Schriftenreihe des
Instituts für Mikrowellentechnik



5

Claudia Vasanelli

Antenna Array Design Solutions for Millimeter-Wave Vehicle-Integrated Automotive Radars

Institut für Mikrowellentechnik
Universität Ulm

Antenna Array Design Solutions for Millimeter-Wave Vehicle-Integrated Automotive Radars



ulm university universität
uulm

Antenna Array Design Solutions for Millimeter-Wave Vehicle-Integrated Automotive Radars

DISSERTATION

zur Erlangung des akademischen Grades eines

DOKTOR-INGENIEURS (Dr.-Ing.)

der Fakultät für Ingenieurwissenschaften, Informatik und Psychologie der Universität Ulm

von

Claudia Vasanelli

aus Bari

Gutachter:	Prof. Dr.-Ing. Christian Waldschmidt
	Prof. Luciano Tarricone
Amtierender Dekan:	Prof. Dr.-Ing. Maurits Ortmanns

Ulm, 10. Oktober 2019

Bibliografische Information der Deutschen Nationalbibliothek
Die Deutsche Nationalbibliothek verzeichnet diese Publikation in der Deutschen Nationalbibliografie; detaillierte bibliografische Daten sind im Internet über http://dnb.dnb.de abrufbar.

Dissertation, Universität Ulm,
Fakultät für Ingenieurwissenschaften, Informatik und Psychologie, 2019

Impressum
Universität Ulm
Institut für Mikrowellentechnik
Prof. Dr.-Ing. Christian Waldschmidt
Albert-Einstein-Allee 41
89081 Ulm
https://www.uni-ulm.de/mwt

Eine Übersicht über alle Bände der Schriftenreihe finden Sie unter
https://www.uni-ulm.de/mwtschriften

Diese Veröffentlichung ist im Internet auf dem institutionellen Repositorium der Universität Ulm (https://oparu.uni-ulm.de) verfügbar und dort unter der Lizenz CC BY-NC-ND 4.0 publiziert.

Details zur Lizenz finden Sie unter
https://creativecommons.org/licenses/by-nc-nd/4.0/

ISBN 978-3-948303-08-2 ISBN 978-3-9800116-5-5 (E-Book)

Acknowledgment

This thesis has been carried out during my work as Research and Teaching Assistant at the Institute of Microwave Engineering of the Ulm University.

First and foremost, I would like to thank my supervisor, Prof. Christian Waldschmidt. The German word for the PhD supervisor is Doktorvater, which explains quite well in my opinion the critical role towards the PhD candidate. For letting me being part of the MWT family, for introducing me to the world of the automotive radars and for his constant guidance, I am really grateful.

I would like to thank Prof. Luciano Tarricone for being the second examiner of this dissertation. Moreover, he first made me passionate about electromagnetism and antennas, and he gave me the required support for starting my experience as an exchange Master's student in Karlsruhe, which then paved the way for my life in Germany.

The PhD journey is not a solitary one. Without the help of Dr.-Ing. Frank Bögelsack, my journey would have been quite boring and way more difficult. For being the best colleague and the best friend I could ever imagine, for his precious encouragement during the hardest time of my life: grazie mille!

For the pleasant, nerdish, and motivating working atmosphere I would like to thank the whole MWT-Kindergarten. In particular, I would like to mention my great office mate, Dr.-Ing. Linus Böhm; Benedikt Meinecke for working together in the KoRRund project; Fabian Roos and Philipp Hügler for their help with the radar measurements and the really useful discussions about DoA estimation together with the other colleagues involved in our DoA paper. A big thank goes also to Adolfo Di Serio, first of all for being a great friend and for his help with the work about the ambiguity function. For the cooperation in the development of the conformal MIMO radar I would like to thank Jonathan Mayer from the Institute IHE of the KIT.

One of the most interesting experiences during my work in Ulm has been the chance of tutoring the students during their Bachelor's and Master's projects. Some results of their theses have been crucial for this dissertation. I would like to thank them all for their precious contributions.

I am also deeply indebted to my Ulmer friends, who made my life in Ulm

easier and funnier. A special thanks to my friends in Italy for their support despite my life abroad.

I would like to thank my family for their never-ending love and constant encouragement during the whole PhD journey, despite the distance and the hard times.

Finally, I owe a huge thank to my father, who has always been a truly source of motivation and inspiration. This work is dedicated to his loving memory.

Contents

1 Introduction **1**
- 1.1 Millimeter-wave automotive radars 1
- 1.2 Goal and outline 4

2 Millimeter-wave antenna arrays for automotive radars **7**
- 2.1 State of the art of mm-wave antenna arrays in PCB technology 7
- 2.2 Antenna requirements and assessment criteria 10
- 2.3 Radar-vehicle integration 18

3 Antenna systems for MIMO radar applications **25**
- 3.1 Background: the virtual aperture 25
- 3.2 Antenna placement optimization 28
  - 3.2.1 Algorithm overview 29
  - 3.2.2 First implementation: the planar case 31
  - 3.2.3 Second implementation: conformal mm-wave MIMO radars 32
- 3.3 Experimental validation of an optimized MIMO antenna configuration 40

4 Design of wideband millimeter-wave microstrip patch arrays **47**
- 4.1 Development of wideband microstrip antennas 49
  - 4.1.1 Patch antenna loaded with parasitic patches 49
  - 4.1.2 Patch antenna with a pair of narrow slots 53
- 4.2 Array design 55
  - 4.2.1 Development of 2-element arrays 55
  - 4.2.2 Development of an 8-element array 59

5 Millimeter-wave low-RCS antennas: fundamentals and principle of operation **67**
- 5.1 Properties of receiving antennas 67
  - 5.1.1 Introduction: the antenna mode and the structural mode 68
  - 5.1.2 Terminology 70

5.1.3 Characterization of the antenna mode and the structural mode of microstrip arrays 71
5.2 A proof of concept: development of a low-RCS surface 74
5.2.1 Surface design 75
5.2.2 Experimental results 81
5.3 Principle of operation of the low-RCS antenna 83
5.3.1 Simulation setup 85
5.3.2 Limitations of the design procedure 87
5.4 Conclusion 89

6 Millimeter-wave low-RCS antenna array design and sensor integration 91
6.1 Measurement setup for the characterization of low-RCS antennas 91
6.1.1 Measuring the RCS reduction for normal and oblique incidence 91
6.1.2 Testing the AUT behind a bumper sample 94
6.2 Development of a microstrip low-RCS array 96
6.2.1 Measurement results of the low-RCS microstrip array . 98
6.2.2 Increasing the area occupied by the AMC 101
6.3 Design of a complex low-RCS antenna system 102
6.3.1 Overview and design procedure 103
6.3.2 Measurement results of the low-RCS MIMO antenna configuration 106
6.4 Integration in a millimeter-wave radar sensor 108
6.4.1 Low-RCS antenna system design 108
6.4.2 Radar measurement results 110

7 Conclusion 119

A Design details of the 8-element array 123
A.1 Array dimensions 123
A.2 Feeding network 124
A.3 Waveguide-to-microstrip transition 126

B Additional measurement results 129

C Some notes on the ambiguity function 133

Bibliography 135

List of acronyms and abbreviations

ADAS . . . . . Advanced driver assistance systems
ADC . . . . . Analog-to-digital converter
AF . . . . . Ambiguity function
AMC . . . . . Artificial magnetic conductor
AoA . . . . . Angle of arrival
AUT . . . . . Antenna under test
CFAR . . . . . Constant false alarm rate
DBF . . . . . Digital beamforming
DML . . . . . Deterministic maximum likelihood
DoA . . . . . Direction of arrival
EBG . . . . . Electromagnetic bandgap
FFT . . . . . Fast Fourier transform
FMCW . . . . . Frequency-modulated continuous wave
FoV . . . . . Field of view
FR-4 . . . . . Flame retardant 4
FSS . . . . . Frequency selective surface
HDI . . . . . High density interconnect
HIS . . . . . High impedance surface
IDFT . . . . . Inverse discrete Fourier transform
LRR . . . . . Long-range radar
LTCC . . . . . Low-temperature co-fired ceramic
MIMO . . . . . Multiple-input multiple-output
MMIC . . . . . Monolithic microwave integrated circuit
MRR . . . . . Mid-range radar

PCB . . . . . Printed circuit board
PEC . . . . . Perfect electric conductor
PMC . . . . . Perfect magnetic conductor
PML . . . . . Perfectly matched layer
PTFE . . . . . Polytetrafluoroethylene
RCS . . . . . Radar cross-section
RFID . . . . . Radio frequency identification
SAE . . . . . Society of Automotive Engineers
SNR . . . . . Signal-to-noise ratio
SRR . . . . . Short-range radar
SUT . . . . . Surface under test
TDM . . . . . Time division multiplexing
ULA . . . . . Uniform linear array
VNA . . . . . Vector network analyzer

1 Introduction

1.1 Millimeter-wave automotive radars

Autonomous driving promises safe and efficient cars in the very near future. While car manufacturers and tech companies all over the world feed the hype of the self-driving car, a tremendous development in advanced driver assistance systems (ADAS) can be seen. Adaptive cruise control, lane change assist, or advanced emergency braking are some examples of the features that are currently employed not only in top level cars. Belonging to the level 2 or lower of the Society of Automotive Engineers (SAE) guidelines for driving automation systems, ADAS can be seen as the fundamental technology to move towards higher level of automation [1].

Typically, a number of different sensors are employed in those systems, such as radar, camera, and lidar. In particular, radar sensors play a significant role due to their robustness against harsh weather conditions [2], like for example fog, darkness, or severe sun dazzle. Two frequency ranges have been assigned to radar sensors for automotive applications. The first one goes from 76 GHz to 77 GHz, while the second one has been set between 77 GHz and 81 GHz [3]. Automotive radars hence fully belong to the mm-wave range. Thanks to the short wavelength, automotive radar sensors show compact dimensions, and this makes particularly easy the integration in the car.

Automotive radar sensors can measure the distance, the velocity, and the angular position of the surrounding targets. According to their function, the radar sensors that are currently on the market are usually categorized as long-range radars (LRR), mid-range radars (MRR) and short-range radars (SRR). Typically, LRRs have a narrow beam, they can measure distances up to 200 m, and they are usually employed for example for adaptive cruise control. They exploit generally the 76 GHz–77 GHz frequency range. On the other hand, SRRs work in the next assigned frequency band to fully benefit from the larger bandwidth to achieve a better distance resolution, required for example for parking aid functions [2]. Finally, MRRs can be used not only for adaptive cruise control, although with a shorter detection range compared to LRRs, but

also for lane change assist or rear cross-traffic alert, since they are able to correctly detect targets around the vehicle or in the driver's blind spot [4].

To address the future requirements of highly automated driving and autonomous driving, today's automotive radar sensors performance need to be improved. Higher resolution radar images are required, in order to correctly identify for example the contour and the orientation of the surrounding vehicles [5]. Moreover, a reliable and robust detection of the relevant targets, and in particular the detection of vulnerable road users such as cyclists or pedestrians, must be still further developed.

In the following, some critical issues that still need further attention and development will be addressed.

The antenna system is a crucial component of the radar sensor. To keep low the production costs and to achieve compact sensor dimensions, the most common choice at the moment is the use of planar antenna arrays, in most of the cases microstrip arrays. However, the limited bandwidth typical of microstrip antennas [6], the fabrication inaccuracies of printed circuit board (PCB) technology, which become more striking at mm-wave frequencies, and the requirements to cover also the frequency range from 77 GHz to 81 GHz make the antenna design challenging. A tolerance-optimized antenna design is required [6], that is to say, an antenna design that offers stable radiation performances in the whole assigned frequency range, and that it is robust against the unavoidable fabrication errors.

Increasing the angular resolution is also a key point for the future development of automotive radars. It is well-known from the antenna array theory that the angular resolution is strictly related to the array aperture. The larger the array, the better the resolution, but at the costs of an increase in sensor dimensions. In automotive applications the estimation of the angular position of a target is usually done with digital beamforming (DBF) on the receiver side, since the mechanical scanning of the antenna array or the use of phase shifters are not cost-effective solutions at mm-wave frequencies [3]. The current trend to increase the angular separation capability is to combine the use of the DBF with a multiple-input multiple-output (MIMO) radar system, which naturally extends the array aperture — and thus improves the angular resolution — with additional virtual antenna elements [7], while keeping compact the physical dimensions of the antenna system. The angular resolution and sidelobe level constraints typically translate into some strict specifications of the virtual array. As a consequence, the virtual array synthesis becomes an important step

to successfully fulfill the antenna system requirements.

Car manufacturers usually hide the mm-wave radar sensors in the car, for instance behind the front and rear bumper, so that the radars do not modify the appearance of the vehicle. The sensor integration is still nowadays a widely underestimated problem, that will become even more significant with the increase of the number of radar sensors employed in a single vehicle. The mounting location behind the bumpers brings a number of related problems. Indeed, a bumper is not designed for the sensor integration or to satisfy particular electromagnetic requirements [8]. The bumper must only obey to safety and aesthetic demands. As a result, a car fascia can significantly degrade the sensor performance. In particular, it can lead to large errors in the estimation of the angular position of the target.

To avoid the problems related to radar-vehicle integration, some car models present an opening in the grille to expose the radar, like in the example of Fig. 1.1. However, since the hidden integration is by far the preferred solution by the car industry, especially because of the increasing number of radar sensors employed in a car, it is important to deeper understand the problem of the radar-vehicle integration and to eventually propose efficient integration solutions. Indeed, one of the big advantages of mm-wave radars compared to other sensor technologies is their potential capability to be placed easily and invisibly in a car [10], and it thus relevant to fully exploit it.



Fig. 1.1: Opening in the grille for placing the radar highlighted by the orange rectangle. Picture reprinted with permission from [9].

1.2 Goal and outline

This thesis deals with the design and development of mm-wave antenna systems for automotive radar applications, that provide the necessary robustness to be successfully integrated in a vehicle and to cope with the increased angular resolution potentiality offered by MIMO radars. In particular, to achieve these goals the main contributions of this thesis are the following:

- development of single-layer wideband microstrip antennas to increase the robustness of the antenna system against the fabrication inaccuracies while keeping at the same time low production costs and fabrication complexity;
- development of an optimization algorithm to define the antenna positions within a MIMO radar. The novelty of this approach resides in the use of a suitable cost function that can take the angular resolution requirements into account;
- development of customized microstrip arrays to improve the radar-vehicle integration and consequently reduce the errors when estimating the angular position of a target.

The work is organized around this three main goals in seven chapters as follows. After this introduction, **Chapter 2** aims to address first of all some basic concepts that will be further required by the following chapters. It briefly offers an overview of the state of the art of mm-wave planar antenna arrays suitable for automotive radar applications. Afterward, it introduces the antenna system requirements and some useful assessment criteria to evaluate the antenna performance, in particular with respect to the problem of the estimation of the target angular position. In addition, the problems related to the radar-vehicle integration are analyzed in details, and their impact on the radar performance is shown. This chapter shows that when the radar sensor is installed behind the bumper, multiple reflections occur between the bumper and the radar itself. Those multiple reflections are then responsible for errors in the estimation of the target position.

The design of an antenna system suitable for a MIMO radar configuration and the issue of the virtual array synthesis have been addressed by **Chapter 3**. After reviewing some MIMO radar fundamentals, the chapter focuses on the development of antenna configurations with the help of a genetic algorithm,

so that the MIMO virtual array can satisfy the given requirements. Moreover, the optimization algorithm has been generalized towards the design of mm-wave conformal MIMO radars, which promise to extend the area that could be illuminated by a radar sensor to detect a target.

Chapter 4 provides the design of wideband mm-wave patch arrays as a tolerance-optimized antenna solution for mm-wave radars. After comparing two different promising antenna designs, the one that offers a more stable performance over the whole frequency range of interest has been further developed into an 8-element array. The antenna array has been fabricated and tested. The measurement results are presented and compared with the full-wave simulation results.

A new solution to the problem of the radar-vehicle integration has been addressed by the **Chapters 5** and **6**. Since the bumper design cannot be in general adapted to the radar sensor needs, a customized antenna design has been proposed here. In particular, the solution introduced by this work, i.e., the design of an antenna array with low radar cross-section (RCS), aims to reduce the amount of power reflected back by the sensor towards the bumper to mitigate the problem of the multiple reflections. The approach followed in this thesis is completely independent of the actual bumper design and properties, and it gives the radar sensor the required flexibility to operate successfully after the vehicle integration.

First, **Chapter 5** gives some fundamentals about the properties of receiving antennas as basic step for the development of a low-RCS antenna. Since the low-RCS antenna design is based on the principle of operation of some chessboard-like metasurfaces proposed in the microwave community in the last years, their principle of operation is reviewed in details, and a low-RCS chessboard-like surface is designed and tested at mm-wave frequencies as a proof of concept.

Chapter 6 investigates the low-RCS antenna design with simulation and measurement results. Different fabricated prototypes are shown and analyzed. Lastly, a low-RCS antenna system is integrated in a mm-wave MIMO radar sensor, and radar measurements have been taken to estimate the angular position of the target. The results are compared with those of a standard mm-wave MIMO radar sensor not equipped with low-RCS antennas to demonstrated how the proposed approach can successfully improve the radar-vehicle integration.

Chapter 7 draws the conclusion and summarizes the main outcomes of this thesis.

2 Millimeter-wave antenna arrays for automotive radars

This chapter provides background information of paramount importance to understand the following of this work.

First of all, an overview of the state-of-art antenna technology for mm-wave automotive radar applications is given. The main design challenges are presented. The technology limitations introduced in this section will be then faced by the microstrip antenna designs presented in Chapter 4.

Fundamental metrics to describe the estimation of the angular position of a target using radar systems are given afterward. The concept of the ambiguity function is introduced, which will be further used in Chapter 3 in the cost function of the optimization algorithm used for generating MIMO radar antenna configurations.

Finally, the problem of the integration of the radar sensor in the vehicle is described in detail. This is the basis for understanding the results of the low-RCS antenna arrays of the Chapters 5 and 6.

2.1 State of the art of mm-wave antenna arrays in PCB technology

The significant market penetration of mm-wave automotive radars even in the middle- and low-class automobile segments is mainly related to the relatively cheap cost of production and to the small size of the sensors, which makes easy the integration in the car. Silicon-germanium (SiGe) monolithic microwave integrated circuits (MMIC) for the generation of the high frequency signal [11] and single PCB antenna array design [12] are the most common choices to keep low both the complexity and the production cost of the sensor. A typical example of such a radar sensor is presented in [13]. In this case, columns of series-fed patch arrays are used as transmitting and receiving antennas. For LRR applications, where a high gain and a narrow beamwidth are required, single patch antennas can also feed a lens antenna, as described in [14].

Standard PCB etching technology assures low production costs, however, significant drawbacks arise at mm-wave frequencies, and they will be here briefly described.

First of all, the most typical substrate materials are not designed, and therefore not characterized, for the frequency range of interest. A deviation from the nominal value of permittivity is thus highly likely; for example, for PTFE-based (Polytetrafluoroethylene) laminates, a deviation up to 5% has been experimentally verified at 77 GHz [15].

Second, standard PCB fabrication offers usually an etching tolerance in the range of 15 µm to 20 µm. Such inaccuracies might affect significantly the antenna design due to the small wavelength. For example, by assuming an effective permittivity of 2.25, the wavelength in the medium would be equal to λ_g=2.59 mm at 77 GHz. As a result, an error of 20 µm in the fabrication is close to 0.8% of the guided wavelength, which might cause in turn a shift of more than 0.6 GHz with respect to the center frequency. By recalling the relative small bandwidth assigned to automotive radar applications, it is easy to understand the potential strong impact of the fabrication inaccuracies on the radar performance. Moreover, for an effective permittivity of 2.25 and a substrate thickness of 127 µm, line widths down to 0.1 mm are commonly used. Also in this case it is straightforward to notice the significance of the etching tolerances with regards to the typical trace widths.

As mentioned in Chapter 1, tolerance-optimized antenna array designs are hence required [6] to give the sensor the necessary robustness against fabrication errors. Moreover, another typical restriction of PCB technology at mm-wave frequencies is the minimum trace (or slot) width. It depends on the substrate copper cladding, and for standard high-frequency laminates and the usual fabrication processes the minimum width is in the range of 90 µm to 100 µm, which can pose quite strict limitations on the antenna design.

Multilayer PCB configurations can provide appealing extra degrees of freedom in the array design, especially to increase the usable bandwidth, but they also lead to an additional source of error, i.e., the interlayer misalignment. Furthermore, the design complexity of the MMIC-to-PCB transition increases for multilayer PCBs. For all these reasons, they are not often employed in commercial applications.

To avoid the problems related to the use of PCB multilayers, hybrid multilayer antenna arrays have been recently proposed [12], where a single layer PCB is combined with thin films attached to it. However, similarly to multi-

layer PCB, the alignment must be done very precisely, and in [12] the thin-film positioning has been carried out using a die bonder.

To overcome the limitations of the PCB technology, alternative approaches have been proposed. Low-temperature co-fired ceramic (LTCC) technology gained a particular interest in the last two decades. It offers highly integrated designs and conductor widths or spacings down to 50 µm [16]. Two different 79-GHz radar sensors for automotive radar applications with antennas developed on LTCC have been presented in [17,18]. The high relative permittivity usually not smaller than ε_r=6 typical of LTCC makes however the antenna design quite challenging, since it reduces the bandwidth and the radiation efficiency. Additionally, during the design process the typical material shrinkage should be taken into account [19]. Finally, the main disadvantage of LTCC technology is still the high production costs compared to standard PCB process, almost independent from volume and miniaturization [20].

Another interesting fabrication technology that can offer highly integrated solutions and small spacings between metal traces close the one of LTCC is the high density interconnect (HDI) PCB[1]. The costs are still significantly higher than simple single layer PCB configurations, but in the future they could potentially decrease hence offering more degrees of freedom in the antenna design. A promising mm-wave planar antenna configuration using such a technology has been presented recently in [21].

However, at the moment it can be concluded that for the reliable series development of antennas for automotive radar applications in the 77-GHz frequency range, there are no realistic alternatives to standard single-layer PCB technology.

To cope with the aforementioned technological limitations, a robust antenna design is needed. This means to develop first a radiating element, and then an antenna array, that still provides an acceptable performance, although the unavoidable fabrication inaccuracies or substrate uncertainties. A robust antenna design can be translated into the development of wideband arrays, where stable performance, in terms of both input impedance matching and radiation pattern properties, can be achieved on a relatively large bandwidth.

As it will be further explained in Chapter 4, this work proposes the use of wideband patch antenna arrays as a tolerance-optimized array design suitable for mm-wave automotive radar applications.

[1] Also known as high resolution multilayer PCB or any-layer PCB.

2.2 Antenna requirements and assessment criteria

The antenna array is a fundamental component of the radar system. Since the array performance significantly affects the ability of the radar to correctly detect the targets, it is essential to define some requirements and assessment criteria that can clearly describe the relationship between array design and radar performance.

It is well known that the main antenna (or array) parameters are usually the impedance matching in the frequency range of interest, i.e., the reflection coefficient $|s_{11}|$, the radiation pattern in the two main cuts, i.e., in the E- and H-plane, and the realized antenna gain.

For automotive radar applications additional criteria can also be introduced. Modern mm-wave radars use normally more than one channel to get angular information of the target in addition to its range and velocity [2]. Typically, the target angle estimation is carried out after the range-Doppler processing, and it is necessary in particular to separate targets that share the same range-Doppler bin. For example, by taking into account a fast-FMCW[2] (frequency-modulated continuous-wave) radar, after receiving the delayed version of the transmitted chirps and down converting them, the signal can be sampled by an analog-to-digital converter (ADC). To estimate the range-Doppler matrix, a two-dimensional fast Fourier transform (FFT) is then used. At this point, the range-Doppler bin of the target of interest can be identified. The complex values generated by the FFT can be then given as input to the further processing required for the direction-of-arrival (DoA) estimation.

Since it is carried out after the range-Doppler processing, the estimation of the angular direction is independent of the radar waveform and modulation scheme [23], while it is strictly related to the antenna system properties, in particular to the number of receiving channels and the receiving array geometry. The angular resolution becomes in particular a key requirement of the system with respect to DoA estimation purposes. A unique widely accepted definition of the angular resolution is not available. The angular resolution depicts the ability of the radar sensor to resolve the angular distance of two closely spaced targets. It depends on the beamwidth of the antenna system, which is inversely proportional to the antenna array aperture. In the literature different definitions of the beamwidth, and consequently of the angular resolution, can be found:

[2] Also known as chirp-sequence radar [22].

- the beamwidth and the angular resolution $\Delta\psi$ can be given by the separation between first nulls in the beam pattern [24];
- the beamwidth and the angular resolution $\Delta\psi$ can be defined as a 3-dB beamwidth (half-power beamwidth) [24];
- the angular resolution $\Delta\psi$ (in radians) is given by the Rayleigh criterion [25], well known from optics, which relates the angular resolution $\Delta\psi$ (in radians) to the separation between the main beam and the first null as

$$\Delta\psi = 1.22\frac{\lambda_0}{d_v}\,, \tag{2.2.1}$$

  where d_v is aperture of the array and λ_0 the free-space wavelength. Although named after Lord Rayleigh, (2.2.1) depends on the diameter of the Airy disk in the case of Fraunhofer diffraction from a circular aperture [26]. The position of the null is given by the first zero of the Bessel function of the first kind of order one $J_1(u)$ [26].

Depending on the radar application, on of the above presented definitions of angular resolution can be employed. In many mm-wave radar applications, the Rayleigh criterion is used to describe the resolution properties of the antenna array [2].

For the sake of completeness, it is also convenient to define the angular accuracy $\delta\psi$ (also in radians) [27]

$$\delta\psi = \frac{\Delta\psi}{\sqrt{2\,\mathrm{SNR}}}\,, \tag{2.2.2}$$

where SNR is the signal-to-noise ratio of the radar system.

The antenna requirements essentially depend on the sensor type specification. For example, the 3-dB beamwidth in azimuth (or elevation) is different for LRR, MRR, or SRR applications [27]. Indeed, while LRR needs a focused and narrow beam to have a good angular resolution, an SRR has a significantly wider beam in azimuth, and even in elevation shows a doubled 3-dB beamwidth compared to LRR and MRR, since the angular resolution is not a critical parameter for this application. Typical angular resolution values for LRR sensors are 1° to 4° for distances larger than 150 m [6,28], while the beamwidth of MRR sensors can be around 20° for 60 m distance [4]. On the other hand, SRRs have stricter

requirements on the range resolution, which is inversely proportional to the bandwidth of the radar system. A larger bandwidth of the radiating element is thus in this case beneficial. The range resolution can reach values equal to or lower than 0.1 m [27, 29].

For DoA-estimation problems (also called angle-of-arrival estimation, AoA), an unambiguous estimation of the angular position of the target is a fundamental requirement. The term ambiguity describes the inability of an antenna array to uniquely distinguish the DoA of the signal reflected by a target. The ambiguity in the DoA estimation is equivalent to the presence of grating lobes in the beam pattern of the receiving array. This concept can be formally described by introducing the so called *ambiguity function* (AF) [30].

Before presenting the signal model to mathematically describe the AF, it is convenient first of all to define the reference system used in this work. It can be seen in Fig. 2.1. Let P be the location of the target expressed in spherical coordinates as $P(r, \psi, \vartheta)$. The angular position can be specified in particular with the azimuth and elevation angles ψ and ϑ. This work focuses only on the azimuth plane, and the DoA estimation problem aims to find the direction of the target indicated by ψ.

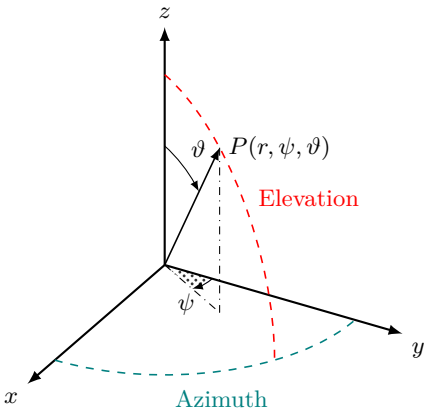

Fig. 2.1: Spherical coordinate system to represent the target position P as a function of the distance r, the azimuth angle ψ, and the elevation angle ϑ.

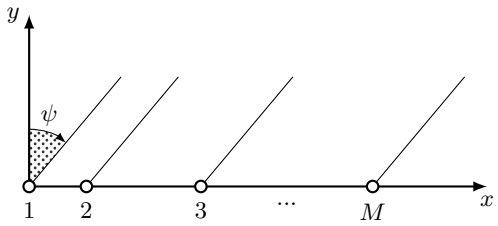

Fig. 2.2: Arrangement of the M elements of the arbitrary-spaced linear array along the x-axis.

To this purpose, consider an arbitrary antenna array with M elements placed on a one-dimensional lattice along the x-axis as depicted in Fig. 2.2. It is also assumed that the target illuminated by the radar is in the far-field of the array. Due to this assumption plane waves propagate, and the directions of propagation of the incoming signals (the azimuth angle ψ drawn in Fig. 2.2) are the same for each element of the array. According to this reference system, the angle ψ is defined in the range $\left[-90^\circ, 90^\circ\right]$ with 0° being the boresight or normal direction. In the ideal case of isotropic radiators, the steering vector of the array associated to the direction ψ is given by

$$\boldsymbol{s}(\psi) = \begin{pmatrix} \mathrm{e}^{\mathrm{j}\beta_0 x_1 \sin(\psi)} \\ \vdots \\ \mathrm{e}^{\mathrm{j}\beta_0 x_M \sin(\psi)} \end{pmatrix}, \tag{2.2.3}$$

where $\beta_0 = \frac{2\pi}{\lambda_0}$ is the phase constant, with λ_0 being the free-space wavelength. The symbol x_k describes the position of the array element with $k{=}1, \ldots, M$. The phase shifts in (2.2.3) are thus only related to the difference in sensor positions; in other words, the signal received by every array element is the same except for the different propagation delays [31].

Then, according to [30] the AF is defined as

$$\chi(\psi_i, \psi_j) = \frac{\left|\boldsymbol{s}^H(\psi_i) \cdot \boldsymbol{s}(\psi_j)\right|}{\| \boldsymbol{s}(\psi_i) \| \| \boldsymbol{s}(\psi_j) \|}, \tag{2.2.4}$$

where the symbol $(\cdot)^H$ denotes the conjugate transpose (Hermitian) vector and

$\|\cdot\|$ the L^2-norm. Due to the presence of the absolute value at the numerator, the function $\chi(\psi_i, \psi_j)$ gets values between 0 and 1. Without taking the absolute value of the numerator, the definition of the AF would be equal to the cosine similarity between the vectors $\boldsymbol{s}(\psi_i)$ and $\boldsymbol{s}(\psi_j)$, which is always within the range -1 to $+1$ [32].

The AF describes how similar the steering vectors are for the directions ψ_i and ψ_j. In other words, this equation evaluates basically the normalized autocorrelation of the steering vector at the angles ψ_i and ψ_j[3]. The correlation reaches the maximum, i.e., 1, when it is not possible to distinguish the value $\boldsymbol{s}(\psi_i)$ from $\boldsymbol{s}(\psi_j)$. This must be of course true when $\psi_i = \psi_j$, but if it happens for $\psi_i \neq \psi_j$, it causes an ambiguity in the DoA [33]. To take into account the complex radiation pattern of a realistic radiating element instead of the isotropic radiator, the steering vector in (2.2.4) can be multiplied by the complex radiation pattern $C(\psi)$ [34].

The above defined AF is also called *type I* [30] or *first order* array ambiguity function [34], since it is assumed that one incident signal impinges on the array, or, in other words, a single target scenario is assumed. This is however not a limiting assumption since in many practical cases a single target occupies a specific range-Doppler bin. As stated in [35], it is anyway not uncommon that two targets share the same range-Doppler bin and need to be separated by identifying their DoA. When the two targets are well separated, namely when their angular separation is larger than the beamwidth of the beamformer [36], the single target theory and techniques can still be applied to find the target

[3] The cross-correlation, or auto-correlation, with zero lag of two signals, or of the signal with itself, is equal to the inner product, whenever the integral and the inner product are well-defined. Given two functions $f(x)$ and $g(x)$, the cross-correlation with lag τ is defined as

$$(f \star g)(\tau) \stackrel{\text{def}}{=} \int_{-\infty}^{+\infty} f^*(x)\, g(x+\tau)\, \mathrm{d}x\,,$$

where f^* is the complex conjugate of f. If τ=0, then the previous equation is identical to the definition of inner product:

$$\langle f, g \rangle \stackrel{\text{def}}{=} \int_{-\infty}^{+\infty} f^*(x)\, g(x)\, \mathrm{d}x\,.$$

Similar conclusions can be drawn for discrete functions.

directions. If the angular separation between the target is smaller than the beamwidth, then super-resolution approaches are required [36], but they are beyond the scope of this thesis.

By plotting the AF it is possible to describe the resolution and ambiguity properties of the array. They depend on the geometrical displacement and number N of the elements in the array, as it can be seen from the definition of $\boldsymbol{s}(\psi)$ in (2.2.3). Indeed, as already known from the antenna theory, the number of elements in an array and the distance between them affect the presence of grating lobes and their positions. The grating lobes have the same amplitude as the main lobe [24], namely they introduce an angular ambiguity. The ambiguity function is usually represented as a three-dimensional surface, where the x- and y-coordinates are the two angles ψ_i and ψ_j, while the z-coordinate describes the magnitude of the ambiguity [37].

To further understand the properties of the AF, it is useful to consider the following examples shown in Fig. 2.3. In particular, Fig. 2.3a shows the AF of a 4-element uniform linear array (ULA) with a spacing between the elements equal to λ_0. On the other hand, Fig. 2.3b presents the AF of a 6-element ULA, again with λ_0 as inter-element spacing. Finally, the plot in Fig. 2.3c depicts the AF for a 6-element ULA, but with a smaller distance between adjacent elements, which is now equal to $\lambda_0/2$. As it can be noticed, the larger the aperture, the thinner is the diagonal width, as it can be seen from the example of Fig. 2.3b. By looking at the plot of the AF, the presence of ambiguities, or grating lobes, can also be concluded. For instance, both in Fig. 2.3a and Fig. 2.3b, where the distance between adjacent antennas is λ_0, it is clear to see the presence of ambiguities: outside the main diagonal the correlation still reaches the maximum value of 1. In this case for example, the DoA of $+30^\circ$ cannot be distinguished from the direction -30°. In the ideal case where no ambiguities are present, the highest magnitude of the AF should be reached only along the main diagonal where $\psi_i = \psi_j$.

By cutting out a row or a column from the plots of the AF of Fig. 2.3, the typical plot of the beam pattern can be obtained. This can be seen for example in Fig. 2.4, where the beam pattern for the DoA $\psi = 30^\circ$ related to two 6-element ULA configurations has been plotted. Again, this result confirms the presence of ambiguities when the distance between the elements of the array is equal to λ_0. As known from the array theory, reducing the distance to $\lambda_0/2$ permits to see a single maximum in the beam pattern at the very same position of the DoA. Some additional comments on the relationship between the AF and

the beam pattern can be found in the Appendix C on page 133.

For automotive applications it is important that the angular range where the DoA estimation is performed is free of ambiguities or near-ambiguities. Usually, this range coincides with the field of view (FoV) of the radar sensor. The FoV outlines the maximum range (in meter) where a target with a given RCS (in the next section a formal definition of the RCS will be given) can be still detected

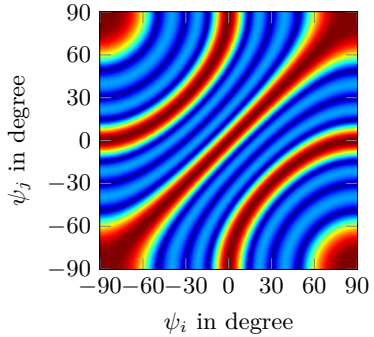

(a) 4-element ULA with λ_0-spacing.

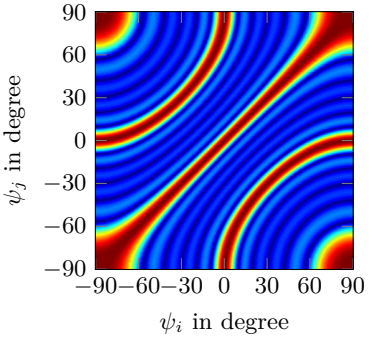

(b) 6-element ULA with λ_0-spacing.

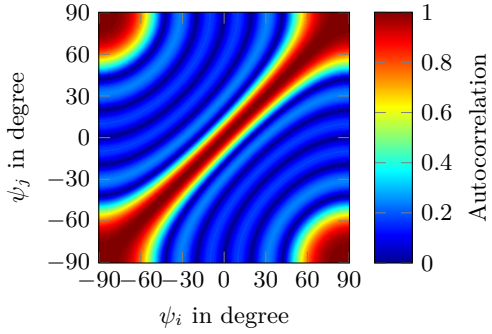

(c) 6-element ULA with $\frac{\lambda_0}{2}$-spacing.

Fig. 2.3: Examples of the ambiguity function for three different array configurations.

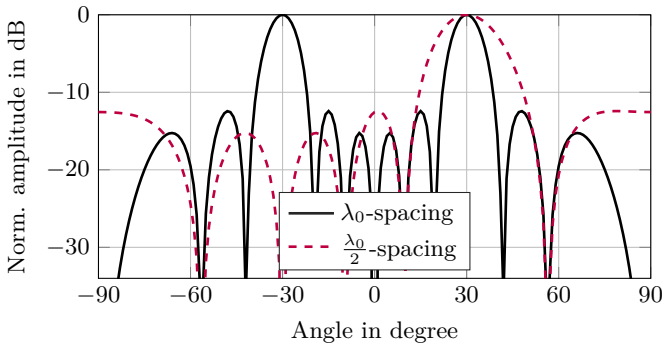

Fig. 2.4: Beam pattern for two 6-element ULAs with different inter-element spacing.

by the radar with an acceptable minimum SNR. The maximum range for the direction ψ, namely $R(\psi)$, can be directly calculated from the well-known radar equation [38]

$$R(\psi) = \sqrt[4]{\frac{P_t\, G_t\,(\psi)\; G_r\,(\psi)\; \lambda_0^2\, \sigma}{(4\pi)^3\; \mathrm{SNR}_{\min}\, k\, \left(T\, + (F-1)\, T_0\right)\; B}}\,, \tag{2.2.5}$$

where P_t is the transmitted power, $G_t(\psi)$ and $G_r(\psi)$ are the gain of the transmitting and receiving antennas, λ_0 is the free-space wavelength, σ the RCS of the target, $\mathrm{SNR}_{\min}$ the minimum acceptable SNR, k the Boltzmann's constant, T the temperature of the radar system, T_0 the standard temperature, F the noise figure of the system, and B the bandwidth. The antenna radiation pattern plays thus a primary role in defining the area illuminated by the radar, that is to say its FoV. Indeed, in the directions where the antenna gain is smaller, the maximum achievable range is shorter, too.

Typically, to the purpose of the DoA estimation it is useful to define an ambiguity-free area. It is usually depicted as a square centered around the boresight direction on the main diagonal of the AF plot and bounded by the first spot where the AF amplitude reaches the maximum or a predefined threshold value, see for example Fig. 2.5. If the ambiguity-free range is larger than the FoV, then it can be concluded that the DoA estimation can be carried out in an

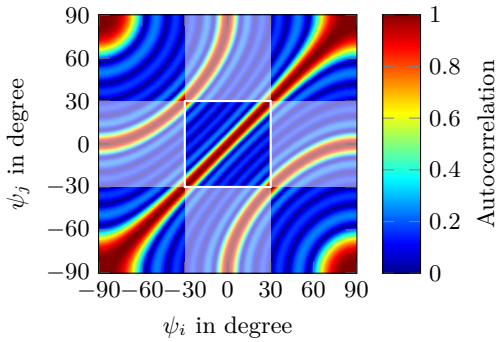

Fig. 2.5: Plot of the AF of a 6-element ULA with a distance between adjacent elements equal to λ_0. The white box in the center describes the ambiguity-free region, while the shaded area highlights the critical directions that could lead to a wrong DoA estimation, since they belong to the FoV of the sensor but not the ambiguity-free area.

ideal case successfully without occurring in any ambiguity or near-ambiguity higher than the given threshold. On the other hand, if the ambiguity-free range is smaller than the FoV, it is still possible that for some directions the solution of the DoA problem can lead to a wrong estimation of the angular position of the target. This issue can be easily understood by looking at the plot of Fig. 2.5. In this example, the FoV has been assumed to be confined within $\pm 90^\circ$, while the ambiguity-free area is confined to $\pm 30^\circ$. All the directions that belong to the shaded areas can still lead to DoA ambiguities although they do not belong to the ambiguity-free region. It is clear for example that a target placed at -60°, thus inside the FoV of the radar, can still bring to a misleading estimation close to the boresight direction.

Hence, a joint analysis of the AF and the FoV of the sensor should be done to understand whether the ambiguities can affect the performance of the radar [39], such as causing an unnecessary braking intervention.

2.3 Radar-vehicle integration

The hidden integration of sensors in the car for ADAS or autonomous driving purposes is a crucial issue for car manufacturers, that could play a signifi-

cant role in finally fully moving from research to serial implementation of autonomous vehicle as standard everyday cars [10]. As it can be easily imagined, the sensors should not disturb indeed the aesthetic of the vehicle.

The compact dimensions are one of of the key features of mm-wave automotive radars due to the small free-space wavelength, which is λ_0=3.9 mm at 77 GHz. Thanks to this advantage, the sensors can be typically placed behind the front and rear bumpers of the vehicle, as already explained in Chapter 1. On the other hand, the bumper of a vehicle is not designed for the integration of a mm-wave radar sensor [8], and it must usually not fulfill any strict requirement from an electromagnetic point of view. As a result, a car fascia can significantly affect the radar sensor performance. In particular, the shape, the material composition, and the presence of a coating influence the target detection and estimation capability of a radar [40].

A bumper is composed of multiple layers. Usually, a low-cost plastic layer is followed by a primer and then by the coatings (base coating and clear coating) [8]. The coatings control the appearance of a printed bumper, and it contains often metal particles. Those metal flakes are responsible for a strong reflection of an impinging electromagnetic wave by the bumper, since the metal concentration in the coating sets the relative permittivity of the medium ε_r. Experimental results demonstrated that values of ε_r up to 53 can be achieved at 76.5 GHz [41]. The dimensions of the metal particles are greatly smaller than the wavelength, hence the coating can be described as a homogeneous material characterized by an effective permittivity.

The first problem associated with the placement of the radar behind the bumper can be easily understood with the help of the transmission line model presented in Fig. 2.6. In this simplified approach the complex multilayer structure of the bumper is modeled as a single equivalent lossless dielectric material. Consider the wave emitted by the radar that impinges on the bumper. Part of the wave will be transmitted, and part will be reflected back. The transmission and reflection coefficients can be calculated by using the transmission line model, that describes the transition between the air and the bumper. By using this model it is possible to define a scattering matrix $\boldsymbol{S}$ and to calculate the associated scattering parameters. The scattering matrix has transmission and reflection symmetry, and thus, only two parameters are necessary to fully describe it. The input reflection coefficient s_{11} and the transmission coefficient s_{21}

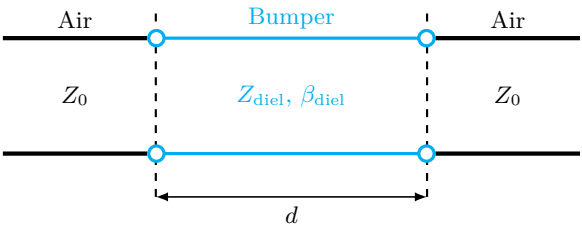

Fig. 2.6: Transmission line model to represent the interface between the air and a bumper with thickness d. Z_0 and Z_{diel} denote the free-space impedance and the impedance in the medium, respectively. The phase constant in the dielectric is β_{diel}.

are

$$s_{11} = s_{22} = r - \frac{t^2 r \mathrm{e}^{-\mathrm{j}2\beta_{\text{diel}}d}}{1 - r^2 \mathrm{e}^{-\mathrm{j}2\beta_{\text{diel}}d}}\,, \tag{2.3.1}$$

$$s_{21} = s_{12} = \frac{t^2 \mathrm{e}^{-\mathrm{j}\beta_{\text{diel}}d}}{1 - r^2 \mathrm{e}^{-\mathrm{j}2\beta_{\text{diel}}d}}\,, \tag{2.3.2}$$

where

$$r = \frac{Z_{\text{diel}} - Z_0}{Z_{\text{diel}} + Z_0} \tag{2.3.3}$$

and

$$t = \frac{2\sqrt{Z_{\text{diel}} Z_0}}{Z_{\text{diel}} + Z_0}\,. \tag{2.3.4}$$

The quantities Z_0 and Z_{diel} are the wave impedances in free space and in the dielectric, respectively, and they are given by

$$Z_0 = \sqrt{\frac{\mu_0}{\varepsilon_0}} \tag{2.3.5}$$

and

$$Z_{\text{diel}} = \frac{Z_0}{\sqrt{\varepsilon_r}}\,, \tag{2.3.6}$$

with μ_0 being the vacuum permeability and ε_0 the vacuum permittivity.

The equations (2.3.1) and (2.3.2) demonstrate that the thickness of the bumper d and the effective permittivity ε_r control the reflection and transmission coefficients. In particular, given a specific value of effective permittivity, the thickness d determines the presence of constructive or destructive interference [10]. As an example, consider the results shown in Fig. 2.7, where the relative permittivity has been set to the value of 7. As it can be seen, by changing the value of the thickness d, quite a significant change in the reflection transmission coefficients can be observed. For example, the best result for the reflection coefficient is achieved when d=2.9 mm, which is close to $2\lambda_g$ at 78 GHz, where λ_g is the wavelength in the medium. On the other hand, it can be seen that the reflection and transmission coefficients get worst at 79.6 GHz when d=$2.25\lambda_g$=3.2 mm.

In the transmission line model the dielectric losses have been neglected. In [8] it has been actually demonstrated that the power losses due to the absorption from the car fascia materials are small compared to the losses due to constructive and destructive interference phenomena related to the thickness of the bumper. The thickness of the bumper must be then carefully chosen to avoid a degradation of the radar performance.

The car fascia can also be described as a relatively strong reflecting object in front of the radar antennas at a very small distance. This can lead to a short-range leakage, which causes sensitivity and detection degradation of the radar system. An artificial on-chip target for short-range leakage cancellation purposes has been proposed in [42] to efficiently address this problem.

An additional and even more critical problem can also arise with the placement of the radar behind the bumper, and it will be here discussed. To better understand it, consider the following example presented in [43] and depicted also in Fig. 2.8.

A radar sensor illuminates a target placed on the street. The wave reflected back by the target will impinge on the metal housing and on the PCB of the sensor. The PCB and the metal housing will reflect again the impinging wave towards the bumper, which in turn will reflect again a part of the impinging wave due to the high permittivity of the car fascia. The antennas of the radar will receive thus two superimposed signals. The first one is the signal of interest directly reflected by the target, represented by a solid line in Fig. 2.8. The latter contains the signal of interest from the target plus an additional contribution, which comes from the multiple reflections between the radar and the bumper,

see the dotted line in Fig. 2.8. Since the distance between sensor and bumper is in the range of a few centimeters, it is typically not possible to resolve them, and thus, both signals will be detected in the same range cell. As mentioned at the beginning of Section 2.2, the DoA estimation is carried out usually after the range-Doppler processing, hence the superposition of the unwanted signal can generate a wrong phase progression among the channels. As a consequence, the multiple reflections can potentially lead to a wrong target DoA estimation, which might in turn cause a wrong intervention in the driving process.

Additionally, it is important to underline that, with the placement of the

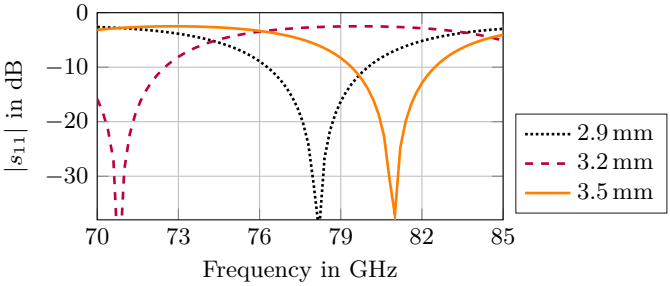

(a) Reflection coefficient.

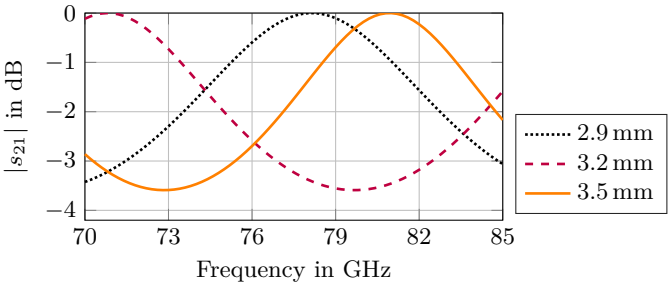

(b) Transmission coefficient.

Fig. 2.7: Scattering parameters for the transmission line model of Fig. 2.6. A sweep on the thickness d of the bumper has been performed. The relative permittivity has been set to 7.

bumper behind a relatively strong reflecting structure like the car fascia, a standing wave can occur. In general, it is convenient to avoid that the bumper is located exactly at one of the minima of the standing wave pattern. However, in a practical scenario where the sensor is installed in a car, it is usually hard to exactly control the positioning behind the fascia, typically due to mechanical inaccuracies.

It can be concluded that design strategies and approaches to mitigate the multiple reflections between radar and bumper are of great practical interest. Although this thesis focuses on automotive radar applications, similar issues could arise in general when an antenna system needs to be placed behind a protective material or even behind a radome. The approach proposed in this work can be generalized in principle to non-automotive scenarios, too.

To carry out the DoA estimation usually it is first necessary to calibrate the radar sensor to take into account the typical deviations from the ideal designed antenna system. In theory, for an automotive scenario it could be possible to calibrate the sensor directly behind the bumper of the car. Although this would represent the ideal solution to the radar-vehicle integration problem, this approach is not a feasible option in any practical case due to the huge related

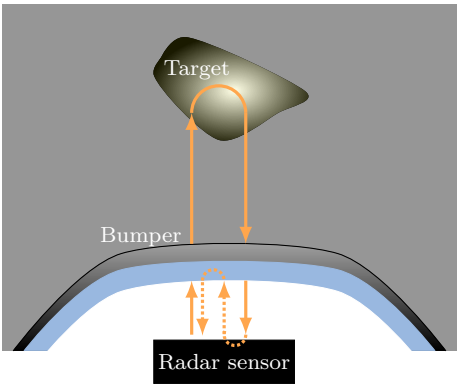

Fig. 2.8: Multiple reflections between the radar sensor and the bumper of the car. The dotted lines represent the unwanted contributions due to the backscattering from the radar sensor. Picture from [43], ©2018 IEEE.

effort and cost, since it would require a dedicated calibration of the sensor for every car model and mounting position.

With the help of Fig. 2.8 it can be understood that only two approaches are possible: either the bumper design or the sensor design should be optimized and adapted to reduce the multiple reflections. Some previous studies already investigated the problem of reducing the reflections from the bumper. For example, in [44] and [41] the authors propose to compensate the reflections of the coating with some inductive strips or frequency selective surfaces (FSS), in particular by clamping an FSS layer on the back side of the bumper to compensate it. Unfortunately, this approach seems too complex in most practical cases. Indeed, these solutions highly depend on the specific material composition and dielectric properties of the bumper. It means that a customized FSS should be developed for every different kind of bumper.

The approach taken in this thesis is quite different, and it focuses on an optimized sensor design, specifically developed to face the vehicle-integration issue. It will be discussed in detail in Chapters 5 and 6, as already mentioned in the outline of this work.

The basic idea is to equip the radar sensor with a low-RCS antenna system in order to suppress the wave reflected back towards the bumper, represented by the dotted lines in Fig. 2.8, and thus, to mitigate the multiple reflections. The RCS is indeed the parameter that describes the amount of power reflected by a target when it is illuminated by an incident plane wave[4]. The proposed solution is definitely appealing, since it is totally independent of the bumper properties and geometrical features, and no a priori knowledge about the car fascia in terms of both shape and material composition is required.

[4]The radar cross-section (RCS) or echo area of a target is defined as [45]

$$\sigma = \lim_{r\to\infty} 4\pi r^2 \frac{\left|\mathbf{E}_s(r)\right|^2}{\left|\mathbf{E}_i(r)\right|^2},$$

where $\mathbf{E}_s(r)$ is the electric field scattered by the target, $\mathbf{E}_i(r)$ the incident field at the target, and r the distance from the target to the point where the scattered power is measured. The RCS is measured in squared meters, or in logarithmic scale in dBsm (decibel relative to one square meter). Using the previous equation, the value of σ is a scalar and a real number, and it depends in general on the specific polarization, the frequency, and the angular orientation of the target [46]. If a reference plane has been defined to set the phase of the incident and scattered field, then the RCS can also be expressed as a complex quantity [46].

3 Antenna systems for MIMO radar applications

Estimating the DoA of a target is a key feature of mm-wave automotive radars. In Chapter 2, in particular in Section 2.2, it has already been recalled that the angular resolution $\Delta\psi$ is strictly related to the physical aperture of the sensor, as described for example by the Rayleigh criterion in (2.2.1). Thus, to improve the angular resolution, the antenna aperture must be increased. This would however also cause an increase in the overall dimension of the radar sensor.

Although super-resolution algorithms that overcome the Rayleigh criterion limitation have already been investigated and developed in the literature, the current trend in automotive radars is exploiting the features of MIMO techniques [3, 47, 48]. The main drawback of super-resolution algorithms is that they can require computationally expensive signal processing, or the use of a priori information about the number of targets, or moderate to high SNR [49].

This chapter provides the concept of the virtual aperture associated to a MIMO radar, which is the key point that allows a MIMO radar to outperform the angular resolution properties of a traditional radar sensor. Afterward, the problem of designing a suitable MIMO radar antenna configuration will be addressed.

3.1 Background: the virtual aperture

Depending on the antenna placement, two kinds of MIMO radar systems have been introduced in the scientific literature: MIMO radars with widely separated antennas and MIMO radars with co-located antennas [7, 50]. The latter ones are of interest for this work, because of the limited spacing between transmitting and receiving antennas on the PCB and because they allow to define an equivalent virtual aperture, which shows in turn better angular resolution properties than the real antenna systems.

A MIMO radar with co-located antennas – from now simply referred as *MIMO radar* – requires the transmission and reception of orthogonal signals, that can be then uniquely associated with every transmitter. This means that all the two-way transmitter-receiver paths can be measured separately [51].

Two signals are orthogonal if they have a zero cross-correlation. The orthogonality can be obtained in the time, frequency, or code domain [52]. For automotive radars, the time division multiplexing (TDM) is up to now the most typical solution thanks to the relatively easy implementation, although investigation on code division [53] and frequency division multiplexing schemes is currently ongoing [54]. For a TDM scheme, the radar transmitters are simply sequentially activated.

If orthogonal waveforms are assumed, it is possible to extend the physical array aperture by defining an equivalent receiving array with virtual sensors, that shows an aperture larger than the physical one. Thus, this makes the beamwidth narrower, and consequently, the angular resolution improves. The MIMO array configuration can be fully described by the properties of its virtual counterpart [51]. This is the case, for example, of the resolution properties for a DoA estimation problem.

To formally describe the synthesis of the virtual aperture, let M_t and M_t be the number of transmitters and receivers, respectively, of a MIMO radar placed on a one-dimensional lattice. Using the same notation introduced for the steering vector definition in (2.2.3) and the coordinate system of Fig. 2.2, the steering vectors associated with the transmitters and receivers for the angular direction ψ can be written as

$$\boldsymbol{a}(\psi) = \begin{pmatrix} \mathrm{e}^{\mathrm{j}\beta_0 x_{t,1}\sin(\psi)} \\ \vdots \\ \mathrm{e}^{\mathrm{j}\beta_0 x_{t,M_t}\sin(\psi)} \end{pmatrix}, \quad \boldsymbol{b}(\psi) = \begin{pmatrix} \mathrm{e}^{\mathrm{j}\beta_0 x_{r,1}\sin(\psi)} \\ \vdots \\ \mathrm{e}^{\mathrm{j}\beta_0 x_{r,M_r}\sin(\psi)} \end{pmatrix}, \tag{3.1.1}$$

where $x_{t,k}$ and $x_{r,l}$ denote the position of the transmitters and receivers, respectively, with $k{=}1,\ldots,M_t$ and $l{=}1,\ldots,M_r$. Finally, it is possible to define the vectors $\boldsymbol{x}_t$ and $\boldsymbol{x}_r$, which contain the physical positions of the transmitters and receivers, respectively.

The steering vector associated to the MIMO virtual array can be calculated as

$$\boldsymbol{y}(\psi) = \boldsymbol{a}(\psi) \otimes \boldsymbol{b}(\psi)\,, \tag{3.1.2}$$

where $\otimes$ is the Kronecker product[1]. The vector $\boldsymbol{y}(\psi)$ is a column vector with

[1] Given two matrices $\boldsymbol{A}$, with dimensions $M \times N$, and $\boldsymbol{B}$, with dimensions $P \times Q$, the matrix $\boldsymbol{A} \otimes \boldsymbol{B}$ is called the Kronecker product, or tensor product, or direct product of

dimension $M_t M_r$, since $\boldsymbol{a}(\psi)$ and $\boldsymbol{b}(\psi)$ are column vectors with dimensions M_t and M_r, respectively. From (3.1.2) it can be concluded that given $M_t + M_r$ physical antennas, it is possible to define a virtual array with $M_t M_r$ virtual elements.

For the sake of completeness, it should be mentioned that the virtual array steering vector $\boldsymbol{y}(\psi)$ can also be calculated as follows:

$$\boldsymbol{y}(\psi) = \text{vec}\left(\boldsymbol{a}(\psi)\boldsymbol{b}^T(\psi)\right) \tag{3.1.3}$$

where the symbol vec $(\cdot)$ denotes the matrix vectorization[2], and $(\cdot)^T$ is the transpose operator. The previous equation comes directly from the relationship between the Kronecker product of two vectors and the vectorization operator [57]. Thus, the expressions in (3.1.2) and (3.1.3) are equivalent.

The virtual array contains all the possible transmitter-receiver pairs. If the antenna radiation pattern has been included in the steering vector definition, then the virtual elements will show an *equivalent* radiation pattern given by the multiplication of transmitter and receiver radiation patterns. The elements of $\boldsymbol{y}(\psi)$ are located on an one-dimensional lattice at the position $x_{t,k}+x_{r,l}$, with $k=1,\ldots,M_t$ and $l=1,\ldots,M_r$ [57]. These locations can also be obtained by convolving the physical positions of the transmitters and receivers [57]. Figure 3.1 presents an example of the synthesis of the virtual array. The virtual array shows a larger aperture compared to the physical receiving array, namely $d_v > d_r$. As it can be noticed, given two transmitters and three receivers, the virtual array is composed of six elements, and it extends thus the physical aperture of the receiving array.

Depending on the placement of the transmitters and receivers, it is possible that at some virtual positions certain elements overlap. This can be described as a spatial tapering of the virtual aperture, and it allows for example to reduce the sidelobe level [58] in the virtual array beam pattern, although at the cost of a smaller virtual aperture. Obtaining overlapping elements in the virtual array can also be used to compensate the phase errors due to target movements while

$\boldsymbol{A}$ and $\boldsymbol{B}$. The dimension of the matrix $\boldsymbol{A} \otimes \boldsymbol{B}$ is $MP \times NQ$ [55].

[2] Let $\boldsymbol{A}$ be a matrix with dimension $M \times N$. The vectorization vec$(\cdot)$ of $\boldsymbol{A}$ is a linear transformation that converts the matrix into a column vector with dimensions MN [56]:

$$\text{vec}(\boldsymbol{A}) = (\boldsymbol{a}_1\, \boldsymbol{a}_2 \ldots \boldsymbol{a}_N)^T$$

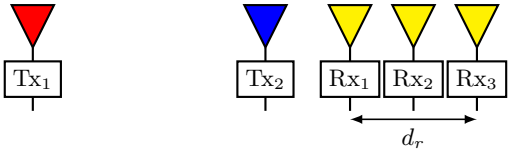

(a) Transmitting and receiving antennas.

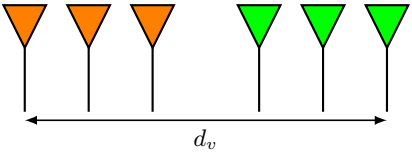

(b) Virtual array.

Fig. 3.1: Synthesis of the virtual aperture for a MIMO radar system composed of M_t=2 and M_r=3 antennas placed on a one-dimensional lattice. Every virtual element is given by a transmitter-receiver pair. For example, the pair made up of the Tx_1 (in red) and Rx_i (in yellow) is represented by the orange elements in the virtual array.

switching the radar transmitters in a TDM scheme [51].

3.2 Antenna placement optimization

As already noticed in the simple example of Fig. 3.1, the positions of the transmitting and receiving antennas set the MIMO virtual array. However, the antenna positions and characteristics affect at the same time several system metrics, like the FoV of the sensor and the achievable unambiguous range in the DoA estimation.

The classical array synthesis techniques can also be applied to the virtual array, for achieving, for example, a desired aperture or sidelobe level. Compared to the standard array design, for a MIMO radar a further important step is necessary, since it is required to map the virtual array configuration into the real locations of transmitters and receivers. This problem does not have however a unique solution, since it is in principle possible that more than one transmitter-receiver configuration synthesizes the same virtual aperture.

Since the inverse mapping from the virtual array to the real transmitter-

receiver configuration cannot be analytically solved, to obtain the real antenna placement an optimization problem must be solved. In this way, the beam pattern of the MIMO virtual array can be synthesized according to a predefined cost function.

3.2.1 Algorithm overview

Different optimization approaches can be used. The most basic one, that is to say the brute force search, is feasible only for a small number of antenna elements [59]. For more realistic MIMO configurations, where a larger number of elements is required, a more sophisticated optimization algorithm must be used. For example, in [59] an algorithm based on the particle swarm optimization solves the problem of finding the optimal antenna placement. In this thesis, the solution of the global optimization problem has been searched by means of a genetic algorithm. A genetic algorithm – introduced first by Holland and then further developed by Goldberg, see [60, 61] – is a numerical optimization method that belongs to the class of evolutionary algorithms, and it searches for the best solution following the natural processes of genetic recombination and evolution [62].

Both the genetic algorithm and the particle swarm optimization are well known and widely employed for solving electromagnetic problems. The reader can refer to [61,62] for an introduction to genetic algorithms, or to [63] for their performance comparison. A detailed analysis of the algorithm performance and characteristics is outside the purpose of this work. The key and the interesting point, and above all the novelty proposed in this work, is on the other hand the choice of an appropriate cost function for the specific application, i.e., the design of a MIMO array configuration. The cost function used in a genetic algorithm is usually called *fitness* function.

In the optimization algorithm used in this work, the classical skeleton of a genetic algorithm has been retained to calculate the best position for the transmitting and receiving antennas. This can be noticed in the flowchart of Fig. 3.2. Two slightly different implementations of the algorithm for finding the optimal antenna placement of a MIMO radar configuration have been implemented and tested. The basic version will be first presented in Section 3.2.2 to give a qualitative description of the algorithm, while a more general one suitable for non-planar antenna configurations will be explained later in Section 3.2.3. For this second version, a more detailed description of the fitness

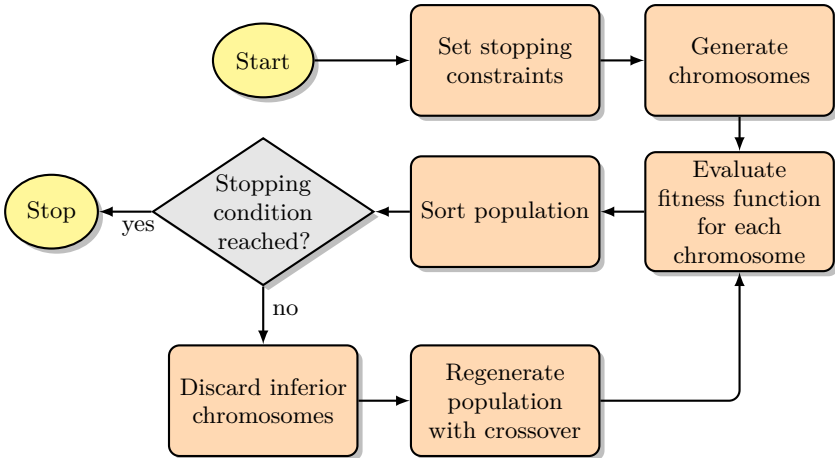

Fig. 3.2: Algorithm flowchart.

function evaluation will be provided.

In both versions the genes, the elementary units of the genetic algorithm, describe the position of the transmitting and receiving antennas, while a chromosome, defined as a set of genes, represents the MIMO antenna configuration. Hence, a chromosome consists of M_t+M_r genes.

The search of a suitable fitness function is an important step in the definition ot the optimization algorithm, since this choice is intimately related to the specific application. In particular, the fitness function must be a measure of system performance to be maximized or minimized [64].

As it has been explained in Chapter 2, for DoA estimation problem, the ambiguity function (AF) is a significant metric to describe the resolution and ambiguity properties of the antenna system. For this reason, this work exploits in both implementations the AF for the definition of the fitness function of the genetic algorithm. As it will be further explained in the next sections, the main idea of the fitness function is to maximize the ambiguity-free area within the ambiguity function. To this purpose, a threshold on acceptable values of the AF inside the ambiguity-free area must be given, which can be any value between 0 and 1 according to the application requirements.

3.2.2 First implementation: the planar case

In the following, it is assumed that the first transmitter is placed in the origin of the reference system, at the position $x{=}x_{t,1}{=}0$. Therefore, the $M_t{+}M_r{-}1$ remaining antenna positions have to be determined. Moreover, to simplify the optimization it has also been assumed that along the one-dimensional lattice, starting from the origin, the transmitting antennas occupy the first positions and they are then followed by the set of receivers. In principle, it is however possible to generalize the algorithm towards an arbitrary antenna placement, and this will be shown in Section 3.2.3. Under the previous assumptions, the virtual aperture d_v of the MIMO array, see Fig. 3.1, can be calculated in a multistatic case[3] starting from the position of the transmitters and receivers. In particular, the virtual aperture is given by

$$d_v = \max(\boldsymbol{x}_t) + \underbrace{\max(\boldsymbol{x}_r) - \min(\boldsymbol{x}_r)}_{d_r}\,, \tag{3.2.1}$$

where $\max(\boldsymbol{x}_t){=}x_{t,M_t}$ is the position of the last transmitter, $\max(\boldsymbol{x}_r){=}x_{r,M_r}$ the position of the last receiver, and $\min(\boldsymbol{x}_r){=}x_{r,1}$ the position of the first receiver. The difference between $\max(\boldsymbol{x}_r)$ and $\min(\boldsymbol{x}_r)$ gives the aperture of the receiving array d_r, also highlighted in Fig. 3.1.

The algorithm starts with determining the necessary virtual array length using the Rayleigh criterion (2.2.1) for a desired angular resolution given as an input. The fitness function must be then evaluated for each chromosome.

As mentioned before, the fitness function aims to maximize the ambiguity-free region. The size of this region is calculated from the plot of the AF by counting the number of contiguous points where the ambiguity function has a value lower than the threshold given as an input to the algorithm, starting from the center of the main diagonal. The points that belong to the main diagonal are excluded from the area that should be evaluated.

The main advantage of such a cost function is that it is possible to take all the potential DoA of interest at the same time into account. This would not be possible, for example, by using as cost criterion the sidelobe level of the beam pattern like in the classical array synthesis problem, since it depends in general on a specific DoA [65].

In Chapter 2 it has been extensively explained, how important it is to carry

[3] In this first version, the transmitters and the receivers never share the same position.

out a joint analysis of the FoV and of the AF to assess the angle estimation performance of the radar sensor. However, in this first implementation of the optimization algorithm the FoV has not been taken into account. Indeed, a joint optimization of FoV and AF is not a trivial task. As it can be seen in (2.2.5), the FoV is a function of the range, while the AF is totally independent of the target distance. For this reason, in this first step only the AF plays a role for the definition of the cost function. The FoV analysis must be carried out separately at the end of the optimization process on the calculated solution. In the next section a more general approach for the implementation of the algorithm will be presented, where also the FoV properties can be partially taken into account.

To obtain usable optimization results, some additional constraints must also be defined. For example, the minimum distance between adjacent antennas $d_{\min}$ can be given to take into account the physical dimension of the antennas and the required distance to have an acceptable level of mutual coupling. In the simulation framework the mutual coupling between the antennas has not been included, since this would cause a great increase in the simulation time and complexity. The mutual coupling depends on the distance between the antenna elements, and hence for every array configuration analyzed by the optimization algorithm a new full-wave simulation should be performed to calculate it. As it can be easily understood, this approach would result in an unbearable computation time.

Finally, the same kind of radiating elements has been assumed for the transmitters and receivers. Accordingly, it is not necessary to incorporate the antenna radiation pattern in the algorithm, since the antenna configuration shows the same ambiguity properties as the ideal case with isotropic radiators (see the Appendix C on page 133).

3.2.3 Second implementation: conformal mm-wave MIMO radars

The second implementation of the genetic algorithm generalizes the previous approach towards the design of a non-planar MIMO radar antenna configuration. Before going into the details of the implementation, a brief introduction about the use of non-planar antenna systems for MIMO radars is here given.

A promising trend for achieving higher safety standards of radar-based driver assistance systems is the use of a radar sensor network to realize a 360°-FoV coverage around the car. An example of such a network for automotive appli-

cations can be found in [66]. In this case, simple sensors with a single receiving channel have been employed. Hence, although the DoA estimation is not possible with the single radar, this can still be calculated through a cooperative signal processing in the network.

Even more ambitious is the mm-wave radar network approach supported by the project KoRRund [67], founded by the German Federal Ministry of Education and Research. The aim of KoRRund is also the development of a radar network to cover the complete FoV around the car. However, in this project the single radar sensors are equipped with more than one channel to increase the DoA estimation capabilities. Moreover, they present a non-planar shape in order to increase the typical FoV achievable with a planar mm-wave radar sensor. This can potentially reduce the total number of nodes required in the network to achieve the fully 360°-coverage. The sensors employed in the project are MIMO radars, thus, the transmitting and receiving antenna positions control the properties of the associated virtual array. The additional degree of freedom given by the conformal shape makes the optimization of the antenna placement much more demanding.

Figure 3.3 shows a simplified top-view representation of an arbitrary conformal antenna system with M elements. Let $\boldsymbol{s}(\psi)$ be the steering vector associated to it. Compared to the example of Fig. 2.2, where a planar array configuration has been introduced, now the shift along the y-direction must also be taken into account for the correct calculation of the phase progression along the array elements. Thus, under the usual far-field assumption the steering

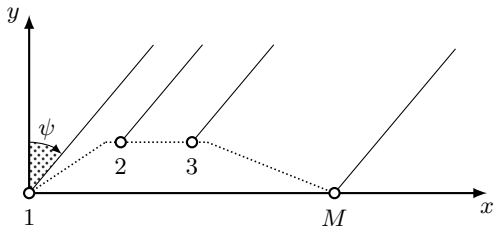

Fig. 3.3: Arrangement of M antenna elements along an arbitrary conformal faceted shape. This sketch represents the top view of a MIMO radar antenna system. Picture from [68], © 2019 IEEE.

vector for the angular direction ψ becomes

$$\boldsymbol{s}(\psi) = \begin{pmatrix} \mathrm{e}^{\mathrm{j}\beta_0\left(x_1 \sin(\psi)+y_1 \cos(\psi)\right)} \\ \vdots \\ \mathrm{e}^{\mathrm{j}\beta_0\left(x_M \sin(\psi)+y_M \cos(\psi)\right)} \end{pmatrix}, \tag{3.2.2}$$

where x_k and y_k describe the x- and y-coordinates of the array element with index $k{=}1, \ldots, M$. For a MIMO radar the definition of the steering vectors associated to the transmitting and receiving array must be then adapted accordingly.

Finally, the virtual array of a conformal MIMO antenna configuration consists of a two-dimensional arrangement of virtual elements in the xy-plane. The position of the virtual elements can be calculated in an analogous way compared to the planar case. Indeed, the coordinates of the virtual elements are simply given by $x_{t,k}{+}x_{r,l}$ and $y_{t,k}{+}y_{r,l}$, with $k{=}1, \ldots, M_t$ and $l{=}1, \ldots, M_r$.

For the practical realization of a conformal mm-wave antenna system two different approaches can be followed. With the first one, schematically represented by Fig. 3.3, the conformal shape can be approximated by many planar PCBs with different orientations connected together. This approach is to some extent similar to the radar demonstrator of [69]. In this case, the piecewise planarity of the structure permits to retain the planarity of the antenna elements, too. It is implicitly assumed that the single radiators cannot be placed directly at the joints between two facets. The second option is to develop a truly conformal array, where also the antenna elements follow the same shape of the curved surface.

This work analyzes only the first approach, that is to say, the faceted array configuration.

As mentioned before, the genetic algorithm introduced above for finding the optimal placement of the antennas in a MIMO radar configuration will be here further developed and generalized. In particular, no assumptions on the transmitter and receiver positions have been done. They can thus be placed without any restriction along the whole given PCB size.

A predefined contour for the conformal radar sensor must be given as input to the algorithm. It is indeed not possible to optimize at the same time both the sensor shape and the antenna positions. The shape of the contour can be defined in terms of the length of the projection on the x-axis and the amount of bending between the facets.

In this implementation, the genes describe the x-coordinate of the antenna positions. Since the contour shape is a known parameter, it is possible to map the x-coordinate values to generate the corresponding y-coordinates. Similarly to the previous algorithm, a chromosome describes a MIMO antenna configuration. In this implementation of the algorithm the maximal acceptable beamwidth at the broadside direction can be given as input, too.

Contrary to the algorithm of Section 3.2.2, for the optimization of a conformal MIMO configuration it is necessary to include the antenna radiation pattern, in this specific case obtained by means of full-wave simulations. For the development of a non-planar mm-wave MIMO radar series-fed microstrip antenna arrays are employed on the facets of the sensor. The radiation pattern of every array follows the conformal shape. In particular, in the simulation setup the antenna main beam must be aligned with the normal of the contour in order to correctly model the possible shadowing caused by the ground plane of the microstrip array along the conformal contour. Thus, knowing the transmitter or receiver position along the contour is mandatory for taking correctly into account the antenna radiation pattern.

To summarize, when the coupling between adjacent antenna elements is neglected, and when all transmitters and receivers are identical and placed in a planar geometry, like the basic implementation presented in the previous section, it is not necessary to include the antenna radiation pattern for analyzing a MIMO configuration. In that case all the virtual elements present the same equivalent radiation pattern, and they do not contribute to the ambiguity function properties [39], as derived also in the Appendix C. On the other hand, for a conformal MIMO configuration, due to the different orientation of the antennas along the contour, it becomes important to consider the antenna radiation pattern, too. Although the same kind of radiating element is employed for the transmitters and receivers, the differences in the antenna orientation can lead to different patterns of the virtual elements.

Also in the case of the conformal MIMO system, the mutual coupling between adjacent antenna elements has not been taken into account in the simulation framework.

The basic idea of using the AF for the definition of the fitness function has also been retained in this second implementation. A detailed description of the main steps required for the fitness function evaluation is here provided.

1. For a given chromosome, first the virtual array steering vector can be

calculated and then the AF plotted. The AF plot is handled as a square matrix, where the number of rows and columns depends on the number of the angular directions ψ_i where the steering vector, and hence the AF, is evaluated.

2. Afterward, the algorithm determines the width of the main beam in the virtual array beam pattern as an half-power beamwidth for the boresight direction. This value is then compared with the maximal acceptable beamwidth, so that chromosomes with a too large main beam become a low score in the ranking of the chromosomes.

3. If the beamwidth is an acceptable value, then the main diagonal is removed from the plot of the AF in order to exclude those points from the evaluation of the ambiguity-free area. This can be seen for example in Fig. 3.4. From the picture it can also be noticed that for angular values far away from the boresight the diagonal cannot be completely removed. Due to the broadening of main diagonal, the beamwidth calculated at the boresight fails to predict the diagonal width in the AF plot for directions away from the boresight.

4. The algorithm searches for the points of the AF plot that show an autocorrelation higher than the given threshold. For those points, the distance $d_{i,j}$ to the boresight direction is calculated as an Euclidean

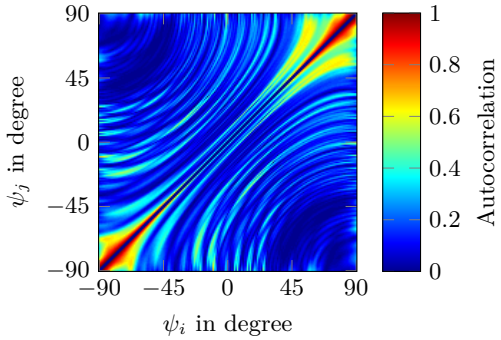

Fig. 3.4: Examplary plot of an AF where the main diagonal has been removed.

norm

$$d_{i,j} = \sqrt{|\psi_i|^2 + |\psi_j|^2}. \tag{3.2.3}$$

5. The shortest distance $d_{\min}$ is then given by

$$d_{\min} = \min d_{i,j} \;\; i,j = 1,\ldots,\widetilde{N} \tag{3.2.4}$$

where $\widetilde{N}$ represents the number of elements with an autocorrelation higher than the threshold. The minimum distance is reached at the point with coordinates $(\psi_{i,\min}, \psi_{j,\min})$. As an example, this point has been depicted in Fig. 3.5.

6. The point with coordinates $(\psi_{i,\min}, \psi_{j,\min})$ can be finally used to define the ambiguity-free area as follows

$$\text{Ambiguity-free area} = \left(2 \min\left\{\left|\psi_{i,\min}\right|, \left|\psi_{j,\min}\right|\right\}\right)^2. \tag{3.2.5}$$

With the previous equation the square centered around the main diago-

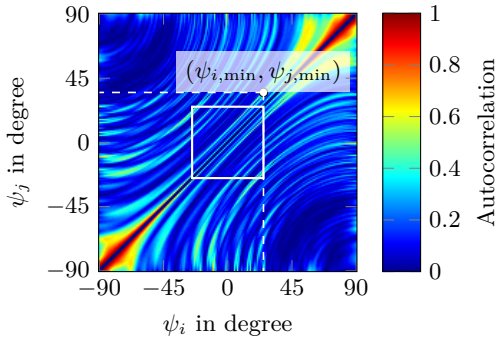

Fig. 3.5: The point at which the autocorrelation is higher than the given threshold and closest to the center of the diagonal has the coordinate $(\psi_{i,\min}, \psi_{j,\min})$. The smallest coordinate between $\psi_{i,\min}$ and $\psi_{j,\min}$ can be used to define the ambiguity-free area, which is depicted as a white square centered around $0°$.

nal can be drawn as per Fig. 3.5. As it can also be observed in Fig. 3.5, this way of obtaining the ambiguity-free area is to some extent a conservative estimate, since the closest point with a non-acceptable value of autocorrelation lies outside the ambiguity-free area.

7. The chromosomes that give a large ambiguity-free area as per (3.2.5) are rewarded with a high score in the chromosome ranking. In this way the fitness function maximizes the achievable ambiguity-free area.

In this implementation of the optimization algorithm, a second iteration for ranking the best chromosomes in the population has been introduced, and it is based on the FoV of the sensor. In this second iteration the ambiguity-free area — see (3.2.5) — and the FoV, at a given distance and for some given system parameters, are compared. Among the chromosomes with the highest scores, the algorithm rewards the antenna configurations, that give a FoV not larger than the ambiguity-free region. In this way it is possible to say the ambiguity-free area fully describes the ambiguity properties of the array, and in principle no other ambiguities can be mapped in the FoV of the sensor.

The parameters used for the calculation of the FoV according to (2.2.5) in the current algorithm implementation are the following: the transmitted power P_t is equal to 10 dBm, the RCS value σ is 10 dBsm, the noise figure F has been set to 10 dB, the temperature T is 300 K, the bandwidth B is 2 GHz, and the minimum acceptable SNR is 15 dB. The SNR of the radar can be further improved by taking into account the processing gain obtained with the coherent integration by the range-Doppler processing. To this purpose, the number of ramps has been set to 128, and the number of samples to 512.

Since the transmitters and receivers of the MIMO radar can be placed without any restriction on different facets of the conformal structure, it is in principle possible to see a non-uniform power level among the virtual channels. Indeed, according to their orientation, the various transmitter-receiver pairs can show different equivalent radiation patterns, as already mentioned above. Those amplitude differences can lead to a broadening of the main diagonal of the AF. Therefore, the antenna configurations, that can lead to such a problem, will be naturally punished by the algorithm while evaluating the population with the help of the fitness function. As already explained above, the broadening of the diagonal might cause a non perfect removal of the main diagonal, see the example of Fig. 3.4. The remaining points are recognized as elements with

a high autocorrelation, and therefore they will lead to a small ambiguity-free area and consequently, a low ranking of the chromosomes.

This point can be better understood with the two examples of conformal MIMO configurations of Fig. 3.6. The configuration on the left, namely Fig. 3.6a, is a solution that has been calculated for a threshold on the AF of 0.6 by the genetic algorithm for the given shape and the given radiation pattern of the antenna elements. It is thus an optimized solution. As it can be noticed, the transmitters are placed on one side of the contour, while the receivers occupy the opposite side. This antenna arrangement can however seem like a non-intuitive distribution. Indeed, the most natural configuration would be the one where the transmitters are more or less homogeneously distributed along the whole given contour to illuminate a broader area in front of the radar sensor, similarly to Fig. 3.6b. The configuration of Fig. 3.6b has been simply obtained by exchanging some transmitters and receivers of the optimal distribution of Fig. 3.6a, while keeping the same dimensions and shape of the contour.

Figure 3.7 presents the plots of the AF that can be obtained with the two configurations presented above. From Fig. 3.7a it can be observed that the optimal MIMO configuration gives an AF with a wide ambiguity-free range. At the same time, the modified antenna configuration, where the transmitters occupy different sides of the PCB contour, restricts the ambiguity-free range

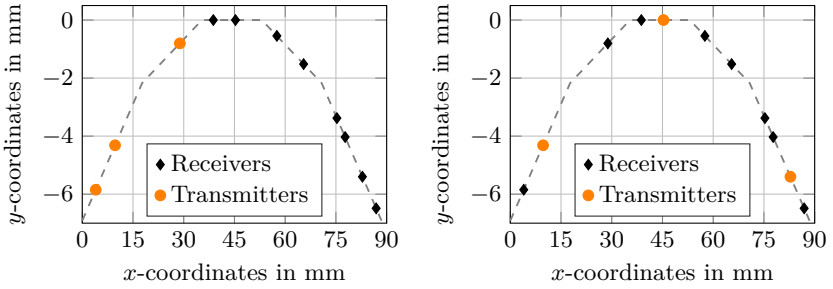

(a) Optimal configuration. **(b)** Modified configuration.

Fig. 3.6: Top view in the xy-plane of two examples of antenna configurations for a conformal MIMO radar with 3 transmitters and 8 receivers. The dashed line represents the contour of the PCB (not to scale). The configuration on the left has also been shown in [68], ©2019 IEEE.

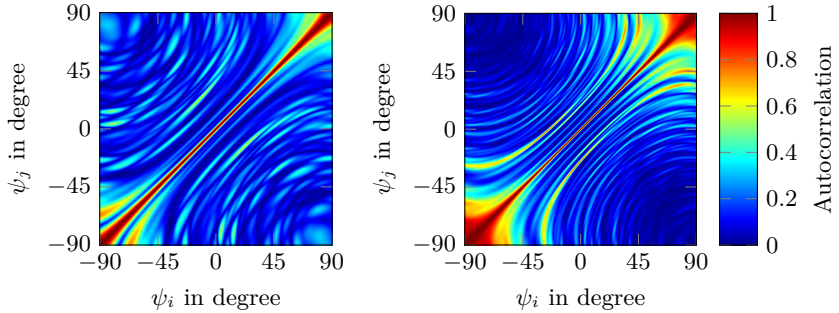

(a) Optimal configuration. **(b)** Modified configuration.

Fig. 3.7: Plot of the AF obtained using the antenna systems of Fig. 3.6. The plot on the left has also been presented in [68], ©2019 IEEE.

mainly because of the evident broadening of the diagonal arising from the non-uniform amplitude among the channels. From the comparison between Fig. 3.7a and Fig. 3.7b it can also be observed that the differences in the array geometry lead to a change in the width of the AF close to 0°. In particular, it can be concluded that although the optimal configuration shows a larger ambiguity-free range, it offers at the same time a wider main diagonal, which generates a worse angular resolution. Hence, in the design of a conformal MIMO radar a compromise between the maximization of the ambiguity-free range and the achievable angular resolution at broadside must be reached.

3.3 Experimental validation of an optimized MIMO antenna configuration

To verify the simulation results of the conformal array configurations designed with the genetic algorithm, two prototypes of conformal antenna arrays have been fabricated and tested with the help of a MIMO radar. The study presented in this section has also been partially shown in [68].

First of all, the optimized antenna configuration with 3 transmitters and 8 receivers presented in Fig. 3.6a has been developed into the prototype of Fig. 3.8. As it can be observed, the PCB with the feeding network and the antenna arrays has been glued to a plastic support realized with a 3D printer.

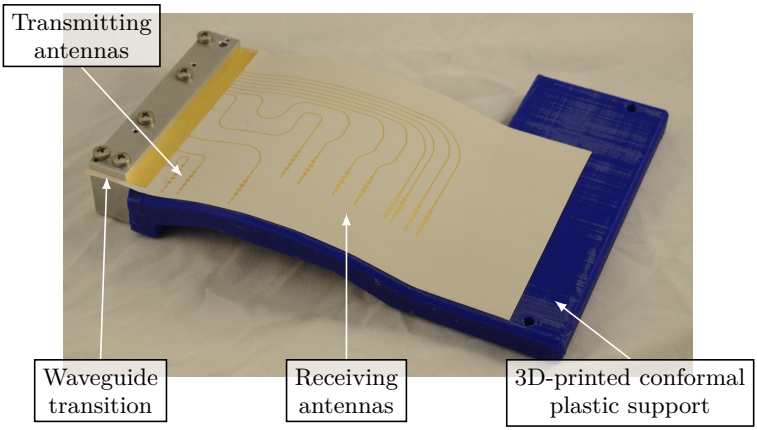

Fig. 3.8: Prototype of the optimized 3×8 MIMO antenna configuration presented in Fig. 3.6a. Picture from [68], © 2019 IEEE.

This support provides not only the necessary mechanical stability, but also the required curvature for the conformal sensor. Both the transmitting and the receiving arrays are 8-element series-fed patch arrays. The substrate employed for the PCB is RO3003 [70] with a thickness of 127 µm.

A second antenna system with a slightly different placement of the transmitting and receiving elements has also been realized with the same technology described above. It is also an optimized version calculated with the help of the genetic algorithm. In the optimization run the maximum acceptable value on the ambiguity function threshold has been set to 0.6. Figure 3.9b presents the sketch of the proposed array configuration together with the associated ambiguity function. Compared to the model of Fig. 3.6a, the configuration in Fig. 3.9a shows a little larger virtual aperture.

The antenna system has been connected through a waveguide-to-microstrip transition to the MIMO radar sensor front-end. A detailed description of the transition and of the radar has been provided in [71].

The calibration of the MIMO radar has been performed in an anechoic chamber. In particular, a corner reflector with an RCS of 9.4 dBsm has been placed at a distance of approximately 3.1 m in front of the radar sensor, which has been positioned instead on a turntable. The measurement samples have been

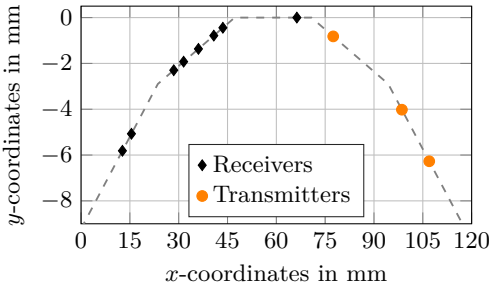

(a) Optimal configuration (not to scale).

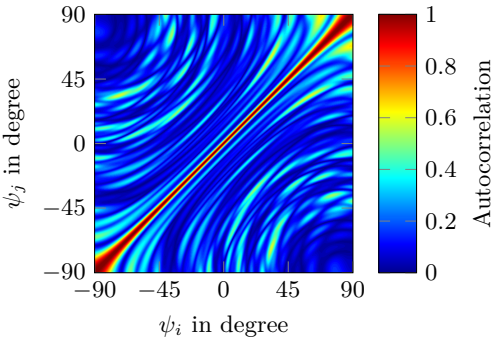

(b) Ambiguity function.

Fig. 3.9: Antenna configuration for a conformal MIMO radar with 3 transmitters and 8 receivers and the associated plot of the AF. The dashed line in the picture (a) represents the contour of the PCB. Picture from [68], ©2019 IEEE.

collected with a 0.5°-spacing on the azimuth plane while performing a sweep between −90° and +90°.

To plot the AF and to further evaluate the angle estimation capabilities of the proposed arrays, it is first necessary to generate the steering vector starting from the raw radar data. In particular, as already mentioned in Section 2.2, after a two-dimensional FFT the correct range bin of interest where the target is present must be identified. The velocity information has been ignored in this

case, since a static scenario is considered.

The correct range bin of the target has been obtained by searching for the maximum amplitude in the neighborhood of the nominal distance where the target has been placed. Since it is not possible to exactly rotate at the same time all the transmitting and receiving elements around their own phase center, a small fluctuation of the range bin index has been actually seen while scanning on the azimuth plane from -90° to $+90^\circ$.

Once the target position in the range-Doppler matrix has been identified, it is possible to extract the corresponding complex value to generate the steering vector. The next step is thus the evaluation of the AF using the measured steering vector in (2.2.4). The plots relative to the AF of the two proposed antenna systems can be seen in Fig. 3.10.

As it can be observed, the measurement results are in quite good agreement with the plots of the AF obtained by means of simulations, namely the plots in Figs. 3.7a and 3.9b. The presence of the waveguide transition on the azimuth plane, see Fig. 3.8, affects the measurements especially at large negative angular positions. The shadowing caused by the metal block reduces significantly the amplitude of the received signal. This effect can be recognized by the noisy pattern in both AF plots.

In the simulated AF it has been assumed that all the transmitters and receivers have the same power at their feeding terminals. However, as it can be noticed in the prototype of Fig. 3.8, a large feeding network with a non-constant feeding line length has been used. The substrate losses for microstrip lines printed on RO3003 substrate and working around 77 GHz are close to 1 dB/cm [15]. This can lead to some variations to the input or output powers of the transmitting or receiving arrays, respectively. Due to the normalization factor in the AF, see (2.2.4), this power mismatch can cause to some extent differences between the simulated and the measured AF.

Further single target measurements have been collected, and the results are shown in Figs. 3.11 and 3.12. As with the calibration, the steering vector should be extracted from the raw data. In this case, the range bin with the target information has been extracted by using a CFAR (constant false alarm rate) algorithm [71]. The angle estimation has been then performed with a deterministic maximum likelihood approach, which will be discussed in detail in Section 6.4.2. Since the purpose of this experimental characterization is the verification of the design strategy based on the use of the optimization algorithm, for the sake of conciseness the formal description of the DoA estimation

algorithm has been here omitted.

The beam pattern obtained after solving the DoA estimation problem can be compared to the beam pattern extracted from the simulated AF. As an example, Fig. 3.11 depicts the comparison of the simulations and the measurements collected with both prototypes for a corner reflector used as a target and placed in front of the radar at the angular direction of 0°. Also in this case, the effect of the bulky transition can be observed. In fact, the good match between

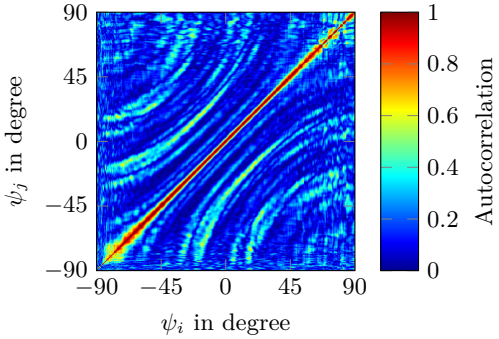

(a) Antenna array of Fig. 3.6a.

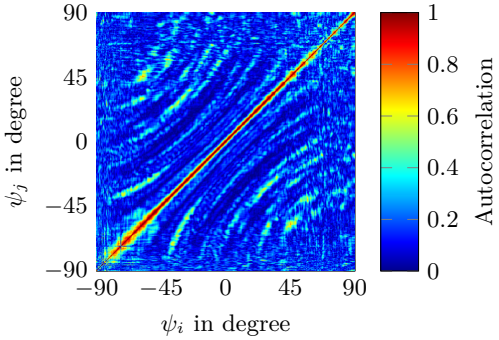

(b) Antenna array of Fig. 3.9a.

Fig. 3.10: Ambiguity function calculated in (2.2.4) with the measured steering vector. Pictures from [68], ©2019 IEEE.

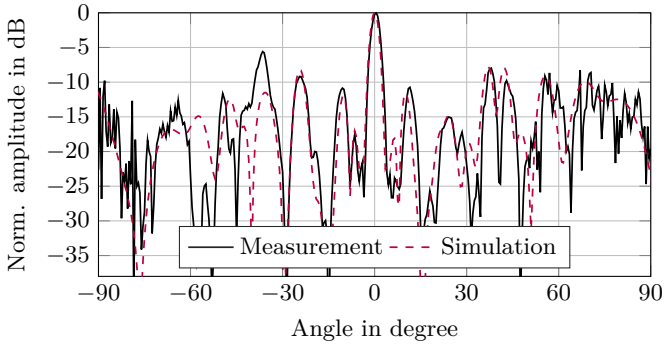

(a) Antenna array of Fig. 3.6a.

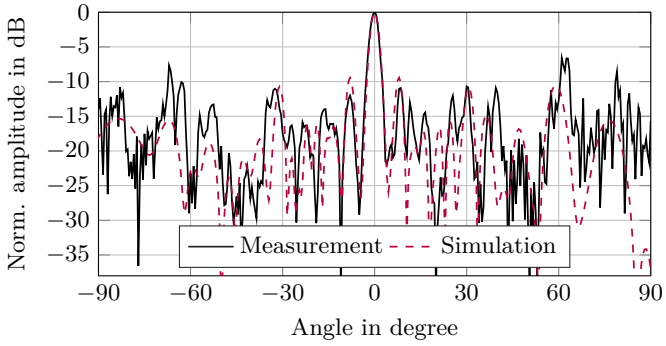

(b) Antenna array of Fig. 3.9a.

Fig. 3.11: Comparison of the simulated and measured beam pattern obtained after the DoA estimation. During the measurements a single corner reflector has been placed in front of the radar sensor at the position of 0°. Pictures from [68], ©2019 IEEE.

numerical and experimental data starts to deteriorate around −70°.

Figure 3.12 shows a further example to confirm the correctness of the proposed method. The simulation and the measurement results of the antenna configuration of Fig. 3.6a have been compared. The results refer to a target placed at a DoA of +20°. Also here, within −70° and +70° a very good

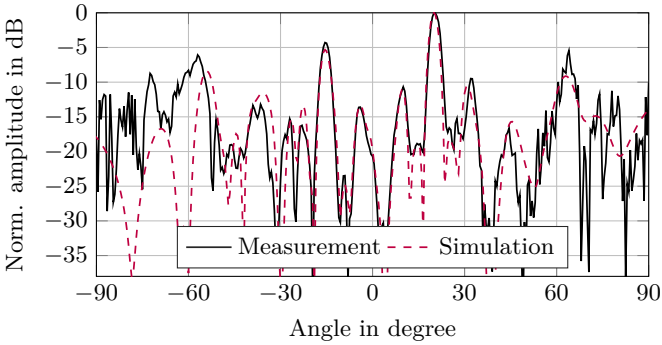

Fig. 3.12: Comparison of the simulated and measured beam pattern obtained after the DoA estimation for a target placed at the direction of +20°. Picture from [68], © 2019 IEEE.

comparison between the two curves can be noticed.

The radar measurements collected with an experimental MIMO radar sensor equipped with an optimized antenna configuration fully verified the antenna array performance predicted by the simulations. Hence, the genetic algorithm introduced in this chapter for finding an optimized antenna placement in a MIMO radar can be successfully applied. The algorithm can hence be used to design planar and non-planar mm-wave antenna systems, while taking into account the requirements on the angle estimation performance.

4 Design of wideband millimeter-wave microstrip patch arrays

Section 2.1 described the importance of developing tolerance-optimized arrays to increase the robustness of mm-wave radar sensors. Moreover, as also explained in Section 2.1, to reduce the design complexity and the unavoidable fabrication errors, standard single-layer PCB technology is the most common solution for automotive radar antenna design. This chapter deals thus with the analysis and development of wideband microstrip arrays with relatively stable performances in the whole automotive radar frequency range on a simple single-layer PCB.

Microstrip patch antennas are widely employed by automotive radar manufacturers mainly because of their low-complex design, small area occupation, and easy integration with the MMICs. Their well-know disadvantage is however the small bandwidth, which is directly related to the patch resonance mechanism [72]. A number of different methods to enlarge the bandwidth have been extensively described in the literature. Many of them rely on a dual- or multi-band design of the patch. If the sub-bands are spaced closely enough together, the multi-band behavior causes a broadening of the total bandwidth [72]. The reader can refer to [72, 73] for an exhaustive list of single-layer dual-band patch antenna designs.

While achieving a good impedance matching on a wide bandwidth is usually possible, obtaining at the same time a stable radiation performance on the whole operating bandwidth is on the other hand usually challenging. Some dual-band patch antenna designs can be at the same time actually a dual-polarized antenna design, or they do experience a quite strong variation of the radiation pattern with the frequency.

An alternative microstrip antenna array design is the grid antenna array, which has been tested and deeply investigated at 77 GHz in several works such as [74–76]. The grid antenna array can also be in principle developed on a single layer configuration. Although the measurement results available in the literature proved a good impedance matching over a wide bandwidth, the required gain and pattern stability still need further improvement.

This thesis analyzes wideband microstrip patch array designs. In particular, two different single-layer dual-frequency designs for the radiating element of the array will be presented in this chapter and compared for benchmarking with a standard patch array design, whose radiating element is the inset-fed patch antenna sketched in Fig. 4.1. The first kind of radiating element analyzed in this chapter employs two additional parasitic patches coupled to the non-radiating edges of the patch antenna [77], while the second model uses a pair of slots close to the non-radiating edges of the patch [78]. Although patch antennas loaded with parasitic elements have been used already for 77-GHz automotive radars, in particular to feed a lens antenna in a commercial LRR from Bosch [6], to the best of the author's knowledge no extensive investigations can be found in the literature about the design of larger arrays at mm-wave frequencies. As a proof of concept, the most promising antenna design will be finally integrated and tested in an 8-element array.

The designs here presented utilize as substrate for the microstrip patch antennas the Teflon-based substrate RO3003 from Rogers Corporation [70] with thickness 127 µm and a nominal value of the relative permittivity ε_r=3 . In the full-wave simulations, the loss tangent $\tan\delta$ has been set to 0.004 at 77 GHz, which is between the nominal value from the manufacturer of 0.001 and the experimental result of 0.01 shown in [15].

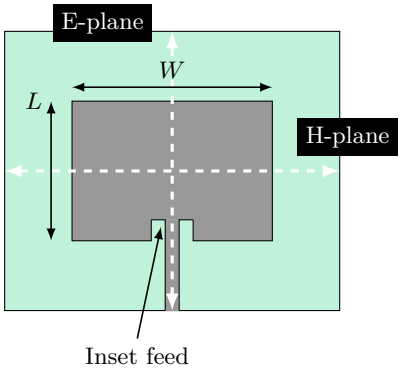

Fig. 4.1: Top view of a patch antenna with an inset feed. The white arrows describe the orientation of the E- and H-planes.

4.1 Development of wideband microstrip antennas

Full-wave simulation results relative to the two different wideband microstrip antenna designs are here shown and discussed.

4.1.1 Patch antenna loaded with parasitic patches

The sketch of a patch antenna loaded with coplanar parasitic elements can be seen in Fig. 4.2. As it can be noticed, the central patch has been fed with a microstrip line, while the parasitic patches are gap coupled with a spacing g to the central element. The parasitic patches have been placed along the non-radiating edges of the patch. They have a slightly different length compared to the central element. The lengths of the parasitic elements and of the central patch can be described by the parameters L_{par} and L, respectively.

The polarization is the same as a standard patch antenna, namely a linear polarization. Therefore, the E- and H-plane can be depicted similarly, see Fig. 4.1.

To optimize the antenna performance, different parameters can be tuned. As it can be easily understood, one of the most sensitive one is the gap width g, which controls the coupling between the patches. Figure 4.3a shows the impedance matching plotted with the help of the Smith chart while performing a sweep on the gap width. As it can be observed, when the parameter g increases, the coupling between the patches decreases, and thus the size of the loop in the impedance locus is smaller. Figure 4.3b presents the reflection coefficient as a function of the frequency. Here, it is clearly possible to observe the two reso-

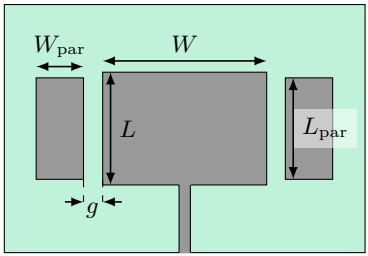

Fig. 4.2: Top view of a patch antenna with parasitic patches close to the non-radiating edges of the central patch.

nances ascribable to the central and parasitic patches. When the gap becomes too wide, it is however not possible to distinguish them anymore.

The width of the parasitic patches, described by W_{par} in Fig. 4.2, can also affect the coupling. To better understand it, the full-wave simulation results have been presented in Fig. 4.4. In particular, by looking at the Smith chart it is possible to notice that the size of the loop gets smaller when the width of the parasitic patch increases.

The other parameters that can be used to describe the model of Fig. 4.2 also

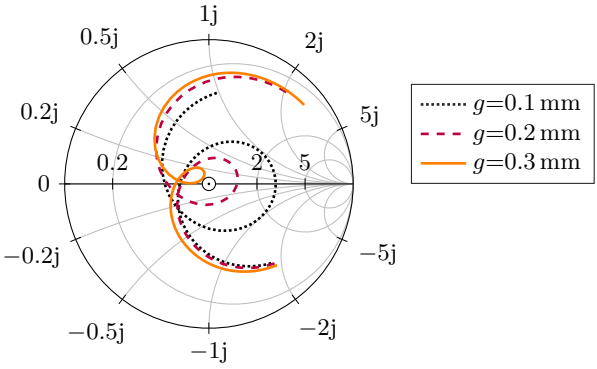

(a) Smith chart.

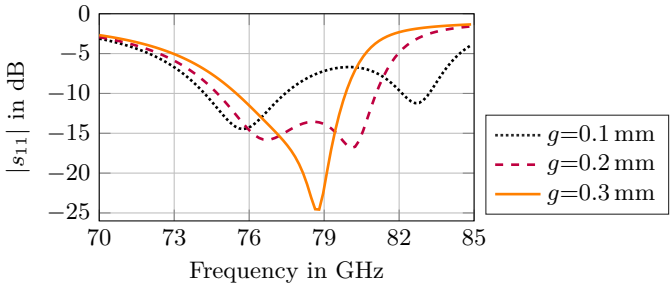

(b) Reflection coefficient.

Fig. 4.3: Full-wave simulation results while performing a sweep on the gap width g of the patch with parasitics.

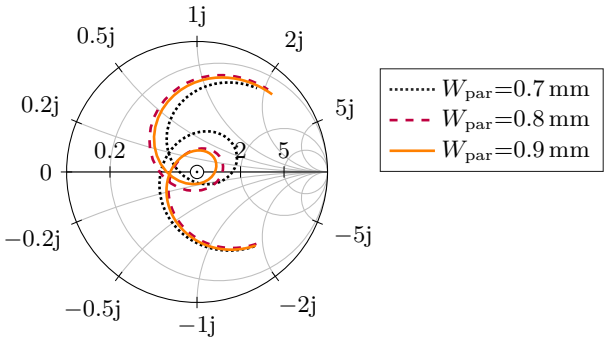

(a) Smith chart.

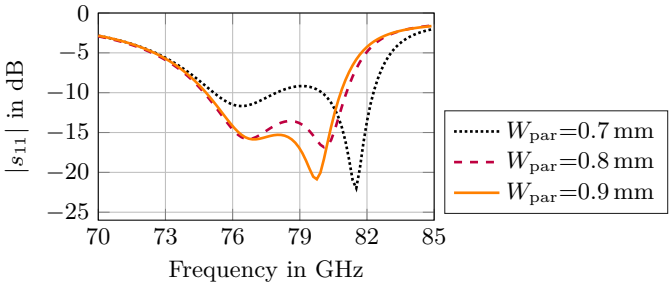

(b) Reflection coefficient.

Fig. 4.4: Full-wave simulation results while performing a sweep on the parasitic patch width W_{par}.

affect the antenna performance. However, their effect is quite straightforward, and thus their impact will be here only briefly summarized. As expected, by changing the lengths of the patches L and L_{par} the position of the two resonances can be shifted in frequency. In particular, the length L_{par} controls mainly the upper resonance frequency. The width of the central patch W can be tuned to improve the impedance matching in a similar manner to the behavior of a standard patch antenna.

It is also important to observe the shape of the radiation pattern during the parameter sweep, as depicted in Fig. 4.5. In particular, Fig. 4.5a shows the an-

tenna radiation pattern at 77 GHz while the gap g has been varied from 0.1 mm to 0.3 mm in 0.1 mm steps. When the gap increases, the sidelobe level increases as well, due to the larger distance between the three radiating elements, i.e., the central patch and the parasitic elements.

Analog conclusion can be drawn by looking at the full-wave simulation results of Fig. 4.5b. Here, a sweep on the width W_{par} has been performed. The sidelobe level increases when the width gets larger. Indeed, the patch antenna loaded with parasitic elements can be simply described as a small 3-element array. Hence, the distance between the array elements can affect the shape of

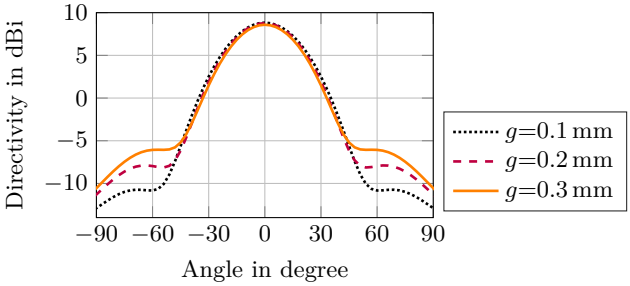

(a) Sweep on g.

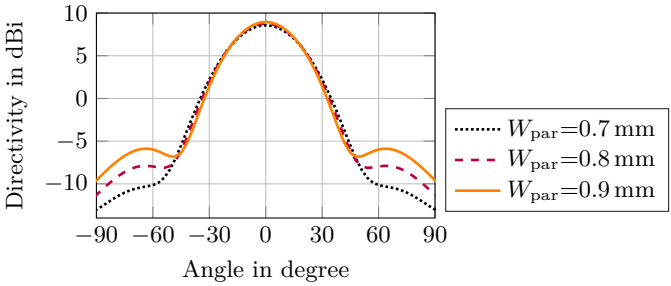

(b) Sweep on W_{par}.

Fig. 4.5: Directivity pattern in the H-plane obtained by full-wave simulations at 77 GHz while performing a sweep on the gap width g (top) and on the parasitic patch width W_{par} (bottom).

the radiation pattern. It is also expected to see a more focused beam in the H-plane compared for example to the standard patch antenna of Fig. 4.1.

4.1.2 Patch antenna with a pair of narrow slots

Figure 4.6 shows the sketch of the patch antenna with a pair of narrow slots in the top metalization. Also in this case, the feeding is a simple microstrip line. The slots are parallel to the non-radiating edges of the patch. Their length and width are equal, and they can be described by the parameter L_{slot} and W_{slot}, respectively.

Similarly to the patch antenna with parasitic elements, also in this case the bandwidth enlargement has been achieved by exploiting a dual-frequency behavior. However, the presence of the slots excites actually a higher order mode with an orthogonal polarization plane compared to the fundamental mode of the patch antenna. It means that the increased bandwidth cannot be fully utilized.

Using horizontal slots, to wit slots parallel to the radiating edges of the patch [79], or modifying the geometry of the slots as in [78, 80] are possible solutions to counteract this problem and to keep the same polarization plane even for the higher order mode. The aforementioned solutions are unfortunately not feasible for the application of interest. Indeed, using for example at the same time slots parallel to the radiating edges and a simple microstrip feeding makes extremely problematic the antenna design. The use of bent [78] or stepped slots [80] is on the other hand easier to employ. However, the achievable

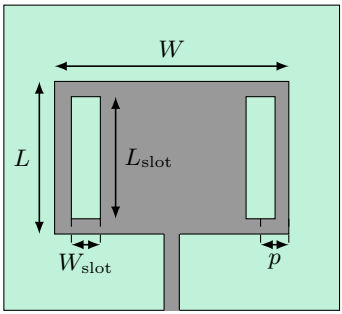

Fig. 4.6: Top view of a patch antenna with slots along the non-radiating edges.

frequency ratio between the two resonant frequencies would become too large, or in other words, the resonant frequencies would not be spaced closely enough to fit in the frequency range of interest and to see a usable band enlargement.

For the above-named reasons, the upper bound of the usable bandwidth for the slot-loaded patch antenna of Fig. 4.6 is limited by the cutoff frequency of the first higher order mode. The cross-polarization increases with the frequency and causes a non-negligible drop in the realized gain.

As it can be easily understood, the most sensitive parameters for the antenna design are those who control the slot geometry. In particular, with reference to Fig. 4.6, these are the slot length and width, L_{slot} and W_{slot}, respectively, and the distance between the center of the slot and the patch edge, described by p.

As an example, the impact of the slot width W_{slot} on the impedance matching has been analyzed, see Fig. 4.7, and on the radiation pattern, see Fig. 4.8. The slot width has been varied in the range between 0.11 mm and 0.15 mm. Figure 4.7 demonstrates that a larger slot width makes the frequency ratio between the two resonant frequencies smaller. However, as it can be noticed in Fig. 4.8, by increasing the slot width there is a significant reduction in the directivity of the antenna. The decrease in the directivity is due to the strong cross-polarization because of the excitation of the first higher order mode.

Changing the distance between the slot and the edge of the patch described by the parameter p of Fig. 4.6 leads to similar conclusions. The simulation results are here omitted for the sake of conciseness. By increasing the value of p it is possible to reduce the frequency ratio but at the cost of a smaller

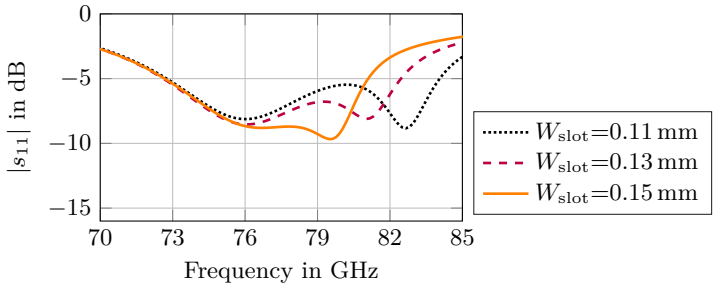

Fig. 4.7: Reflection coefficient calculated by full-wave simulations. A sweep on the slot width W_{slot} has been performed.

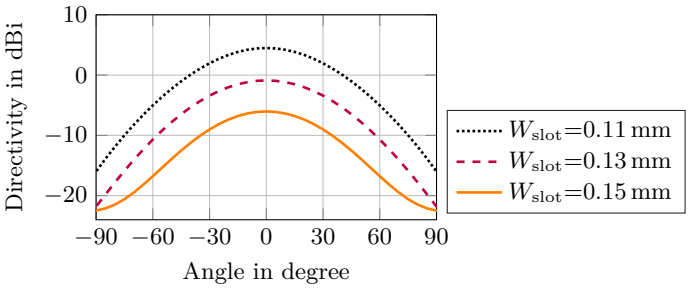

Fig. 4.8: Directivity pattern in the H-plane obtained by full-wave simulations at 81 GHz while performing a sweep on the slot width W_{slot} of the slotted patch.

value of the maximum directivity.

Similar is also the behavior that can be observed while changing the slot length L_{slot}. A longer slot decreases the frequency ratio, again at the cost of the directivity.

For the sake of completeness, the radiation patterns of the two patch antenna designs that have been here introduced should be compared. Although the results have not been obtained at the same frequency, from the comparison of the radiation pattern of the slotted patch array, see Fig. 4.8, and the array with the parasitic elements, see Figs. 4.5a and 4.5b, it can be observed that for the latter design, as expected, the beamwidth is smaller and the directivity larger.

4.2 Array design

To further verify the properties of the wideband patch antenna designs introduced in the previous section, the radiating elements have been placed and tested in a 2-element array configuration. After their performance comparison, the most promising antenna design has been further developed into an 8-element array and characterized.

4.2.1 Development of 2-element arrays

The pictures of the fabricated prototypes can be seen in Fig. 4.9. As it can be observed, not only the slotted patch and the patch loaded with parasitic

elements have been employed — see Fig. 4.9a and Fig. 4.9b, respectively — but also the patch with an inset feed has been used in the 2-element array configuration for benchmarking, as depicted in Fig. 4.9c.

The fabricated arrays have been integrated with a waveguide-to-microstrip transition for measurement purposes. Moreover, the three arrays of Fig. 4.9 are centered fed. To avoid the beam splitting, a balun has been employed to provide the required 180°-phase difference at the input ports. The reader can find further information about the design and the performance of the balun in the Appendix A, together with further details about the waveguide-to-microstrip transition.

The reflection coefficient seen from the waveguide-to-microstrip transition

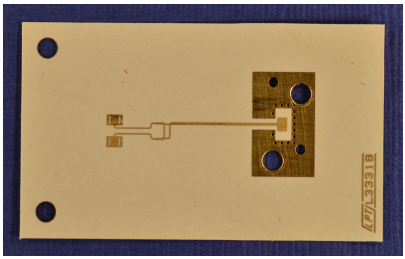

(a) Slotted patches.

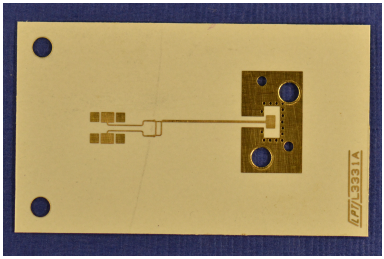

(b) Parasitic patches.

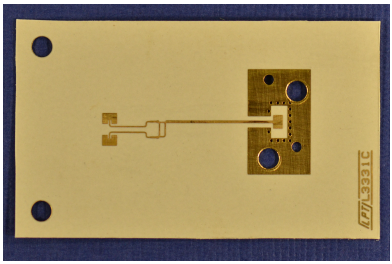

(c) Patches with inset feed.

Fig. 4.9: Photos of the fabricated 2-element arrays using different radiating elements (top view). The same kind of balun has been employed in these three examples. On the right side of the photographs the waveguide-to-microstrip transition can be observed.

has been measured, and the results can be seen in Fig. 4.10. First of all, it is important to observe that both the slotted patch and the patch loaded with parasitic elements show, as expected, a good impedance matching over a wider bandwidth compared to the patch with the inset feed. Similar results can also be seen in Fig. 4.11, which represents the amplitude of the measured s_{11} after removing the effect of the waveguide-to-microstrip transition with the time gating.

Using the gain-comparison method [81], the realized gain of the three arrays has been characterized. The results are depicted in Fig. 4.12. As expected, the array with parasitic patches has the highest gain. In an 8-GHz bandwidth the gain is quite stable, since it varies in a less than a 3-dB-wide range. Such a performance cannot be achieved using for example the standard patch array with the inset feed. However, even with the slotted patch array it is not possible to achieve a similar performance. Indeed, in this case the gain drops quickly after 80 GHz limiting thus the upper bound of the usable bandwidth.

Figure 4.13 depicts the measured radiation pattern of the three arrays at 77 GHz in the H-plane. As expected, loading a patch with parasitic elements reduces the width of the main beam compared to the other antenna configurations. On the other hand, the beamwidth of the two other arrays is quite similar in the H-plane. The non-perfectly symmetric radiation pattern can be ascribed to the presence of the bulky waveguide transition on the very same plane. Finally, the small ripples that can be noticed in the pattern are probably due to the influence of the surface wave excitation. The radiation pattern

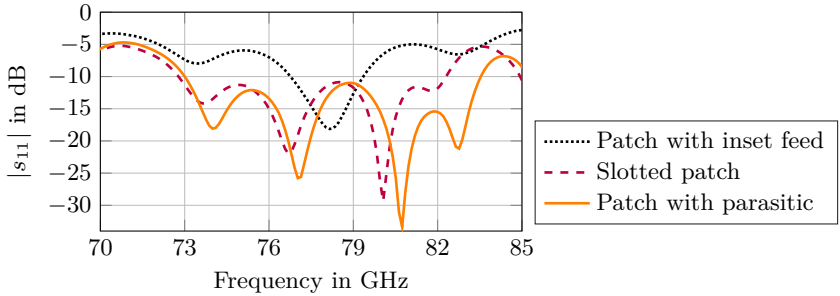

Fig. 4.10: Measured reflection coefficient of the three 2-element array prototypes of Fig. 4.9 from the waveguide-to-microstrip transition.

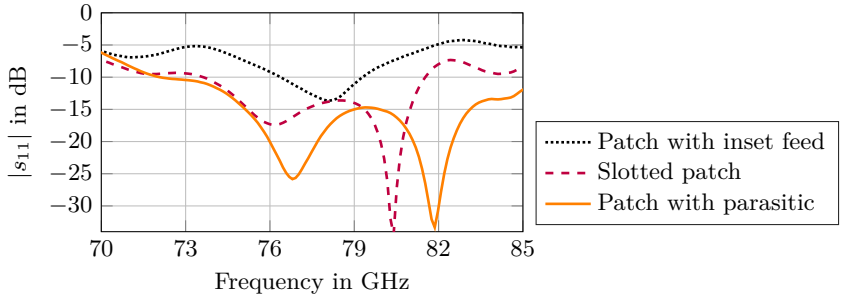

Fig. 4.11: Measured reflection coefficient of the three 2-element array prototypes of Fig. 4.9 after removing the effect of the waveguide-to-microstrip transition with the time gating.

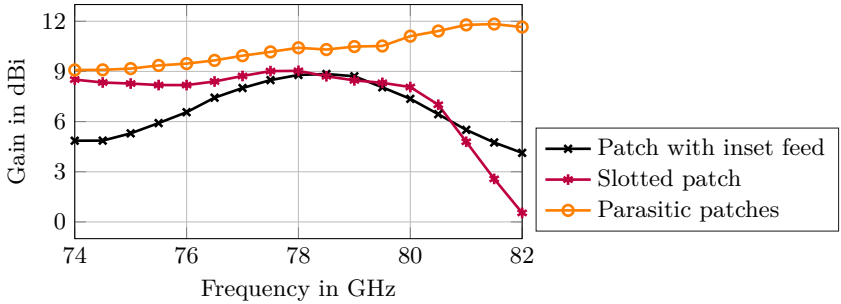

Fig. 4.12: Measured gain of the three different prototypes of Fig. 4.9.

in the H-plane has been characterized at other frequencies, too, but it is here omitted for the sake of brevity.

Figure 4.14 presents the measured radiation pattern in the E-plane of the three prototypes in the frequency range between 74 GHz and 82 GHz. The plots have been normalized to their respective maximum measured gain. The measurement results confirm once again that by employing the patch loaded with parasitic element in the 2-element array it is possible to achieve a quite stable radiation performance in a sufficiently large frequency range, as it can be observed in Fig. 4.14c. The array with parasitic patches outperforms the array with the basic patch antenna as radiating element, as it can be noticed

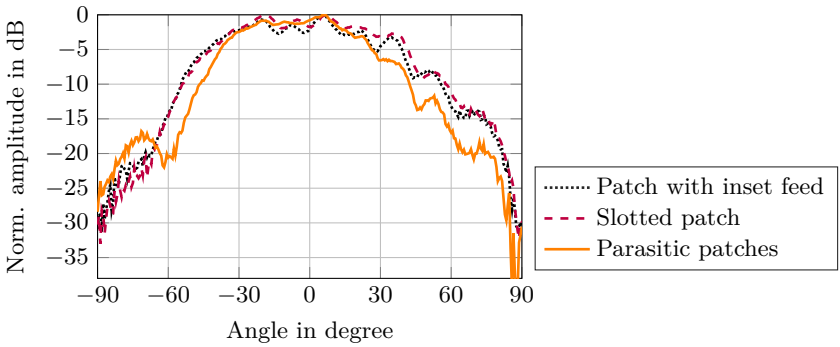

Fig. 4.13: Measured radiation pattern at 77 GHz in the H-plane for the three arrays of Fig. 4.9.

in Fig. 4.14a. On the other hand, the array with the slotted-patch elements suffers from a clear drop in the gain at higher frequency due to the excitation of the cross-polarized first higher order mode, clearly visible in Fig. 4.14b between 80 GHz and 82 GHz.

The quick investigation here presented using simple 2-elements arrays demonstrated that loading a patch with parasitic elements is a promising approach to extend the bandwidth and at the same time to keep quite stable the radiation performance over a sufficiently large frequency range. These measurement results motivate thus the use of such an antenna element in a larger array configuration.

4.2.2 Development of an 8-element array

The next step is the design of an 8-element array based on the patch loaded with parasitic elements presented in the previous section.

In an analogous manner to the previous prototypes, the proposed array is center-fed to avoid the typical beam squinting problems of the series-fed configuration often employed in automotive radar applications. Again, a balun providing 180° phase difference at the input of the two array branches has been employed. The photo of the fabricated array can be seen in Fig. 4.15. The detailed dimensions of the prototype can be found in the Appendix in the Tab. A.1. The appendix provides also a description of the employed feeding

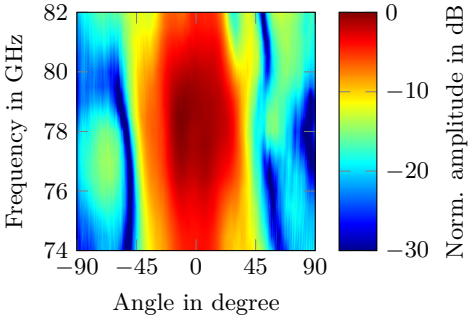

(a) Patches with inset feed.

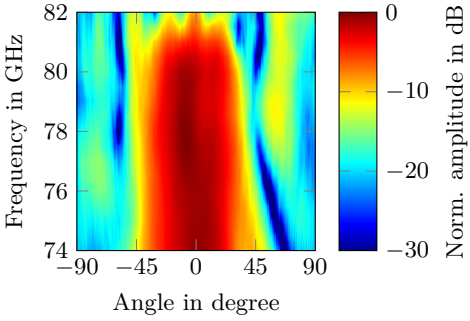

(b) Slotted patches.

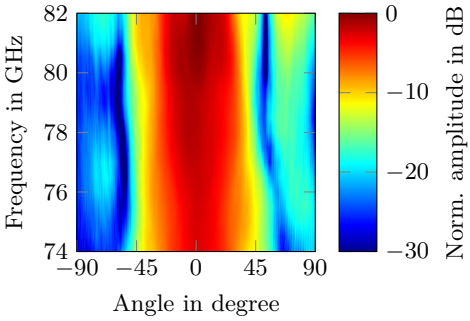

(c) Parasitic patches.

Fig. 4.14: Measured radiation pattern in the E-plane between 74 GHz and 82 GHz of the three different prototypes. The results have been normalized to the highest amplitude.

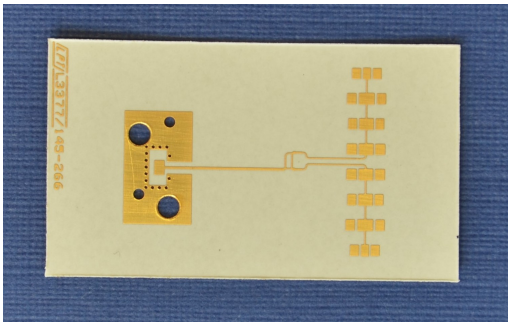

Fig. 4.15: Photo of the fabricated 8-element array integrated with a waveguide-to-microstrip transition.

network.

As it can be noticed from the picture, the structure is symmetric. Two identical branches, with the same number of antenna elements and dimensions, are fed by the balun. Every branch is a series-fed array, which consists of the repetition of a two-port patch with parasitic elements, except for the last antenna element.

The input signal coming from the waveguide-to-microstrip transition, after the balun, travels along the length of the branches. As typically done for traveling array designs, the good impedance matching of the last element avoids that part of the signal can be reflected back because of the mismatch. This signal would travel again along the array contributing to the radiation pattern of the array.

Finally, it can also be observed in Fig. 4.15 that the dimensions of the antennas along the branch are not constant. An amplitude tapering has been applied to reduce the sidelobe level in the E-plane. Due to the complexity of the basic radiating element and the unavoidable mutual coupling between the array elements, it is not straightforward to derive an analytical model for the array factor synthesis. Hence, the sidelobe level control has been simply achieved with the help of the built-in optimizer of the electromagnetic-field solver.

To understand the behavior of the array, it is important to check the transmission properties of the patches along the array, since they do affect the amplitude and phase distribution of the currents along the array. Figure 4.16 presents the

phase of the transmission coefficient for the antenna element at the beginning of the chain, i.e., close to the balun. The curve becomes pretty flat between 76 GHz and 81 GHz. This means that, after traveling along this unit cell, the phase shift added to the signal will be quite small. Similar results have been observed in the transmission coefficient of the other antenna elements in the array, too. Such a behavior is quite appealing for the unit cell of a series-fed array, since it potentially allows to obtain stable radiation performance in the frequency range of interest, due to the limited progressive phase shift along the length of the array.

The input reflection coefficient with and without the waveguide transition has been measured. In the latter case the time gating has been applied to filter out the effect of the waveguide-to-microstrip transition. The measurement results have been compared with the full-wave simulations. In particular, to agreement between the measured and the simulated results a tuning of the value of the relative permittivity ε_r has been done. Indeed, at mm-wave frequencies a significant discrepancy between the nominal and the actual value of ε_r is extremely likely. The simulation results that will be presented in the following have been calculated with ε_r=3.15.

Figure 4.17 shows the comparison between the measured and simulated reflection coefficient evaluated from the waveguide transition. The comparison is fairly good in the frequency range of interest. Similar conclusion can be drawn by looking at Fig. 4.18, which compares the measurement after applying the time gating and the full-wave simulation result without the use of the waveg-

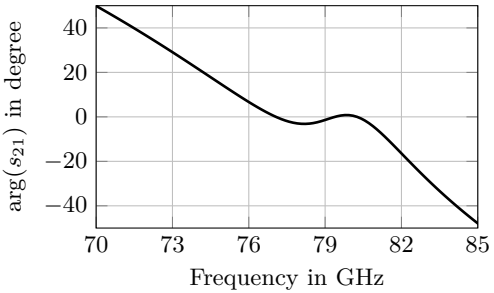

Fig. 4.16: Phase of s_{21} of the array unit cell. The antenna dimensions are the same as element 4 of Tab. A.1, page 124.

uide transition. The results demonstrate a good agreement with the full-wave simulations and a sufficiently good impedance matching in the whole frequency range of interest.

Another important step is the experimental characterization of the array radiation properties. First of all, Fig. 4.19 depicts the comparison between the measured and simulated gain of the 8-element array. Like the gain measurement of the 2-element array prototypes, also here the gain comparison method has been applied to calculate the results presented in the plot. As it can be observed, the measured gain is smaller than the value expected from the simulations, although this difference is within 2 dB between 75 GHz and 80 GHz. The measurement results confirm that using the proposed array it is possible to obtain stable radiation performances over a large frequency range, since the measured gain varies in a 2-dB range in a more than 7-GHz-wide frequency range.

The measured radiation pattern has also been compared to the simulation results, for both the E- and H-plane, as depicted in Fig. 4.20a and Fig. 4.20b, respectively. The agreement is good, and the predicted value of the sidelobe level in the E-plane has also been fairly achieved in the measurements.

Finally, the measured radiation pattern for the E-plane in the frequency range from 74 GHz to 82 GHz can be seen in Fig. 4.21. The results have been normalized to the maximum amplitude. The radiation performance are quite stable in the whole frequency range for both the beamwidth and the sidelobe

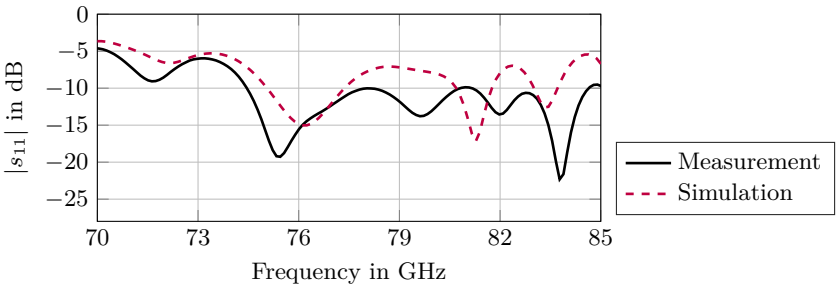

Fig. 4.17: Measured and simulated reflection coefficient of the 8-element array from the waveguide-to-microstrip transition. In the simulation the relative permittivity is ε_r=3.15.

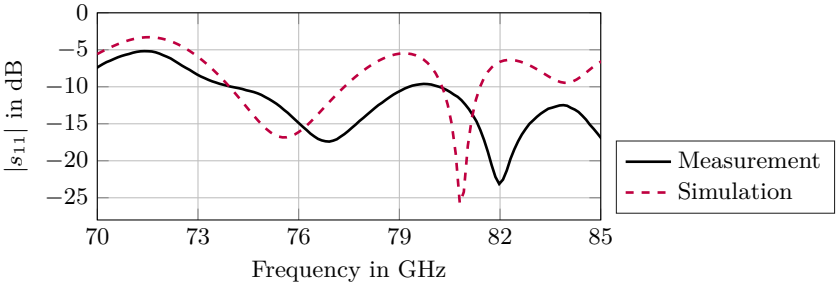

Fig. 4.18: Measured reflection coefficient of the 8-element array prototype after removing the effect of the waveguide-to-microstrip transition with the time gating. In the simulation the relative permittivity has been set to ε_r=3.15.

level. A slight increase in the sidelobe level can be only noticed at 79 GHz.

It is possible to conclude then that the measurement results demonstrated the robustness of the proposed antenna design. The sufficiently good impedance matching and the stable radiation properties over a wide bandwidth make the design a suitable candidate as antenna array for automotive applications. Compared to a series-fed microstrip array, typically employed in commercial automotive radars, the use of patch antennas loaded with parasitic elements combined with the feeding from the center of the array allows to definitely

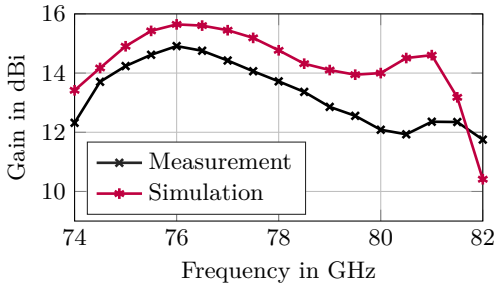

Fig. 4.19: Measured and simulated gain of the 8-element array. In the simulation the relative permittivity has been set to ε_r=3.15.

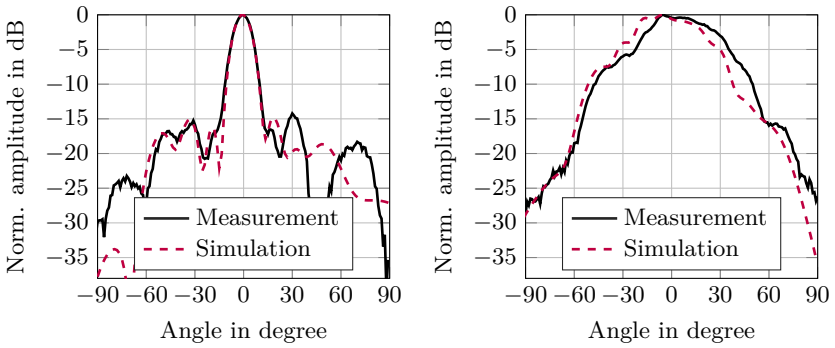

(a) E-plane. **(b)** H-plane.

Fig. 4.20: Measured and simulated radiation pattern at 77 GHz in both main cuts. In the simulation the relative permittivity has been set to ε_r=3.15.

increase the robustness of the design while retaining the simple single-layer configuration, although at the cost of a larger area occupation on the PCB.

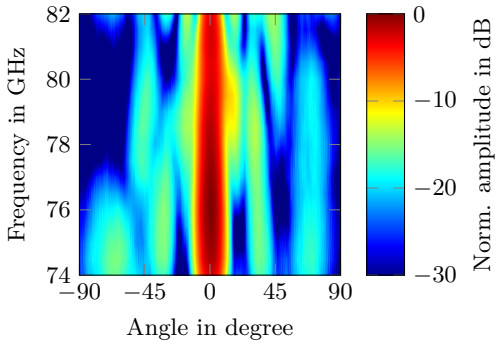

Fig. 4.21: Measured radiation pattern in the E-plane between 74 GHz and 82 GHz of the 8-element array. The results have been normalized to the maximum amplitude.

5 Millimeter-wave low-RCS antennas: fundamentals and principle of operation

The new idea proposed in this work to address the problem of the radar-vehicle integration is the development of a customized antenna design with a small RCS. To develop such an antenna system, it is important to understand the scattering properties of the antenna arrays usually employed in automotive radar applications, namely microstrip arrays. Therefore, some basics about the scattering properties of receiving antennas are explained in this chapter.

Afterward, the design principle of the microstrip low-RCS antenna is illustrated in detail.

5.1 Properties of receiving antennas

One of the most fundamental and useful theorems in the electromagnetism is the reciprocity theorem [82], that allows the antenna engineers to derive in many practical cases the transmitting properties of an antenna from its receiving properties, and the other way around. As stated in [83], the theorem sets an interchangeability in the receiving and transmitting antennas performance. Some of those properties are for example the radiation pattern, the gain, and the impedance matching [84].

However, for some specific applications an additional feature typical of receiving antennas, such as the scattering (or RCS) from the antenna, can be of great interest. A well-known recent example is the radio frequency identification (RFID), which directly exploits the backscattering characteristic of an antenna. Another possible application where the antenna scattering plays a significant role is for instance the development of stealth antenna designs for military applications.

For automotive radar applications, and in particular to understand the problem of the radar-vehicle integration, it is also important to consider the antenna RCS, since this values describes the amount of power that the antenna system of the radar sensor reflects back towards the bumper when it is illuminated by an impinging plane wave. As described in Section 2.3, the new solution pro-

posed and analyzed in this thesis is to equip the mm-wave radar sensor with a low-RCS antenna system in order to reduce the amount of power reflected back by the sensor towards the bumper, and thus to mitigate in the end the problem of multiple reflections between radar and car fascia.

5.1.1 Introduction: the antenna mode and the structural mode

To further understand the antenna scattering mechanism, consider a receiving antenna of arbitrary shape illuminated by an incident plane wave as in Fig. 5.1. As represented in Fig. 5.1a, the antenna feed can be connected to an ideal load impedance Z_l. Part of the incident power will be received by the antenna. More formally, the incident wave induces a current that causes a voltage across the feed terminal. The received power is thus absorbed by the matched load. However, part of the incident power does not reach the load, but it is directly scattered in space by the antenna depending on the RCS value σ_s, since the antenna can be described as a target with its own RCS [85]. This scattered signal is called usually *structural mode* [86] or *residual scattering* [84]. In other words, the structural mode scatter is the scatter that would have occurred if a plane wave had illuminated any body with identical shape, material, and dimension as the antenna [45].

Additionally, it is possible to consider the case of a short circuit connected to the feed of the antenna instead of the load Z_l, like the example of Fig. 5.1b. Obviously, in this case it is not possible to absorb any part of the received power,

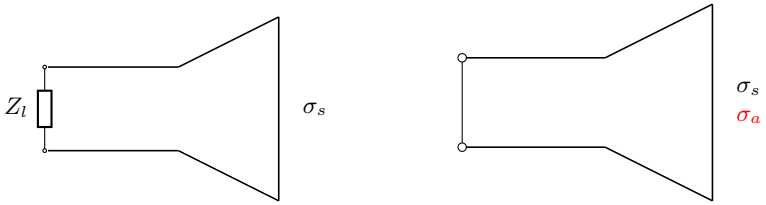

(a) Ideal matching. **(b)** Short circuit.

Fig. 5.1: General antenna with an ideal matching (left) and short circuit (right) at the feed terminals; this representation is based on [85]. The terms σ_s and σ_a represent the RCS of the structural mode and the antenna mode, respectively.

that will be instead reradiated by the antenna after being reflected back by the mismatch of the short circuit. The power is reradiated with the same pattern as the radiation pattern of the antenna [84], and in this case the signal is defined as *antenna mode* [86] or simply *reradiation* [84]. In a similar manner to the structural mode, the antenna mode can be described by the RCS value σ_a. It can be concluded that, if the antenna has a short circuit at the feed terminals, it scatters back in space some power due to the mismatch, i.e., an amount of power proportional to σ_a, plus the power that depends on the structural mode, which is independent of the actual load at the feed. It is widely accepted to assume that the structural mode and the antenna mode are independent [86].

In general, when a non-ideal load is connected to the port of the antenna, the total scattered field is the superposition of the scattering due to the structural mode and antenna mode, which in turn depends on the mismatch at the load. If an arbitrary reference plane has been defined, then σ_s and σ_a are complex quantities, and the total scattered field depends also on the phase difference between the two modes.

Once the concepts of scattered and received (or absorbed) power have been explained, for the sake of completeness let the absorption efficiency η of an antenna be defined as the ratio between the absorbed power and the sum of absorbed and scattered power. The absorption efficiency can be defined in terms of cross-sections [84]. To this purpose, let the value σ_{abs} be the absorption cross-section, which is related to the amount of incident power absorbed by the load. Then according to the previous definition, the absorption efficiency is expressed by

$$\eta = \frac{\sigma_{\text{abs}}}{\sigma_{\text{abs}} + \sigma_s + \sigma_a} \,. \tag{5.1.1}$$

The efficiency η is always bounded between 0 and 1. In case of an ideal matching such as in Fig. 5.1a, the value of the antenna mode cross-section σ_a is 0, it means thus the amount of power absorbed by the load is only limited by the structural mode of the antenna. On the other hand, in the case of a short circuit at the antenna feed terminals as in Fig. 5.1b the incident power cannot be absorbed, leading consequently to both σ_{abs} and η equal to 0. To avoid any misunderstanding, it is important to notice that the absorption efficiency is not related to the well-known concept of antenna efficiency, which is on the other hand one of the interchangeable properties of transmitting and receiving antennas that can be described with the help of the reciprocity theorem. The

absorption efficiency is a unique property of receiving antennas.

It is interesting now to analyze the scattering properties of the typical antenna systems employed in a mm-wave automotive radar. Hence, the antenna mode and the structural mode must be deeply analyzed. It has been already extensively described in the previous chapter, that microstrip patch arrays are the most common choice as radiating elements in such application. For the purpose of this thesis it is thus sufficient to focus only on this family of radiators.

The numerical results presented in [87] show that the absorption efficiency of a patch antenna is almost zero. Similar results have been obtained in [88], although for other kinds of planar antennas. In both works, the results are collected at relatively low frequencies, since the highest frequency is 11 GHz. These results are however not surprising, since it is easy to imagine that the presence of a large ground plane makes the structural mode significantly larger than the antenna mode, and hence the absorption efficiency small.

In the following, the receiving properties of a mm-wave microstrip array will be experimentally verified, and the main outcomes will be presented.

Before moving to the measurement results, it is important to add a fundamental remark. From the aforementioned literature results it is possible to conclude that the structural mode is the dominant component in the scattering cross-section of a microstrip patch array. In other words, the antenna mode can be neglected. Reducing the structural mode of a patch array is thus sufficient to reduce in turn the RCS value of the antenna array. For the specific application, i.e., the development of a low-RCS antenna system to be used in an automotive radar, this is a key point, since it means that the exact knowledge of the actual impedance matching of the array is not necessary for achieving a suitable low-RCS counterpart. The measurement results, that will be shown in the following of this work, will also confirm the results of the scientific literature.

5.1.2 Terminology

The current and the following chapters present several simulation and measurement results to investigate the echo characteristics of microstrip antennas.

Taken from the radar standard terminology [45], in this work the word *backscattering* is used to describe the monostatic scattering from an antenna.

The absolute RCS value of the different antenna systems presented in this thesis has not been calculated. On the other hand, only relative RCS values have been provided. Indeed, it is usually sufficient to show only the amount

of the *RCS reduction* to demonstrate and verify the low-RCS property of the proposed antenna designs.

Typically, if the results have been obtained by means of an experimental characterization, the relative RCS, namely the reciprocal of the RCS reduction, is calculated with respect to a reference metal plate or a reference antenna. Only in a really limited number of cases the measurement results have not been normalized to a reference structure. However, from a physical point of view they still represent a normalized value, since they have been collected with the help of a VNA, which compute them as S-parameters. Alternatively, when the RCS reduction has been determined by an electromagnetic-field solver software, it is always shown as a normalized quantity, since the result computed by the software are given in most of the cases automatically as a ratio of incident and reflected fields.

Hence, the RCS reduction is presented in this work as a normalized quantity. Due to this normalization, the RCS reduction can also be described as a *reflection coefficient*. This should not be confused of course with the input reflection coefficient, or s_{11}, of an antenna.

Therefore, the terms backscattering, RCS reduction, and reflection coefficient are used interchangeably in the next sections.

5.1.3 Characterization of the antenna mode and the structural mode of microstrip arrays

By changing the load connected to the input port of an antenna illuminated by a plane wave, it is possible to investigate the contribution of the structural mode and the antenna mode on the total scattered field. From the previous comments on the properties of receiving antennas, it should be now clear that, if the antenna is connected to a short circuit, the antenna mode can be maximized, while with a conjugate matching it can be minimized.

Therefore, to characterize the scattering of a microstrip patch array at mm-wave frequency the setup of Fig. 5.2 has been used.

In this setup, the antenna under test (AUT) is connected first to an E-band[1] waveguide variable attenuator. At the time of the characterization of the AUT only a V-band [2] waveguide variable phase shifter was available in the measurement facility. Hence, the output port of the waveguide attenuator has been

[1] The E-band extends from 60 GHz to 90 GHz.
[2] The V-band extends from 50 GHz to 75 GHz

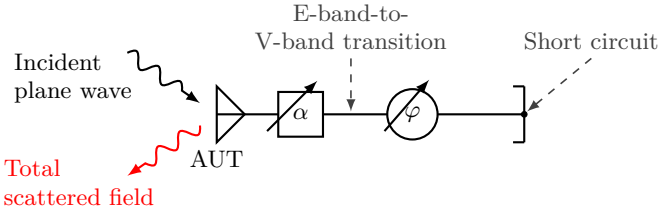

Fig. 5.2: Measurement setup for the characterization of the scattering from the AUT. The setup is composed of the AUT, a variable attenuator (α), an E- to V-band waveguide transition, a waveguide variable phase shifter (φ), and a short circuit. This measurement setup has been presented for the first time in [43], ©2018 IEEE.

connected to the V-band phase shifter with a short circuit at its second port. As it can also be seen in the sketch of the measurement setup, an E-to-V-band waveguide transition has been placed between the attenuator and the phase shifter. By changing the settings of the attenuator and the phase shifter, it is possible to control the impedance matching of the array, in terms of both amplitude and phase. The setup of Fig. 5.2 is a more flexible and powerful realization of the simple versions presented in [89, 90].

The phase shifter adjusts the phase in coarse discrete steps. It has been experimentally characterized to check its performance in the E-band, so outside its specified range. At 77 GHz the phase difference when moving from the start position to the next one was $-40°$, the successive was $-60°$, and the last one $-62°$.

The measurements have been conducted in an anechoic chamber. In particular, the backscattering has been measured by a 25-dBi standard-gain horn antenna connected to a VNA and placed 2 m apart from the AUT. It is a monostatic measurement setup, in which the horn antenna has also been used as transmitting antenna to illuminate the AUT. To collect only the signal of interest, that is to say, the signal reflected back by the AUT, the time gating feature of the VNA has been applied. More details about the measurement setup and the use of the time gating can be found in Chapter 6.

The AUT is a 10-element series-fed microstrip array. The fabricated prototype is shown in Fig. 5.3. Similarly to the antenna design of Chapter 4, the used substrate is RO3003 from Rogers Corporation [70] with a thickness of



Fig. 5.3: Fabricated series-fed microstrip patch array integrated with a waveguide-to-microstrip transition. The waveguide and the flange have been milled in an aluminum block. Photo from [43], ©2018 IEEE.

127 µm and a nominal value of the relative permittivity ε_r=3. For measurement purposes the array has been integrated with a waveguide-to-microstrip transition, which has been covered by absorber material during the measurements. Details about the design and fabrication of the transition are given in the Appendix A.3 on page 126.

Figure 5.4 presents the measurement results collected by the horn antenna while changing the attenuation of the variable attenuator and by keeping constant the phase of the phase shifter. The plot demonstrates that the amplitude

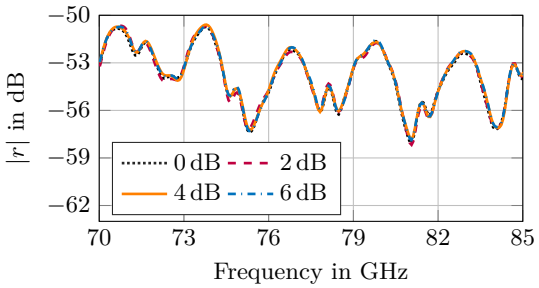

Fig. 5.4: Measured backscattering from the AUT by changing the attenuation of the variable attenuator in the setup of Fig. 5.2. These results have been presented in [43], ©2018 IEEE.

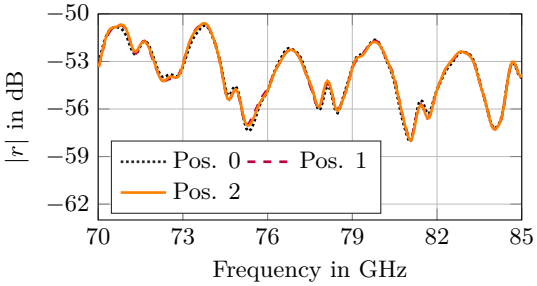

Fig. 5.5: Measured backscattering from the AUT by changing the phase of the variable phase shifter in the setup of Fig. 5.2.

of the backscattering, namely the amplitude of the reflection coefficient r, is not affected by the differences in the load matching. Similar results have been obtained when the attenuation from the variable attenuator has been kept constant to 0 dB, and only the phase of the variable phase shifter has been modified, as depicted in Fig. 5.5.

The experimental results confirmed that the antenna mode of a mm-wave microstrip array is negligible compared to the antenna mode. As a consequence, the impedance matching at the input port of the array can be ignored while investigating the array scattering properties.

5.2 A proof of concept: development of a low-RCS surface

Before presenting the principle of operation and the design of the microstrip low-RCS antenna array developed in this thesis, it is first of all important to understand the behavior of the low-RCS surface that has been presented originally by [91]. This surface is the starting point for the design of the low-RCS antenna that will be introduced in the next section and then analyzed in detail in Chapter 6. Based on the idea of [91], a low-RCS surface for mm-wave frequencies has been developed and presented in [92], and the main results will be discussed here thoroughly.

5.2.1 Surface design

The low-RCS surface is composed of a periodic repetition of a unit cell. As it can be seen from Fig. 5.6, the unit cell itself consists of a periodic displacement in a chessboard-like manner of an artificial magnetic conductor (AMC) and a perfect electric conductor (PEC). This combination of AMC and PEC is a simple and elegant way to strongly reduce the RCS of the surface compared to an equal-sized metal plate.

Indeed, an AMC mimics the behavior of a magnetic conductor, because at the resonance frequency the reflection phase is 0°, i.e., the reflection coefficient is +1. This property is complementary to a PEC, and since in nature a perfect magnetic conductor does not exist, it can be adequately described by the word *artificial* [93].

When a plane wave illuminates the surface, a phase compensation effect or a cancellation effect of the AMC and PEC contributions can be observed. Specifically, due to the presence at the same time of an AMC and a PEC a destructive interference takes place in the backscattered wave. This results in a strong reduction in the amount of power reflected back in the normal incidence direction.

The first model of the low-RCS surface presented in [91] used as AMC a squared patch connected to the ground through a metallic via, also known as

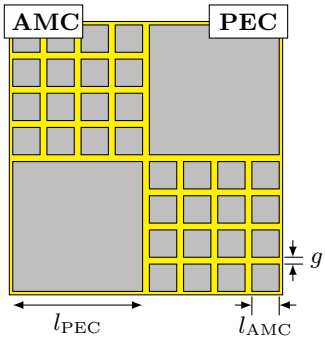

Fig. 5.6: Unit cell of the chessboard-like low-RCS surface according to [92]. The dimensions are the following: l_{AMC}=0.88 mm, l_{PEC}=3.94 mm, g=0.14 mm.

AMC-Sievenpiper structure or *Sievenpiper mushroom* structure. The pioneer work of Sievenpiper in [94] paved the way for the use of the AMC as a new high-impedance surface (HIS). His work focused mainly on a surface texture based on patches connected to the ground by vertical vias. However, to simplify the fabrication, it is appealing to omit the grounding vias. As it can be easily understood, avoiding a huge number of vias is particularly important for mm-wave applications, where the use of vias can increase the cost, the complexity, and the possible fabrication errors of the device. For this reason, in the model investigated in [92] and depicted in Fig. 5.6 no vias are present. The absence of vias does not actually modify the reflecting properties of the surface. To understand this point, the basic properties of HIS and AMC should be recalled.

The terms HIS and AMC to describe the Sievenpiper's surface highlight the properties of reflecting an incident wave with 0° phase at a specific frequency. However, this kind of metasurface presents also an electromagnetic bandgap (EBG). This concept describes the ability of the structure to stop the propagation of surface waves traveling at the surface interface [93]. Or, in other words, the EBG is the frequency range where complex solutions of the Maxwell equations exist [93]. Removing the vias modifies the EBG properties of the surface, but not the reflection phase. It means that even without using the vias an AMC can be properly realized.

The amplitude of the RCS reduction for a chessboard-like low-RCS surface can be calculated with the following equation based on the approximated model presented in [95]:

$$|r| = 10 \log \left| \frac{A_{\mathrm{AMC}} \mathrm{e}^{\mathrm{j}\varphi_{\mathrm{AMC}}} + A_{\mathrm{PEC}} \mathrm{e}^{\mathrm{j}\varphi_{\mathrm{PEC}}}}{2} \right|^2 \mathrm{dB}\,, \tag{5.2.1}$$

where A_{AMC} and A_{PEC} are the amplitudes and φ_{AMC} and φ_{PEC} the phases of the reflection coefficients of AMC and PEC, when they are illuminated by an incident plane wave. The RCS reduction has been expressed as the reflection coefficient r. Since the surface is composed of two subsections, namely the AMC and the PEC, with equal dimensions, the RCS reduction can be calculated by taking the average of the reflection coefficients of the two subsections. In the ideal lossless case, the amplitudes A_{AMC} and A_{PEC} are both equal to 1, and thus the highest RCS reduction can be achieved when the difference between φ_{AMC} and φ_{PEC} is equal to 180°. The equation (5.2.1) presented above is based on a simplified model, that for example does not take into accounts

the edge effects [95] or the coupling between the AMC and the PEC sections. However, the formula is still a useful guideline for starting the design of such metasurfaces.

As explained in [96], the equation (5.2.1) can also be derived starting from the classical array theory. The underlying assumption is that the basic components of the metasurface, in this case namely the AMC and the PEC, can be considered as independent radiating elements that belong to the same array when illuminated by an incident plane wave. The excitation amplitude of the two basic components, that would be required for the formal derivation of the array factor, is then directly related to the scattered electric field, and consequently to the RCS.

Another equivalent way of describing the behavior of the chessboard-like metasurface is based on the concept of scattering centers. As stated for example in [97], an electrically large target can be modeled by a set of discrete scattering centers contributing independently to the total scattered field. The electric field individually scattered by those points, that can be described in terms of amplitude and phase, adds up giving the resulting total scattered field [98]. By taking the coherent sum of the contribution from the scattering centers, it is possible to calculate the RCS of the target [45]. In other words, the total backscattering can be obtained by a phasor addition of the scattered field of the single scattering centers. The equation (5.2.1) hence can also be seen as a normalized coherent summation of the contribution from two scattering centers, i.e., the AMC and the PEC.

Figure 5.7 further describes the properties of the low-RCS surface. In particular, the picture in Fig. 5.7a presents the reflection phase of the AMC from full-wave simulation results, the constant reflection phase of the PEC, and the phase difference between them. As it can be noticed, when the phase difference in Fig. 5.7a is equal to 180°, a strong RCS reduction can be observed at the very same frequency in Fig. 5.7b. Moreover, when the phase difference is in the range $\left[145^\circ, 215^\circ\right]$, the RCS reduction reaches at least 10 dB. The frequency range in which this condition is satisfied is highlighted in gray in the plot. These results refer to a square metal patch used as AMC simulated with periodic boundary conditions and with the same dimensions as the AMC in Fig. 5.6. The same substrate of the prototype presented in Fig. 5.3 has been used.

The mechanism of the phase compensation provides a strong RCS reduction in a specific angular direction, in particular the RCS decreases significantly in

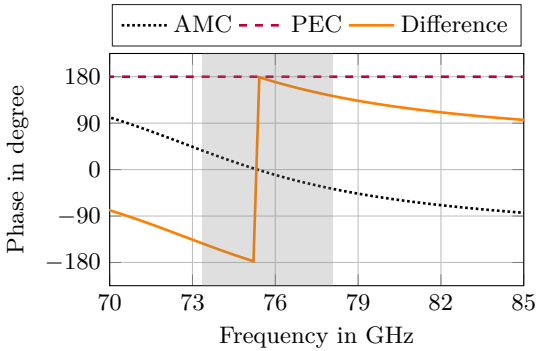

(a) Reflection phase of the AMC and PEC and wrapped phase difference between them.

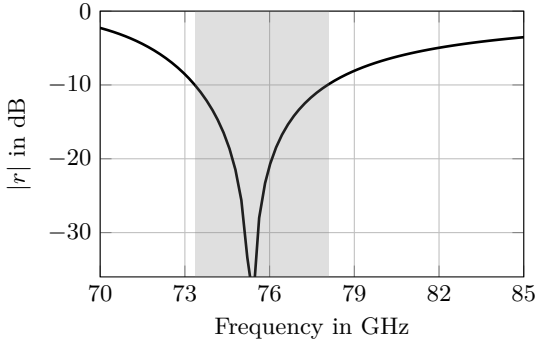

(b) Estimated RCS reduction using (5.2.1).

Fig. 5.7: Simulation of the AMC and PEC to demonstrate the principle of operation of the low-RCS surface. When the phase difference in the top picture reaches 180°, a strong RCS reduction is achieved in the lower picture. The shaded area highlights the range in which it is possible to achieve at least 10 dB of RCS reduction. Results from [92], © 2016 IEEE.

the boresight direction when a plane wave impinges on the surface in the normal incidence case. This behavior is apparent from the farfield plot of Fig. 5.8,

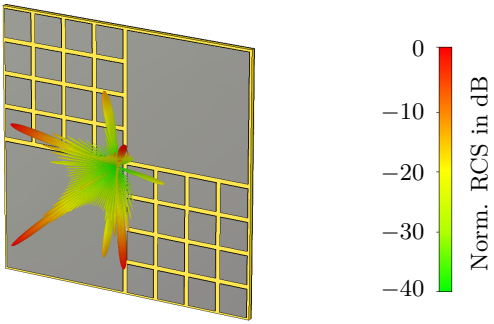

Fig. 5.8: Simulated normalized 3D-bistatic RCS at 77 GHz for a plane wave incoming from the normal incidence direction [92], © 2016 IEEE.

which represents the bistatic RCS generated by means of a full-wave simulation at 77 GHz, when a plane incoming from the normal direction illuminates the structure. The farfield plot has been calculated by multiplying the pattern of the unit cell presented in Fig. 5.6 with the array factor of a surface composed of 10×10 chessboard-like unit cells. As it can be noticed from the picture, while the amplitude can be significantly reduced for the boresight direction, it increases for others. In particular, four beams with equal high amplitude can be observed. This plot demonstrates that the surface redirects the energy of the impinging wave in directions other than the normal one. For the sake of completeness, it must also be mentioned that no absorption phenomena — like the HIS design presented in [99] — are required for achieving a good RCS reduction.

The RCS reduction presented in Fig. 5.7b has been estimated with the simplified approach of (5.2.1). In order to evaluate the discrepancy between the simplified model and the full-wave results, it is then interesting to calculate with a full-wave simulator the backscattering for the normal incidence case. To this purpose, the black dotted curve in Fig. 5.9 is presented. It can be noticed that the minimum in the plot has been slightly shifted towards higher frequencies compared to Fig. 5.7b. However, it is still possible to observe the good reduction in the RCS already seen in the previous result.

The full-wave simulation results presented in Fig. 5.9 permits also to investigate the effect of the etching inaccuracies on the RCS reduction. In particular,

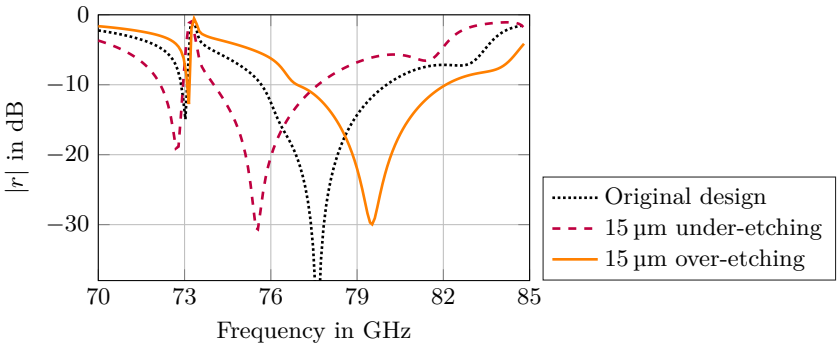

Fig. 5.9: Full-wave simulation results of the backscattering from the chessboard-like surface in the normal incidence case. The effect of PCB fabrication errors on the performance of the low-RCS surface have been investigated, too. Results from [92], © 2016 IEEE.

by considering 15 µm of under- and over-etching, which are typical values of etching tolerances as also mentioned in Section 2.1 on page 7, the fabrication inaccuracies cause a frequency shift of less than 3% with respect to the results obtained with the ideal design. Additionally, even in the worst cases it is possible to achieve at least 5 dB of RCS reduction in the frequency range of interest.

The plot of Fig. 5.9 makes also another important comment about the proposed full-wave simulation results possible. By comparing the aforementioned plot with Fig. 5.7b it can be seen that an additional minimum around 73 GHz is present. This minimum is rather insensitive to over- and under-etching, since it is quite stable in frequency compared to the resonances at higher frequencies. In the full-wave simulation a large number of higher order modes must be taken into account, since a waveguide port with the same dimension as the chessboard unit-cell has been employed. When a higher-order mode becomes able to propagate, a resonance around its cutoff frequency can be observed, and this generates the simulation artifacts of Fig. 5.9. The over- and under-etching do not change the total outer dimensions of the unit cell. Further comments about the full-wave simulation setup to better understand possible simulation artifacts will be given in Section 5.3.1.

5.2.2 Experimental results

To verify the properties of the low-RCS surface, a prototype has been fabricated and tested. A picture of this structure can be seen in Fig. 5.10. It is composed of 10 × 10 unit cells with the same dimensions of Fig. 5.6. To increase the mechanical stability of the structure, an FR-4 support has been glued on the back side of the high-frequency substrate below the ground plane. The visual inspection showed approximately 15 µm etching tolerances.

The measurement setup will be discussed in detail in the next chapter, and for this reason the measurement results will be presented to understand the feasibility of the proposed approach at mm-wave frequencies, in particular with respect to the fabrication accuracy and the development of a suitable measurement setup. Indeed, the proposed surface is composed of many long thin slots that divide the AMC and PEC cells, which can be hard to realize accurately with standard photo-etching process at high frequencies.

First of all, the backscattering for the normal incidence case has been measured and compared with the full-wave simulation results. The results are depicted in Fig. 5.11. It can be noticed that a good agreement is obtained. The measured minimum of the reflection coefficient is shifted by less than 1 GHz towards lower frequencies with respect to the simulation results. The measured bandwidth, where at least 10 dB of RCS reduction have been achieved, is approximately 6 GHz wide and centered around 76.8 GHz. The measurement proves that the proposed structure is able to achieve 17 dB of RCS reduction at 76.8 GHz in the boresight direction compared to an equal-sized metal plate.

The oblique incidence case has also been experimentally evaluated. To this purpose, the surface has been placed on a turntable in an anechoic chamber, in order to collect the measurements while performing a sweep on the azimuth plane. As an example, the results for 76.8 GHz and 78.0 GHz can be seen in Fig. 5.12. First of all, the plots confirm again the strong RCS reduction of the low-RCS surface compared to a metal plate for the direction of 0°, namely for the boresight direction. It can also be observed that roughly between −15° and +15° the amplitude of the backscattering from the metasurface is smaller than the one of the PEC, but outside this range the amplitude increases. The results show thus clearly the redirection of the incident wave towards the directions far away from the boresight. In particular, two peaks with a high amplitude can be observed at −29° and at +27°. The non-perfectly symmetric patterns in the two plots are related to minor positioning inaccuracies during

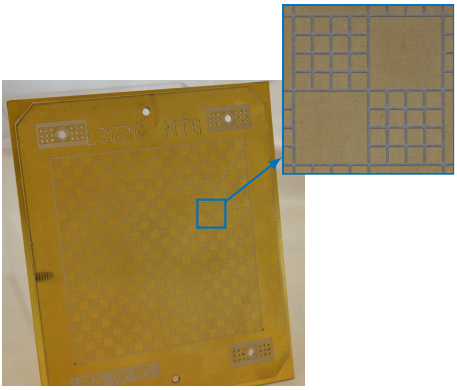

Fig. 5.10: Photo of the fabricated prototype of the low-RCS surface. The enlarged view of one unit cell can be seen in the top right corner. The outer part of the PCB has been covered by absorber material during the measurements.

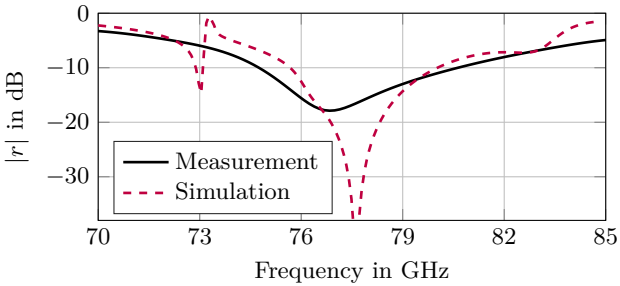

Fig. 5.11: Comparison of the measured and simulated backscattering from the low-RCS surface for the normal incidence case. The measurement result has been normalized to the result of a measured equal-sized metal plate [92], ©2016 IEEE.

the measurements.

The investigation presented in this section demonstrated the feasibility of the design at mm-wave frequencies of a low-RCS surface that exploits the mutual phase compensation of two basic components, namely the AMC and the PEC.

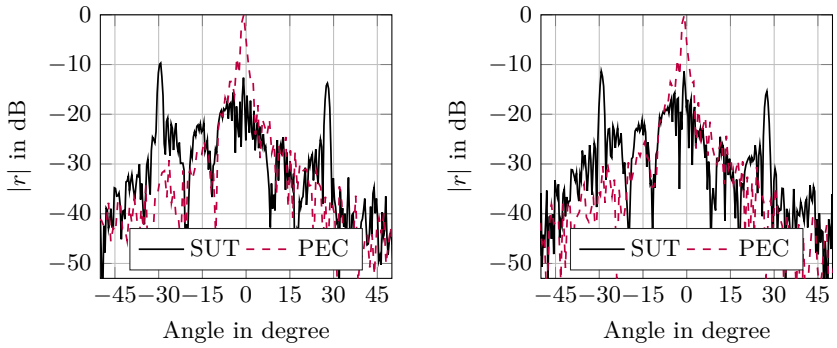

(a) 76.8 GHz. **(b)** 78.0 GHz.

Fig. 5.12: Normalized amplitude of the backscattering from the surface under test (SUT) and an equal-sized metal plate for the oblique incidence case [92], © 2016 IEEE.

This promising approach will be now further generalized towards the development of low-RCS antenna array configurations suitable for automotive radar applications.

5.3 Principle of operation of the low-RCS antenna

The basic idea of the low-RCS surface presented above is the mutual phase compensation between the AMC and the PEC. In principle, it should be possible to generalize such approach towards the development of low-RCS antenna arrays, for example by substituting the PEC with an arbitrary planar antenna. If the phase of the backscattering from the antenna is known, then it could be possible to compensate it by designing a proper AMC so that a destructive interference in the wave reflected back can be achieved. Similarly to the low-RCS surface, the low-RCS array would show a strong reduction in the amount of power reflected back in a specific angular direction and at a given frequency, while redirecting the impinging wave towards other directions.

This work deals with the reduction of the RCS in the same operating bandwidth where the antenna and the radar system are designed to function. Reducing the RCS at out-of-band frequencies is outside the purpose of this work,

since it is not relevant for the application of interest. However, it is in principle possible to achieve it with the very same design procedure presented in this section.

The here presented design strategy would offer an appealing advantage. To realize a low-RCS planar antenna array it is possible to keep the original design of the array — for example already developed for automotive radar applications — and then it would be sufficient to place the AMC on the same substrate around the array to develop its low-RCS counterpart. Designing such a low-RCS antenna would not bring a significant increase in the cost or in the fabrication complexity, since it can be realized with the same kind of technology already used for the typical development of the antenna system, that is to say, standard PCB photo-etching process. What is required for the design of the low-RCS array is the backscattering from the antenna, in terms of amplitude and phase. Once this value has been obtained, either by simulations or measurements, the development of the low-RCS version is straightforward.

As it can be easily understood, the design shown in this thesis is easy to develop and to integrate with the sensor components, compared to other low-RCS antenna design already presented in the literature. For example, in [100] the authors propose to replace the metallic ground plane of a microstrip array with a periodic hybrid PEC-FSS structure. A modification of the ground plane can be however tricky for integrating the array with the feeding network and the other electronic components, and the design strategy proposed in [100] provides anyway a strong RCS reduction only at frequencies outside the operating bandwidth of the antenna array.

In the previous section equation (5.2.1) described the RCS reduction of the investigated metasurface. To calculate in the most general case the antenna RCS reduction for the proposed design procedure, the equation can be modified as follows:

$$|r| = 10 \log \left| w_{\mathrm{AMC}} A_{\mathrm{AMC}} \mathrm{e}^{\mathrm{j}\varphi_{\mathrm{AMC}}} + w_{\mathrm{ant}} A_{\mathrm{ant}} \mathrm{e}^{\mathrm{j}\varphi_{\mathrm{ant}}} \right|^2 \mathrm{dB}\,, \tag{5.3.1}$$

where A_{AMC} and A_{ant} are the amplitudes and φ_{AMC} and φ_{ant} the phases of the reflection coefficients of the AMC and of the antenna, respectively. Compared to (5.2.1), the terms w_{AMC} and w_{ant} have been introduced. Unlike the amplitude of the PEC of (5.2.1), the amplitude A_{ant} can be different than A_{AMC} even in the ideal lossless case. Thus, to successfully achieve a small value for the reflection coefficient r, the weights w_{AMC} and w_{ant} must be introduced,

since forcing 180°-phase difference between the AMC and the antenna is not sufficient to maximize the RCS reduction. The two weights describe the area occupied on the PCB by the AMC and the antenna, respectively. By recalling the array theory approach of [96] to describe first (5.2.1) and thus also the generalized version of (5.3.1), the area occupation of the two building blocks, namely the antenna and the AMC, controls the scattered field and hence the RCS.

The first step for developing a low-RCS array, in particular a low-RCS microstrip array, is the estimation of the backscattering from the array to obtain the terms A_{ant} and φ_{ant} of (5.3.1). Obtaining them by means of full-wave simulations can be a tricky task, and thus the next section will treat the details of setting a proper simulation setup.

5.3.1 Simulation setup

In this work the backscattering from the array has been evaluated by means of 3D-full-wave simulations with an electromagnetic-field solver software. One of the typical antenna models that has been analyzed is a series-fed patch array as depicted in Fig. 5.13.

If the antenna array is illuminated by an incident plane wave, it is possible to define a reference plane at the antenna position, and in particular at the patch top metalization, and to calculate finally the amplitude and the phase of the reflection coefficient, i.e., of the backscattering. For example, in Fig. 5.13 the reference plane has been described by the white dashed lines.

A standard way of defining a plane wave in full-wave simulations is to set PEC and PMC (perfect magnetic conductor) walls [101] or equivalently to set unit cell boundaries as boundary conditions. The excitation is then usually given by a waveguide port placed above the AUT where a perfectly matched layer (PML) is set. In the example of Fig. 5.13 the waveguide port has been represented by the grid patterned area at the top of the picture. The electromagnetic problem has been then solved with the help of a frequency domain solver.

Simulating the backscattering from a microstrip array poses specific challenges with respect to the simulation setup. As it can be observed in Fig. 5.13, the waveguide port defined above the array has the same dimensions as the array substrate and the ground plane. In a microstrip patch array, they normally extend for many wavelengths in width and length, and consequently, the waveguide port can have large dimensions with respect to the wavelength. For

this reason, a great number of higher order modes must be taken into account to correctly carry out the simulations. The presence of so many higher order modes can lead to simulation artifacts in the plot of the reflection coefficient seen by the waveguide port when those modes become able to propagate.

Finally, the significant dimensions of the structure and, at the same time, the fine geometrical features of the array set a quite large number of mesh cells to proper discretize the 3D-model. All these issues let the simulation time and the memory consumption increase.

In the simulation setup used in this work, unit cell boundary conditions have been employed, since in the simulation software this configuration allows a larger number of higher order modes to be correctly taken into account. However, the structure that has been investigated is by its nature not periodic. This means, that the coupling between adjacent unit cells must be carefully reduced to avoid simulation artifacts. As a final remark, the edges of the array do not contribute to the simulation results since an infinite extent of the structure is assumed.

In many automotive radar applications, larger arrays composed of many columns in parallel of series-fed arrays are employed to achieve a higher gain.

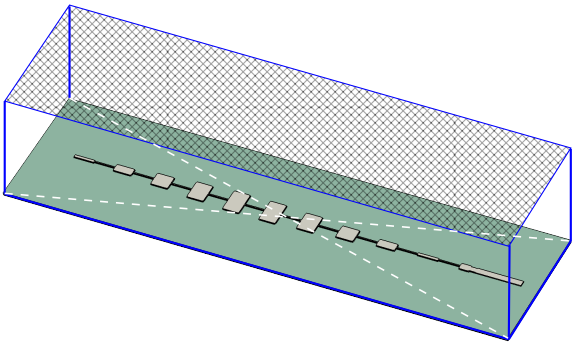

Fig. 5.13: Model of the series-fed microstrip array used in the 3D-full-wave simulation. The white dashed lines highlight the position of the reference plane for the calculation of the reflection coefficient, while the blue solid lines describe the bounding box. The area filled with the grid pattern represents the waveguide port to let a plane wave impinge on the array. Picture based on [43], © 2018 IEEE.

In those cases, the overall dimensions of the structure are obviously larger than in the example depicted in Fig. 5.13. Hence, solving such an electromagnetic problem can demand large computational resources. To overcome this issues, in the next chapter an alternative empirical design procedure for developing a more complex low-RCS antenna system will be proposed.

Another possible alternative simulation setup to threat the problem of analyzing the backscattering from a planar antenna array could be based on an asymptotic solver, that is often employed for calculating the RCS signature of objects extremely large in wavelengths. However, this approach was not covered in this thesis.

5.3.2 Limitations of the design procedure

The design of the low-RCS array relies on the knowledge of the array reflection phase to compensate it. It should be now clear from the previous section that accurately estimating the phase is sometimes not an easy tasks. Moreover, as it has been already mentioned previously, in all the cases where the backscattering of the array cannot be obtained by means of full-wave simulations, it can be only collected with the help of measurements. Phase measurements at mm-wave frequencies are extremely sensitive to small errors and inaccuracies, as it will be explained in the next chapter. For all these reasons, it is then interesting to understand how significant is a phase (or amplitude) error in (5.3.1) for the performance of the low-RCS array. By including two error terms ΔA and $\Delta\varphi$ to describe a discrepancy in the amplitude and the phase estimation, (5.3.1) becomes

$$|r| = 10\log\left|w_{\mathrm{AMC}}A_{\mathrm{AMC}}\mathrm{e}^{\mathrm{j}\varphi_{\mathrm{AMC}}} + w_{\mathrm{ant}}(A_{\mathrm{ant}}+\Delta A)\mathrm{e}^{\mathrm{j}(\varphi_{\mathrm{ant}}+\Delta\varphi)}\right|^2 \mathrm{dB}\,. \quad (5.3.2)$$

The phase compensation between the AMC and the array as in (5.3.1), and consequently in (5.3.2), can be elegantly described as a vector sum in the complex plane (or Argand-Gauss plane), as depicted in Fig. 5.14.

In the following it is assumed without loss of generality, that the array and the AMC occupy the same amount of area on the PCB and that the ideal lossless case is considered. In this basic example, the weights w_{AMC} and w_{ant} can be both assumed to be equal to 0.5, thus the magnitude of the vectors A_{AMC} and A_{ant} are also assumed identical. In the ideal case where a perfect mutual compensation between the AMC and the antenna exists, the error terms

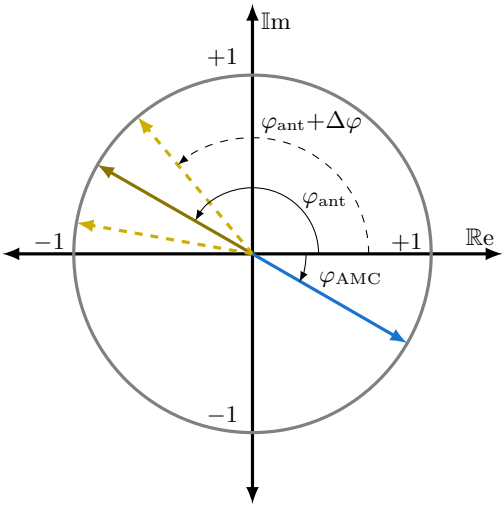

Fig. 5.14: Phase compensation between φ_{AMC} and φ_{ant} in (5.3.1), when $w_{\mathrm{AMC}}{=}w_{\mathrm{ant}}{=}0.5$, represented as vector sum in the complex plane. The amplitudes of the vectors are assumed equal, the losses are neglected. The effect of a non-ideal knowledge of φ_{ant} is described by the vectors with dashed lines and included in (5.3.2). Picture based on [43], © 2018 IEEE.

are equal to 0, and the RCS reduction can be calculated by the sum of the two vectors depicted with solid lines in Fig. 5.14.

If there is an error $\Delta\varphi$ in the estimation of the phase term, a perfect compensation between the antenna and the AMC cannot be obtained. This situation can be represented for example by one of the dashed vectors in Fig. 5.14. From easy calculations it can be concluded that, if the error on the phase of the antenna is within $[-20°, +20°]$ of the nominal value, it is still possible to achieve at least 9 dB RCS reduction. Similar considerations can be done for errors on the estimated amplitude from the antenna array. Uncertainties on the antenna amplitude up to 5 dB can still lead to at least 7 dB RCS reduction.

In all practical cases, there will be at the same time errors both on the amplitude and the phase of the reflection coefficient. This will deteriorate the achievable RCS reduction. However, small errors on the knowledge of the phase

or the amplitude can still be tolerated in the design procedure.

5.4 Conclusion

In this chapter the principle of operation of the proposed low-RCS antenna array has been introduced and described in detail.

The scattering properties of microstrip arrays make the design of the low-RCS counterpart intuitive and straightforward. Indeed, since the actual impedance matching at the array feed terminals does not significantly affect the total RCS of the array, the knowledge of the array structural mode is sufficient for the development of the low-RCS version.

The principle of operation of the low-RCS antenna is based on the low-RCS chessboard-like metasurface presented in [91]. A similar version designed for working in the E-band has been developed and characterized to test the feasibility — in terms of both fabrication and measurement accuracy — of such an approach at mm-wave frequencies.

The fundamental and new idea presented in this thesis is to retain the standard planar array design typically used in the mm-wave radar sensor and to reduce its RCS by placing a suitable AMC on the very same substrate. The mutual phase compensation in the backscattering from the AMC and the array is the basic mechanism for reducing the RCS of the array itself in a specific angular direction and in a given frequency range.

In the following chapter, the design of a low-RCS microstrip array will be further explained and a fabricated prototype tested. Afterward, more complex designs suitable for the radar sensor integration will also be introduced, to finally demonstrate that the use of low-RCS antenna systems can effectively mitigate the problem of multiple reflections between the sensor and the bumper.

Before moving to the next chapter, it is worth mentioning a last remark. The experimental characterization of the low-RCS chessboard-like metasurface proved that it is possible to achieve a good RCS reduction — compared to an equal-sized metal plate — in a sufficiently large frequency range for the application of interest. Similar results can also be predicted for the low-RCS microstrip antenna array. However, it is in principle possible to widen this frequency band by considering for example the use of multiband AMCs, such as the models presented in [102]. Although possible from a theoretical point of view, employing more complex AMC designs might typically require extremely small slot and trace widths of the unit cell, that can be quite challenging

to realize with a standard PCB fabrication process. On the other hand, the approach proposed in [95,103] seems more feasible, where two different unit cells with a slight difference reflection phase are employed. This simple technique can actually lead to a broadening of the frequency range where a good RCS reduction can be achieved. However, this method have not been tested yet as part of this work, but it could in principle conduct to promising results.

6 Millimeter-wave low-RCS antenna array design and sensor integration

In this chapter different microstrip antennas with low-RCS are presented. To verify their scattering properties, a dedicated measurement setup has been used. For this reason, the realized setup is discussed in detail at the beginning of this chapter.

Furthermore, an antenna array with low-RCS is integrated in a mm-wave MIMO radar sensor and tested behind a car bumper to demonstrate that the proposed approach can improve the radar-vehicle integration in a realistic scenario.

6.1 Measurement setup for the characterization of low-RCS antennas

This section presents and describes the two measurement setups that have been employed for the characterization of the low-RCS antenna prototypes. The first one has been used for measuring the backscattering from planar antenna systems and the RCS reduction in the normal and oblique incidence case, while the second one permits to characterize the multiple reflections between the AUT and a bumper sample.

6.1.1 Measuring the RCS reduction for normal and oblique incidence

Firstly, the setup for measuring the antenna backscattering properties and the RCS reduction in the normal incidence case is presented, and it is shown in Fig. 6.1. As it can be noticed, it is a monostatic measurement setup where a 25-dBi standard-gain horn antenna illuminates the AUT. The horn antenna is in turn connected through a rectangular waveguide to a frequency converter module that extends the measurement range of the VNA to the E-band. The available VNA does not support frequencies higher than 50 GHz, and therefore external frequency converter modules are required.

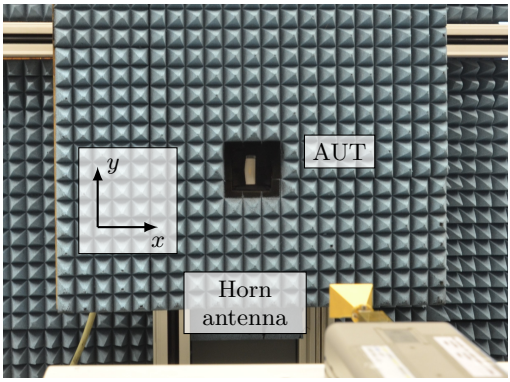

Fig. 6.1: Photo of the measurement setup for the characterization of the backscattering from the antenna in the normal incidence case. Picture from [104], © 2018 IEEE.

The AUT has been fixed to a plastic support, which is in turn controlled by a stepped motor to accurately set the position in x- and y-direction, according to the reference system of Fig. 6.1. Because of the short wavelength, the measurement results are quite sensitive to small misalignments. Therefore, to mitigate them, a set of 25 measurements has been collected on a rectangular planar scanning area. The final results are then calculated as average of the 25 different contributions. The distance between two adjacent points in the scanning domain can be adjusted depending on the AUT dimensions. Finally, the whole supporting structure is covered by absorbing material, as it can also be observed in Fig. 6.1.

In the measurements presented in this work, a one-port calibration has been used, which defines the reference plane on the waveguide at the input of the horn antenna.

To collect only the signal of interest, that is to say, the backscattering from the AUT, the time gating has been applied. This is a well-known feature implemented in most VNAs to selectively remove unwanted discontinuities in reflection or transmission measurements [105]. Starting from the time domain representation of the s_{11} measured by the horn antenna, obtained by means of an inverse discrete Fourier transform (IDFT), the gating can be used to filter out a part of the signal response in time, or equivalently in space. Afterward,

the remaining signal can be transformed back to the frequency domain with a DFT. In particular, in this work the gating function is a bandpass filter, used to isolate the amount of power reflected back by the AUT. The windowing suppresses the discontinuities at the input and at the ouput of the horn antenna and other unwanted spurious reflections from the surrounding environment.

The frequency range in which the measurements are carried out sets the response resolution of the time gating, which is in the end the spatial resolution required to resolve two closely spaced discontinuities. In this work all the measurements have been carried out in the whole E-band. Thus, the 30 GHz frequency range together with the bandpass windowing guarantees 9.7 mm response resolution, which is sufficient to correctly identify the backscattering from the AUT.

Depending on the AUT dimensions, the distance between the AUT and the horn antenna can be adjusted to eventually fulfill the farfield condition.

Typically, for both the characterization of the backscattering of an antenna and the evaluation of the RCS reduction, an additional reference measurement is required. The actual measurement data of the AUT is then divided by the reference measurement result. In this work the reference object can be either a metal plate with the same dimensions of the AUT or the standard antenna system without the integration of the AMC. However, for phase measurements the reference object should have known phase properties. For this reason a metal plate has been used. To compensate for the phase shift introduced by the metal plate itself, 180° should be added to measured phase data. This approach has been described in detail in [106]. It is important to underline that the AUT and the reference metal plate should be successively placed in the same position to correctly evaluate the reflection phase. Errors in the positioning can introduce additional phase shifts to the measured data, which can become not negligible at mm-wave frequencies.

Finally, for the oblique incidence case, a quite similar measurement setup can be employed. The AUT can be placed on a turntable in an anechoic chamber for performing a sweep on the azimuth plane while collecting the measurements with the same kind of monostatic setup described above. The same considerations about the calibration and the time gating still hold true.

6.1.2 Testing the AUT behind a bumper sample

By slightly modifying the measurement setup used for the normal incidence case, the AUT can also be tested in a more realistic scenario, i.e., behind a car bumper sample. More specifically, with such a setup the multiple reflections between the AUT and the bumper can be evaluated.

Figure 6.2 shows the setup, in which a silver-metallic bumper sample is between the AUT and the horn antenna. In this case, the AUT has been kept in a fixed position and no scanning in the xy-plane has been carried out.

The bumper sample used in this work has a thickness of 2.8 mm and an area of 18 cm × 24 cm. The distance between the sample and the AUT has been kept constant to 13 cm throughout the measurements. This is the smallest distance that can be achieved with the proposed measurement setup, and it is simply limited by the height of the pyramidal absorbers that surround the AUT, as it can be noticed in Fig. 6.2. The distance between the horn antenna and the AUT depends again on the AUT dimensions. To increase the power of the measured received signal, the distance has been sometimes reduced even below the farfield condition. This is however not critical, since the purpose of these measurements is simply a qualitative verification of the reduction of the multiple reflections compared to a standard antenna system without the integration of the AMC.

For easily investigating the multiple reflections, it is convenient to represent

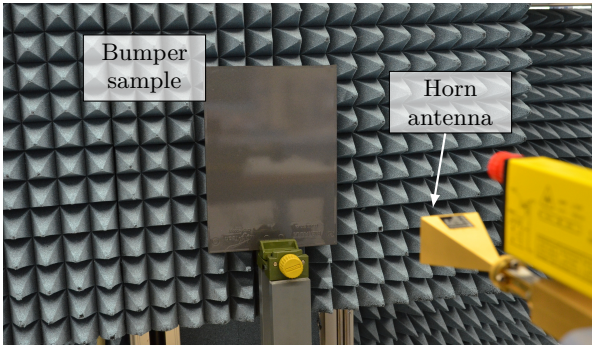

Fig. 6.2: Photo of the measurement setup for analyzing the multiple reflections between the AUT and a sample of a car bumper [104], © 2018 IEEE.

the measured signal in the time domain. Indeed, in this way it is possible to quickly and intuitively locate in space the multiple reflections and to immediately compare their amplitudes, when antenna systems with and without the integration of the AMC are employed. In the time domain representation, the distance plotted on the abscissa refers to the distance from the reference plane set with the one-port calibration, that means the rectangular waveguide at the input of the horn antenna.

The picture in Fig. 6.3 sketches the first multiple reflection that can be characterized with the setup described above.

The horn antenna illuminates the AUT. The wave traveling from the horn antenna impinges first on the bumper sample and then on the AUT. Part of the wave is reflected back by the AUT towards the bumper, which in turn reflects also back a part of the impinging wave towards the AUT. Finally, the signal is received by the horn antenna after bouncing once again against the AUT. This path has been measured for some fabricated prototypes with and without the use of the AMC. The comparison of these measurement results gives a clear insight into the amplitude reduction of the first multiple reflection.

Finally, it is worth mentioning that the measurement setup described in this work seems to be the only effective solution for the experimental characterization of the multiple reflections related to the radar-vehicle integration. Indeed, it is not possible to directly measure them with the AUT or the radar sensor because of the limited bandwidth of the microstrip arrays typically employed.

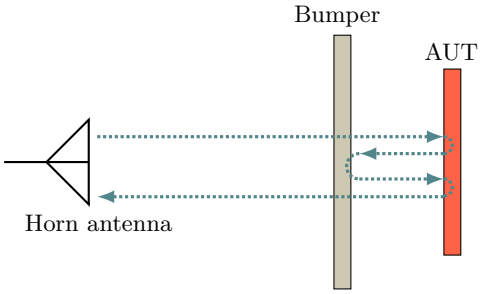

Fig. 6.3: Sketch of the path (dotted lines) of the first multiple reflection that can be measured with the experimental setup of Fig. 6.2. Picture from [43], ©2018 IEEE.

The resulting poor spatial resolution cannot lead to satisfactory results. The change of perspective given by the measurement with the horn antenna of Fig. 6.2 brings the required bandwidth and thus enough spatial resolution.

6.2 Development of a microstrip low-RCS array

Using the simulation setup described in Section 5.3.1, a microstrip patch array with low-RCS properties has been designed and developed. The starting point of the design was the analysis of the backscattering of the 10-element series-fed patch array presented in Fig. 5.3. The very same model has been then retained for the development of the low-RCS counterpart. In the simulation setup, the metalization of the array has been defined as PEC and the substrate RO3003 modeled as lossless to speed up the simulation time.

The backscattering from the microstrip array, i.e., the reflection coefficient obtained by means of full-wave simulations, is depicted in Fig. 6.4a. As it can be observed, the amplitude A_{ant} of the reflection coefficient is slightly below 0 dB close to the resonance frequency of 77 GHz, while the phase φ_{ant} is confined between 141° and 151° in the frequency range of interest. The small ripples visible in Fig. 6.4a can be ascribed to simulation artifacts due to the excitation

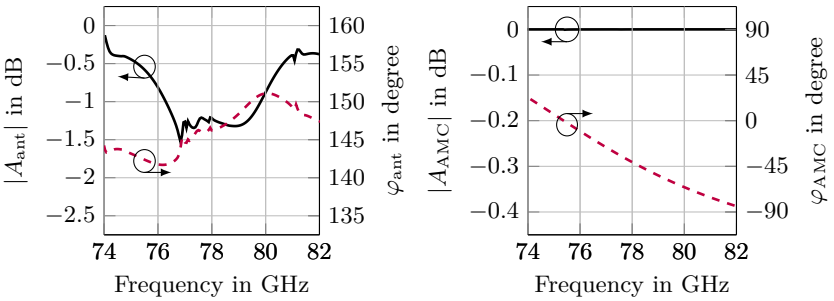

(a) Patch array. **(b)** AMC.

Fig. 6.4: Backscattering calculated with full-wave simulations of the microstrip patch array (left) and of the AMC (right) illuminated by an incident plane wave. Amplitude and phase of the reflection coefficients are depicted in the plots with solid and dashed lines, respectively. Pictures from [43], © 2018 IEEE.

of higher order modes.

The next step is the design of a suitable squared patch to be used as AMC in order to compensate the reflection phase of the array at 77 GHz. In particular, by using a squared patch with a side length of 0.88 mm and a gap between adjacent cell equal to 0.13 mm it is possible the get the results of Fig. 6.4b. It can be noticed that at 77 GHz the reflection phase is $-33°$. This value is close to the ideal required value for a perfect phase compensation of the antenna array contribution.

Once the backscattering from the antenna and from the AMC have been investigated, the weights needed in (5.3.1) can be finally defined. The photo of the fabricated prototype, where the AMC has been integrated on the same substrate as the antenna array, can be seen in Fig. 6.5. In this example, the weight w_{AMC} is equal to 0.56. The outer part of the prototype has been covered by absorber material during the experimental characterization. Also in this case, a waveguide-to-microstrip transition has been used to allow further measurements.

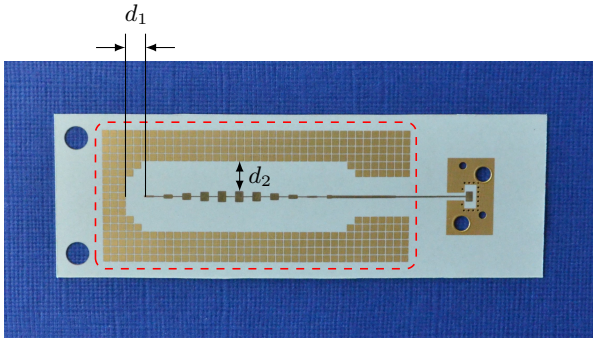

Fig. 6.5: Photo of the prototype of the low-RCS antenna array. The red-dashed area describes the part of the array illuminated by the horn antenna during the measurement, while the remaining part has been covered by absorbers. The AMC occupies 56% of this area. The distances d_1 and d_2 are equal to 2.42 mm and 3.94 mm, respectively. Picture based on [43], © 2018 IEEE.

6.2.1 Measurement results of the low-RCS microstrip array

The integration of the AMC around the microstrip patch array should not degrade the antenna performance. To this purpose, before starting the evaluation of the RCS reduction, two prototypes with and without the integration of the AMC have been tested and their performances compared.

First of all, Fig. 6.6 shows the input reflection coefficient of the two arrays measured from the waveguide-to-microstrip transition. As it can be observed from the comparison of the measurement results, the integration of the AMC does not significantly affect the amplitude of the s_{11} except for a slight shift towards higher frequencies. This effect could be however also ascribed to the discrepancies in the fabrication tolerances, since the two prototypes have been not developed during the very same etching process. Afterward, the radiation pattern in the two main cuts has been measured in an anechoic chamber. As an example, Fig. 6.7 presents the results at 77 GHz. The sidelobe level and the 3-dB beamwidth of the low-RCS antenna are similar to that one of the standard series-fed patch array, i.e., without the integration of the AMC. Similar results have been obtained at the other frequency points, and they are here omitted for the sake of brevity. They can be found however in the Appendix B on page 129.

From the previous experimental results it can be concluded that the integration of the AMC does not critically affect the antenna array performance. The co-design of the microstrip array together with the AMC placement to assure

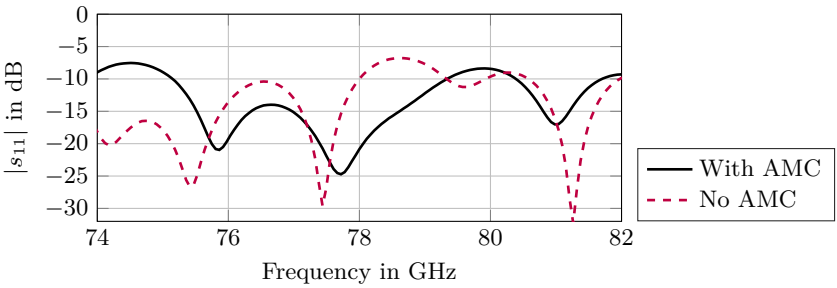

Fig. 6.6: Measured input reflection coefficient of the arrays fed by the waveguide-to-microstrip transition, with and without the integration of AMC. Results from [43], © 2018 IEEE.

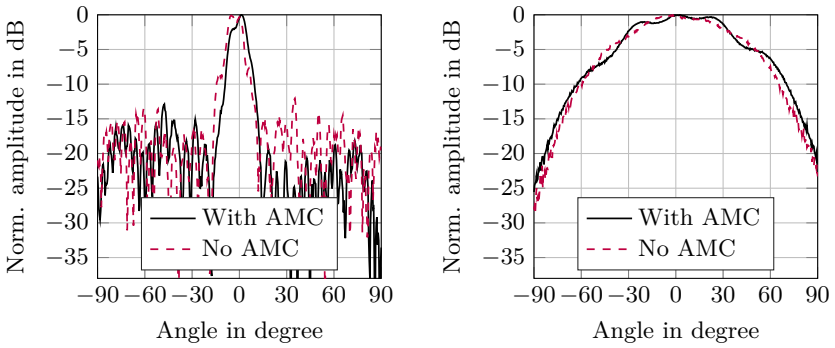

(a) E-plane. **(b)** H-plane.

Fig. 6.7: Measured radiation pattern at 77 GHz with and without the integration of the AMC around the series-fed patch array. Results from [43], ©2018 IEEE.

a good antenna performance is hence not necessary.

The following step is the characterization of the RCS reduction using the monostatic measurement setup described at the beginning of this chapter and depicted in Fig. 6.1. In this case, a reference metal plate with the same dimensions as the AUT has also been measured.

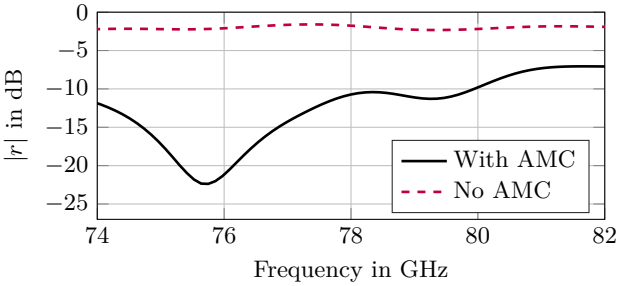

Fig. 6.8: Measured backscattering from the array with and without AMC for the normal incidence case. Both curves are normalized to a measured equal-sized metal plate. Results from [43], ©2018 IEEE.

The measurement results for the normal incidence case can be seen in Fig. 6.8. It can be observed that the low-RCS array shows an amplitude of the backscattering approximately 20 dB smaller compared to the standard microstrip array without the use of the AMC at approximately 76 GHz. The RCS reduction is at least 10 dB in a 6-GHz range.

The AUT has been then tested behind the car bumper sample with the setup of Fig. 6.2. Also in this case, the result has been compared to a patch array without the integration of the AMC. The measurement results represented in the time domain are depicted in Fig. 6.9. First of all, in the plot the reflections from the horn antenna itself and from the bumper plate can be clearly observed. They are of course identical in the amplitude for both prototypes. After them, the peak that corresponds to the backscattering from the AUT is distinctly present at approximately 0.36 m. The results here presented confirm again the results of Fig. 6.8, namely the reduction of the backscattering when the low-RCS antenna array is employed. Consequently, the amplitude of the multiple reflections can be reduced, too. The first multiple reflection at a distance of approximately 0.48 m can be identified. With the use of the low-RCS array, its amplitude decreases compared to the normal patch array.

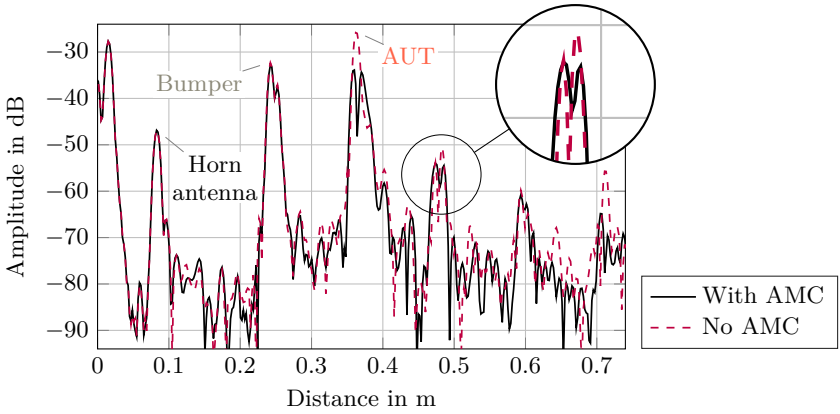

Fig. 6.9: Testing the low-RCS antenna array behind a sample of a car bumper. Representation of the measured backscattering in the time domain. The zoomed view highlights the amplitude reduction in the first multiple reflection (see the sketch of Fig. 6.3). Results from [43], ©2018 IEEE.

6.2.2 Increasing the area occupied by the AMC

Finally, to further understand the principle of operation of the low-RCS antenna, the effect of changing the area occupied by the AMC on the achievable RCS reduction has been analyzed. To this purpose, a second prototype has been realized, which is shown in Fig. 6.10.

The AMC occupies now a larger area on the substrate compared to the model of Fig. 6.5, where it covered 56% of the PCB surface. In particular, the AMC fills now 76% of the area illuminated by the horn antenna during the measurements.

The measurement results depicted in Fig. 6.11 demonstrates that the increased AMC area does not improve the RCS reduction, rather it causes an over-compensation of the backscattering from the antenna array and, hence, the RCS reduction is smaller than in the previous case.

These experimental results implicitly confirm the correctness of (5.3.1), where two weights have been introduced to describe the amount of backscattering related to the relative area occupation on the PCB of the antenna array and

AMC, respectively. The relative area occupation of the AMC plays a major role in controlling the RCS reduction.

6.3 Design of a complex low-RCS antenna system

The design of the low-RCS microstrip array of Fig. 6.5 is based on the knowledge of the backscattering from the the series-fed patch array, in terms of amplitude and phase. These values have been obtained by means of full-wave simulations. However, the limitations of the simulation setup, which have been described in Section 5.3.1, pose quite strict constraints on the maximum size of the AUT.

In many practical cases, the radar sensors make use of larger antenna arrays to increase the realized gain. Typically, multiple columns of series-fed arrays are used. The backscattering from such structures cannot be analyzed with the simulation setup described in the previous chapter. Another example, where the full-wave simulation setup fails to correctly analyze the structure of interest, is a MIMO-radar antenna configuration. In this case, multiple antenna arrays are employed as transmitting and receiving elements, and they all contribute at the same time to the RCS signature of the antenna system.

This section will thus deal with the design of a more complex low-RCS antenna system, that cannot be developed with the aid of full-wave simulation results to obtain the backscattering. The starting point is the MIMO antenna system of Fig. 6.12. As it can be seen in the picture, some large microstrip arrays made out of multiple series-fed patch array columns can be observed on

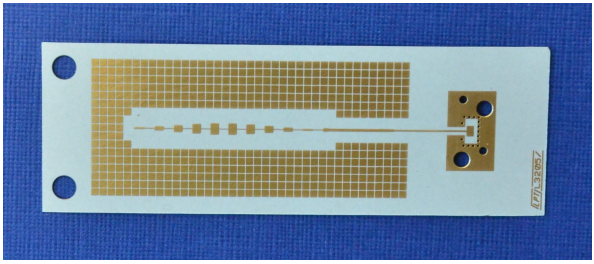

Fig. 6.10: Prototype of the low-RCS array with 76% of the area illuminated during the measurement occupied by the AMC. Picture from [43], ©2018 IEEE.

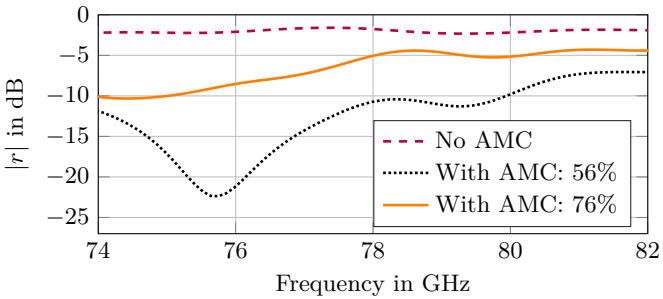

Fig. 6.11: Comparison of the measured backscattering from the array without AMC and the arrays of Figs. 6.5 and 6.10 for normal incident direction. The curves are normalized to a measured equal-sized metal plate. Results from [43], © 2018 IEEE.

the substrate.

6.3.1 Overview and design procedure

To overcome the limitations of the simulation setup, an *empirical* design approach has been used, as presented in [104]. The main design steps will be here presented, and the measurement results of a fabricated prototype will be described in the following section.

Since the design procedure cannot rely on the simulation results, the terms A_{ant} and φ_{ant} of (5.3.1) have been obtained by means of measurements, with the same setup described at the beginning of this chapter.

The measured backscattering of the model in Fig. 6.12 is depicted in Fig. 6.13a in terms of both amplitude and phase. Once these values are known, the proper dimensions of the AMC can be calculated with full-wave simulations in order to compensate the phase term φ_{ant}, and finally, by changing the weights w_{AMC} and w_{ant}, the RCS reduction can be further adjusted. The simulation results that give φ_{AMC} are shown in Fig. 6.13b. These results have been obtained for a square patch with an edge length of 0.87 mm and with a gap between adjacent patches of 0.13 mm. As it can be noticed from the amplitude A_{AMC}, the losses have been neglected.

A picture of the fabricated prototype can be seen in Fig. 6.14. A set of squared patches acting as AMC surrounds the MIMO antenna system presented

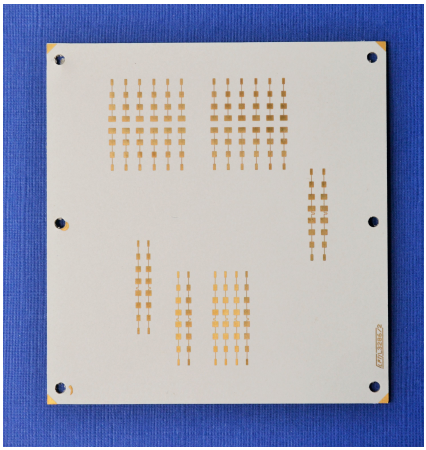

Fig. 6.12: MIMO antenna system composed of multiple series-fed microstrip arrays. The external dimensions of the PCB are 63 mm × 67 mm.

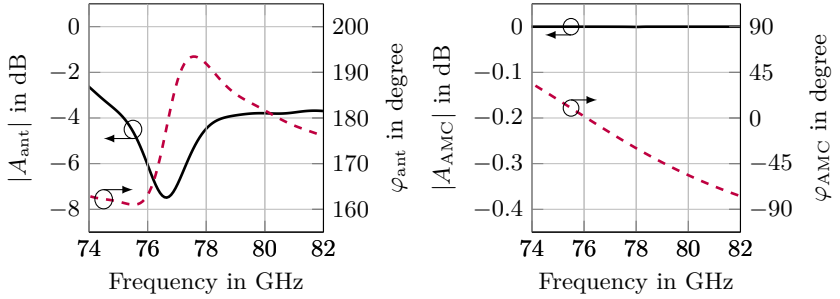

(a) MIMO array. **(b)** AMC.

Fig. 6.13: Measured backscattering of the MIMO antenna configuration (left) and backscattering of the AMC obtained by full-wave simulations (right). Amplitude and phase of the reflection coefficients are depicted in the plots with solid and dashed lines, respectively.

above. For this model, the weight w_{AMC} has been set to 0.4 and w_{ant} to 0.6.

Since it has been already verified that only the structural mode contributes

to the antenna RCS, the feeding network has been omitted, as it can be clearly observed in both Fig. 6.12 and Fig. 6.14.

Before moving to the experimental results, it must be noticed that the proposed empirical method does not provide any rigorous solution to the problem of designing a complex low-RCS antenna system. In particular, the main limitation of this approach is related to the use of phase measurements to get φ_{ant} required in (5.3.1). As mentioned in Sec. 6.1, it is well known that at mm-wave frequencies the accuracy of phase measurements is critical. However, as the next results will show, this approach is still a valuable support where no analytical or numerical solutions are available, and it is still possible to calculate a reasonably good prediction of the achievable RCS reduction.

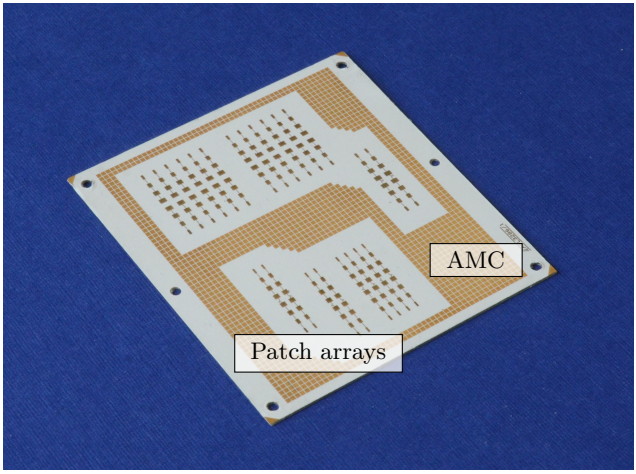

Fig. 6.14: Fabricated low-RCS MIMO antenna system. The external dimensions of the PCB are the same as the model of Fig. 6.12, namely 63 mm × 67 mm.

6.3.2 Measurement results of the low-RCS MIMO antenna configuration

Figure 6.15 presents the measured RCS reduction for the normal incidence case. The experimental results have been compared to the estimated RCS reduction calculated with (5.3.1), where the backscattering from the antenna has been obtained by the measurements of Fig.6.13a. As it can be noticed, at 77 GHz the reduction of the RCS is equal to 17 dB. Although without a perfect match, the two curves are in fairly good agreement. The highest RCS reduction in the measurement result (solid line) is only shifted by 0.53 GHz towards higher frequencies compared to the estimated results of (5.3.1).

Afterward, the measurements for the oblique incidence case have been carried out in an anechoic chamber. The results can be seen in Fig. 6.16 for 77 GHz and 79 GHz. At both frequencies, the measurements confirm again the good RCS reduction for normal incidence (angle of 0°). At 77 GHz the structure with the AMC shows a smaller backscattering compared to the counterpart without the AMC in the angular range $[-10°, +10°]$. Outside this range the amplitude becomes comparable or even larger than in the case without AMC. This behavior is similar to the results of the chessboard-like metasurface (see Fig. 5.12). Thus, due to the displacement of the AMC around the antennas, the impinging wave is redirected towards directions other than the boresight. A similar behavior can also be observed at 79 GHz.

Finally, the MIMO low-RCS antenna configuration has also been tested be-

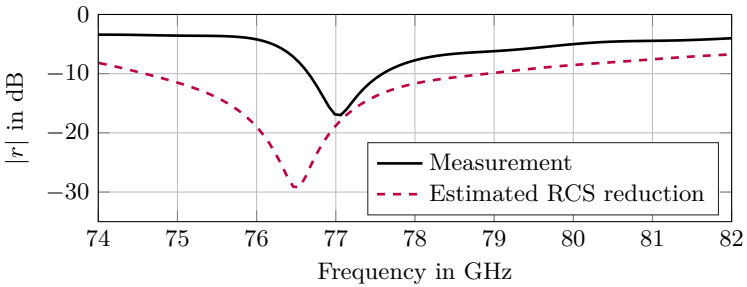

Fig. 6.15: Estimated — using (5.3.1) — and measured RCS reduction for the prototype of Fig. 6.14. The solid curve has been normalized to a prototype without the integration of the AMC. Results from [104], © 2018 IEEE.

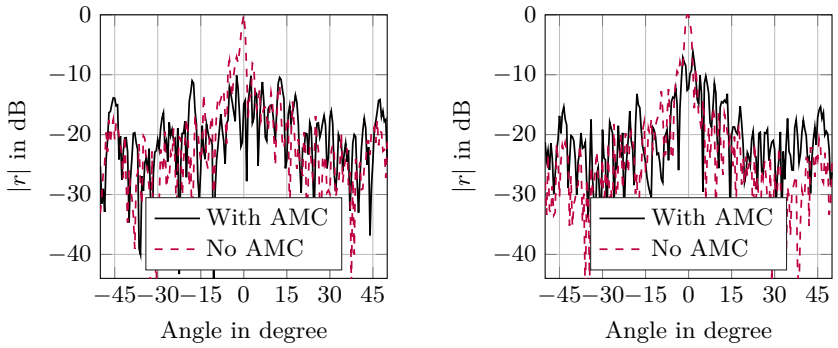

(a) 77 GHz. **(b)** 79 GHz.

Fig. 6.16: Measured backscattering from the two prototypes with and without AMC on the azimuth plane. The results have been normalized to the measurement results of a reference metal plate. Results from [104], © 2018 IEEE.

hind the car bumper sample for the characterization of the multiple reflections, and the results are depicted in Fig. 6.17. Similarly to the time domain results of the single column low-RCS array of Fig. 6.9, also in this case it is possible to clearly identify in the plot the reflections from the horn antenna, from the bumper, and from the AUT. In particular, as expected, the measured amplitude of the reflections from the horn antenna and the bumper are not affected by the specific AUT. Again, also here the reduction in the backscattering from the AUT — visible at approximately 0.74 m — when the AMC is placed on the substrate confirms the good RCS reduction for the normal incidence case of Fig. 6.15. Finally, the first multiple reflection between the AUT and the bumper sample at the position of 0.85 m can be distinctly observed in the plot, too. By looking at the measurement results, it is possible to conclude that the low-RCS prototype allows to clearly reduce the amplitude of the first multiple reflection.

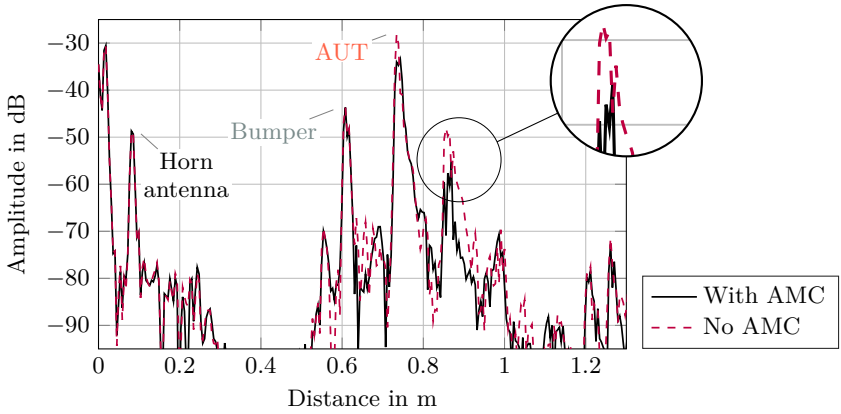

Fig. 6.17: Testing the MIMO low-RCS antenna configuration behind a sample of a car bumper. Representation of the measured backscattering in the time domain. The zoomed view highlights the amplitude reduction in the first multiple reflection (see the sketch of Fig. 6.3). Results from [104], © 2018 IEEE.

6.4 Integration in a millimeter-wave radar sensor

After verifying the design of the low-RCS arrays, it is also interesting to integrate them into a mm-wave radar sensor. This makes possible to further understand if the use of a low-RCS antenna configuration can actually lead to a reduction in the angular errors for DoA-estimation problems when the radar is placed behind the car fascia.

6.4.1 Low-RCS antenna system design

The radar used to test the proposed design strategy is a fast-FMCW MIMO system with M_t=3 transmitting and M_r=4 receiving elements. The bandwidth of the radar is 500 MHz centered around 76.5 GHz. The same kind of antenna array is used for both the transmitters and receivers, and it is composed of two slotted patches in parallel, as it can be noticed from Fig. 6.18. To avoid any beam splitting, the patches are fed with 180°-phase difference thanks to the different lengths of the microstrip feeding lines. The prototype has been realized with standard PCB-technology on a Teflon-based substrate with a thickness

of 127 µm and a nominal value of the relative permittivity of 3. Similarly to the previous prototypes, the AMC has been displaced around the antenna elements, as it can also be observed from Fig. 6.18. The side length of the squared patch used as AMC unit cell is 0.87 mm, and the gap between adjacent patches is 0.15 mm.

Due to the complexity of the MIMO configuration, also in this case it was not possible to perform a full-wave simulation of the complete antenna system. Like in the previous example, an empirical design approach has been followed. However, while in the previous section the terms A_{ant} and φ_{ant} of (5.3.1) were estimated with measurements, in this example the starting point for the design is the simulation of the 2-element slotted-patch array. It is then assumed that the reflection coefficient of the whole MIMO antenna system is similar to the one of the 2-element array. This is not an exact solution to the problem of designing a low-RCS MIMO antenna configuration. But again, it is an helpful empirical approach when alternative solutions cannot be exploited.

Figure 6.19a presents the backscattering from the 2-element slotted patch array calculated by the full-wave simulator. As it can be observed then from Fig. 6.19b, the reflection phase of the AMC is 180° out of phase with respect to the one of the array around 78 GHz, in order to achieve the phase compensation. To take into account the different amplitudes A_{ant} and A_{AMC}, that would not allow a perfect destructive interference, the weights w_{ant} and w_{AMC} must be carefully chosen to make $|r|$ in (5.3.1) small. In this case the AMC occupies 43% of the area, and an almost perfect mutual cancellation can be achieved close to the frequency of 78 GHz, as it can be seen from the estimated RCS reduction in Fig. 6.20.

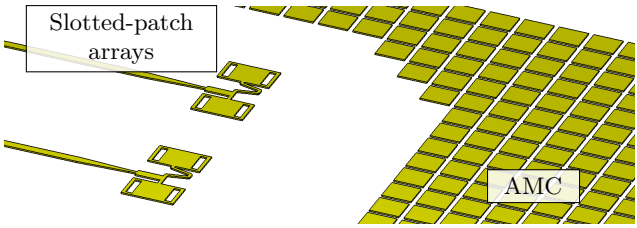

Fig. 6.18: Sketch of the low-RCS antenna configuration. The AMC surrounds the slotted patch arrays. Zoomed view of two transceivers. Picture from [107], © 2018 IEEE.

For the sake of completeness, the results of Fig. 6.19a can be compared with the reflection phase of the series-fed array depicted in Fig. 6.4a on page 96. As it can be clearly observed, the curve that represents the backscattering from the slotted patch array is significantly smoother. This difference can be explained by recalling the full-wave simulation setup employed in this work. Indeed, the dimensions of the waveguide port that illuminates the structure are directly related to the size of the array substrate and the ground plane. Consequently, the substrate size sets the number of higher order modes that must be taken into account during the simulation. The smaller size of the slotted patch array substrate reduces thus the number of modes included in the simulation, and makes the curve smoother thanks to the absence of simulation artifacts.

6.4.2 Radar measurement results

A prototype of the proposed MIMO radar equipped with the low-RCS antenna system has been fabricated and tested. For a fair evaluation of the impact of the low-RCS antenna system, a second prototype without the integration of the AMC has been realized, too. The MMIC placed on the PCB for the generation of the high-frequency signal has been covered with absorbing material to suppress the spurious radiation that can degrade the antenna radiation pattern.

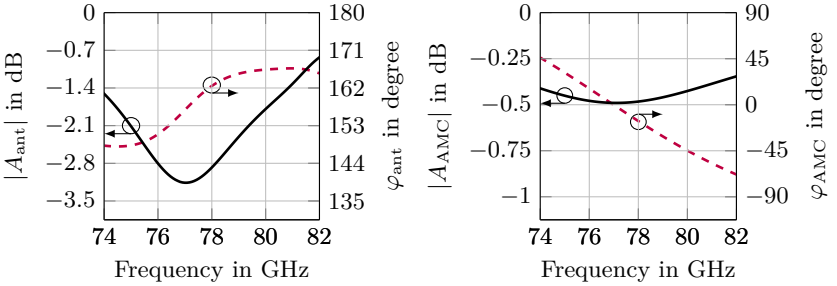

(a) Slotted patch array. **(b)** AMC.

Fig. 6.19: Backscattering calculated by means of full-wave simulations of the 2-element slotted patch array (left) and of the AMC (right). Amplitude and phase of the reflection coefficients are depicted in the plots with solid and dashed lines, respectively. Results from [107], ©2018 IEEE.

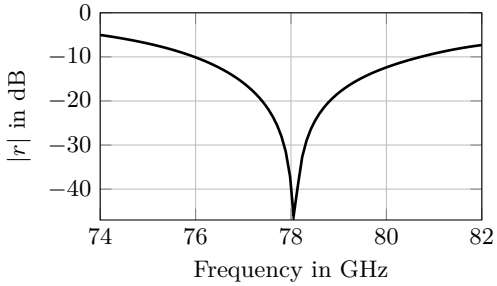

Fig. 6.20: Estimated RCS reduction using (5.3.1) with the simulation results of Fig. 6.19. Picture from [107], © 2018 IEEE.

Finally, both prototypes — with and without AMC — have been covered with a radome typically employed in mm-wave automotive radars.

First of all, it is important to verify that the AMC does not affect the antenna array radiation pattern, similarly to what has also been checked in Section 6.2.1. Since a direct measurement of the single patch array is not possible, the 2-way radiation pattern for all the transmitter-receiver pairs has been collected: a corner reflector has been placed in the farfield of the sensor, and a sweep on the azimuth plane has been performed. The results for one transmitter-receiver pair are depicted in Fig. 6.21. As it can be observed, the presence of the AMC does not affect much the shape of the radiation pattern. The 2-way radiation pattern remains the same with and without the integration of the AMC. Similar results have been obtained for the other channels, too.

The next step is the characterization of the angular error in the DoA estimation when the radar sensor is placed behind a car bumper. To calculate the angular error, first of all the DoA estimation problem must be solved. Then, by comparing the estimated angle ϑ_{est} with the actual DoA, the angular error is easy to determine.

In this specific problem, the DoA estimation can be practically solved by measuring the cross-correlation between the measured signal when the bumper is in front of the radar and a reference measurement taken without the bumper. If the correlation returns 1, it means that the two measurements are identical, i.e., the impact of the bumper is negligible, and the estimated DoA coincides with the actual DoA. In such a way, it is possible to characterize the similarity

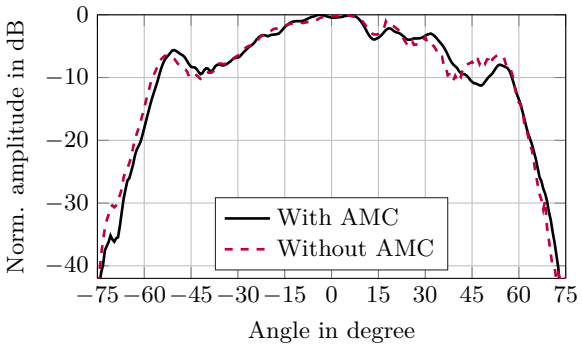

Fig. 6.21: Measured 2-way radiation pattern using the first transmitter and the first receiver, for both the sensors with and without AMC. Picture from [107], ©2018 IEEE.

between the measured signals, and thus understand how the measurements collected with the bumper differ from the reference results. This kind of approach for solving the DoA problem is strictly related to the problem of the ambiguities in the beam pattern and the definition of the AF given in Chapter 2.

Such a solution for finding the DoA of a target is sometimes called *deterministic maximum likelihood* (DML) method [108]. However, for the single snapshot and single target scenario, finding the DML estimator means simply maximizing the Bartlett's beamformer (or conventional beamformer) spectrum [109]. Indeed, similarly to the conventional beamformer the cross-correlation can be calculated over a range of angles ψ. The direction that maximizes the computed cross-correlation gives the estimated DoA. Typically, in the Bartlett's beamformer a weight vector is also employed, which is taken in this case from the reference measurement data, and it can be described as a spatial filter matched to the received signal [49].

As a last remark, it should be mentioned that the DoA estimation problem can be solved in such an intuitive way because the reference (or calibration) measurement has been carried out at several known angular positions, and the array response is basically known at those points. No interpolation has been applied, and the DoA can be estimated only at the very same points of the azimuth sweep.

The bumper sample used in this measurement setup is made out of polycarbonate with a thickness of 2.89 mm. The measurement setup is quite similar to the one for the characterization of the 2-way radiation pattern. First of all, the reference measurement for both prototypes has been carried out without the presence of the bumper. It is identical to the procedure for collecting the two-way pattern. Afterward, the bumper sample has been placed in front of the radar sensor, and the 2-way pattern has been measured again while keeping the corner reflector in the same position. By comparing the results with and without the bumper, it is possible to assess the angular error and to verify the impact of the low-RCS antennas on it.

In Section 2.3 the problem of the radar-vehicle integration — and in particular the issue of the multiple reflections between sensor and bumper — has already been extensively described. However, it is important to recall here that, when placing the radar sensor behind the bumper, a standing wave can occur. For a correct examination of the experimental results, it is convenient to avoid that the bumper is located exactly at one of the maxima or minima of the standing wave pattern. Therefore, multiple measurements have been collected, where the distance between the sensor and the bumper has been changed in steps of 0.5 mm starting from the initial value of 10 mm. It must also be underlined that in a practical scenario, where the sensor is installed in a car, it is usually hard to exactly control the positioning behind the fascia, typically due to mechanical inaccuracies. Hence, collecting multiple measurements by slightly changing the distance between the prototype and the bumper sample is an effective solution to test at the same time the robustness of the results.

Let $\boldsymbol{C}$ be the matrix that contains the results of the reference measurement, as follows:

$$\boldsymbol{C} = \begin{array}{c} \begin{matrix} \psi_1 & \psi_2 & \dots & \psi_N \end{matrix} \\ \begin{pmatrix} c_{11} & c_{12} & \dots & c_{1N} \\ c_{21} & c_{22} & \dots & c_{2N} \\ \vdots & \vdots & \ddots & \vdots \\ c_{M1} & c_{M2} & \dots & c_{MN} \end{pmatrix} \end{array} \begin{array}{l} \text{channel 1} \\ \text{channel 2} \\ \vdots \\ \text{channel } M \end{array} \tag{6.4.1}$$

where $M{=}M_t M_r$ is the number of virtual channels and N is the number of sweep points in azimuth plane where the measurements have been collected.

The generic element c_{ij} is a complex value describing the reference measurement result at the angular position ψ_j for the i-th virtual channel[1]. In this specific case N is equal to 751. The measurements have been collected between $\pm 75^\circ$ with a spacing of 0.2° between two consecutive measurement points.

Every element of the matrix can be normalized by dividing it by the norm of the column vector as follows:

$$\widetilde{c}_{ij} = \frac{c_{ij}}{\left\|\boldsymbol{c}_j\right\|}\,, \tag{6.4.2}$$

and to define then the matrix $\widetilde{\boldsymbol{C}}$, which is composed of the elements $\widetilde{c}_{ij}$. In a similar manner, let $\widetilde{\boldsymbol{A}}$ and $\widetilde{\boldsymbol{A}}_{\mathrm{AMC}}$ be the matrices that contain the normalized measurement results of the sensor without and with the AMC, respectively, collected after the placement of the bumper in front of the radar. Thanks to the normalization, the cross-correlation can be written in a compact way as inner product:

$$\boldsymbol{X} = |\,\widetilde{\boldsymbol{C}}^H \cdot \widetilde{\boldsymbol{A}}|\,, \tag{6.4.3}$$

$$\boldsymbol{X}_{\mathrm{AMC}} = |\,\widetilde{\boldsymbol{C}}^H \cdot \widetilde{\boldsymbol{A}}_{\mathrm{AMC}}|\,, \tag{6.4.4}$$

where the symbol $(\cdot)^H$ denotes the conjugate transpose (Hermitian) matrix. Again, this calculation is similar to the computation of the ambiguity function (AF) in (2.2.4) on page 13. The two matrices in (6.4.3) and (6.4.4) are square matrices of order N, and they describe the cross-correlation between the two different sets of measurements. For estimating the DoA ψ_{est}, the maximum in every column $\boldsymbol{x}_l$, i.e., the highest similarity, must be searched. Thus, the DoA is given by

$$\psi_{\mathrm{est}} = \arg\max_{\psi} \boldsymbol{x}_l\,, \tag{6.4.5}$$

where the function arg max returns the angular positions where the cross-correlation reaches the maximum[2]. For every column $\boldsymbol{x}_l$ in the cross-correlation

[1] As explained in Section 2.2, this complex value has been generated by an FFT, and it is the starting point for further processing of the DoA estimation.

[2] For a given function, the arg max, i.e., the *argument of the maximum*, returns the points within the function domain at which the function reaches the maximum. The name *argmax* can be easily understood by recalling that for a function $f(x)$ the element x can be called not only variable, but also *argument* [110].

matrix it is finally possible to calculate the angular error as

$$\psi_{\text{err}} = \psi_l - \psi_{\text{est}} \,, \tag{6.4.6}$$

namely as a difference between the nominal angular position ψ_l and the estimated DoA ψ_{est}.

Figure 6.22 presents the angular error in the DoA estimation at all the possible offset positions for the two prototypes, namely with and without the use of the AMC. The plotted reference value is the autocorrelation of the ideal reference measurement taken without the bumper, and for this reason it is equal to 0° in the whole angular range. As it can be observed in Fig. 6.22b, the low-RCS antenna system clearly reduces the error in the DoA estimation in an angular range close to the boresight direction, that means close to 0°, approximately in the range $\left[-25°, 10°\right]$. The AMC displacement on the PCB is not symmetric, and thus neither is the pattern of the angular error reduction.

In Fig. 6.22a for some angular positions, such as at ψ=3.8° for the 1-mm offset measurement and at ψ=−7.2° for the 2-mm offset measurement, a large angular error can be observed. These results can be better explained by looking at the cross-correlation plots of Fig. 6.23 for these specific offsets and angular values. As it can be noticed, the large errors are generated by the wrong angle estimation for positions either close to the FoV boundaries (see Fig. 6.23a) or by ambiguities such as in Fig. 6.23b. While the former can be easily avoided by confining the DoA estimation in a slightly smaller FoV, the latter is a critical issue for the radar sensor, since it generates an ambiguity in DoA estimation in the really central part of the FoV, and it can potentially cause an unnecessary driving intervention. It can be clearly observed in Fig. 6.23b that in the cross-correlation plot two angular directions show the same amplitude, and it is hence not possible to estimate the correct DoA ψ_l. On the other hand, low-RCS antennas mitigate this problem to some extent. By looking at the cross-correlation plot of the prototype with the integration of the AMC for the very same offset and angular position, it can be noticed in Fig. 6.24 a reduction in the amplitude of the ambiguity. Although in absolute terms it does not represent a huge reduction in the sidelobe level of the spectrum, it is still enough to lead to a reasonable DoA estimation and thus to a smaller angular error as demonstrated by Fig. 6.22b.

Finally, using the angular error results, the standard deviation σ of the two sets of measurements has been calculated and plotted in Fig. 6.25. As it can

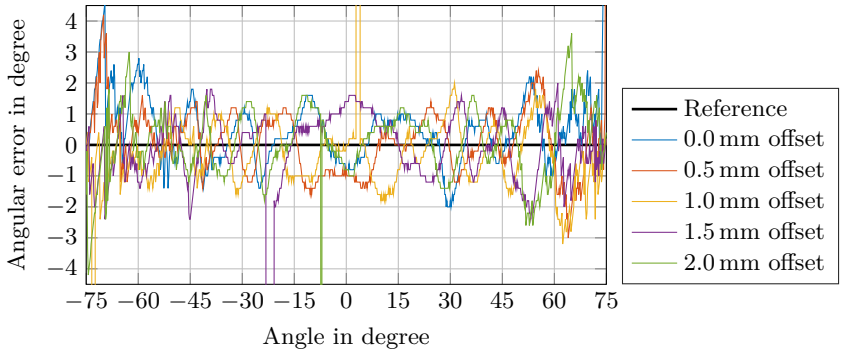

(a) Without AMC.

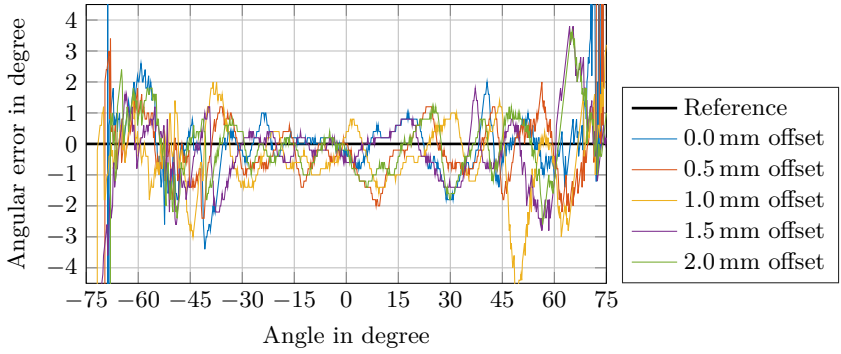

(b) With AMC.

Fig. 6.22: Angular error in the DoA estimation when the prototypes (with and without AMC) are placed behind the bumper. The distance between the sensors and the bumper has been changed in steps of 0.5 mm. Five different measurements have been collected. Results from [107], ©2018 IEEE.

be noticed, when the AMC is integrated around the antennas, the value of the standard deviation σ gets smaller in the range $\left[-25°, 10°\right]$. It means that the sensor with the low-RCS antennas presents less dispersion from the mean error value, and therefore, it offers a valuable increase in the system robustness.

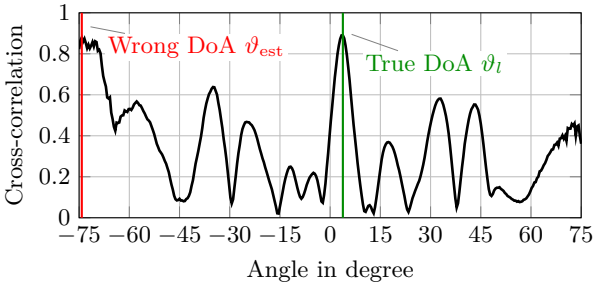

(a) Offset 1.0 mm.

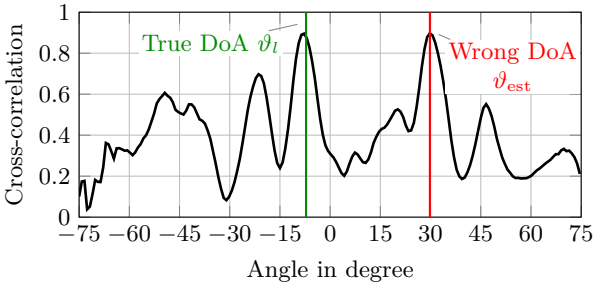

(b) Offset 2.0 mm.

Fig. 6.23: Selected cross-correlation results of the prototype without the AMC. The wrong DoA estimation leads to a strong increase in the angular error of Fig. 6.22a. Results from [107], ©2018 IEEE.

The experimental characterization presented in this chapter of a mm-wave MIMO radar equipped with a low-RCS antenna system demonstrates that the use of such antennas is a valuable solution for mitigating the problem of the multiple reflections between the radar and the car fascia. Indeed, the measurement results show clearly that the DoA estimation can benefit from the use of such a customized array design. In particular, with the approach first described in this thesis it is possible to reduce the errors in the DoA estimation. The experimental characterization shows an improve in the estimation of the DoA in an approximately 35°-range around the boresight direction.

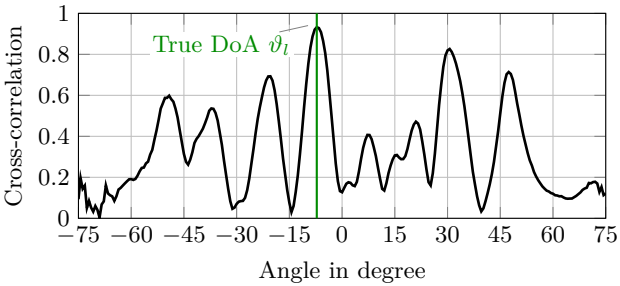

Fig. 6.24: Cross-correlation of the prototype without the AMC measured at an offset of 2.0 mm and for the DoA of −7.2°.

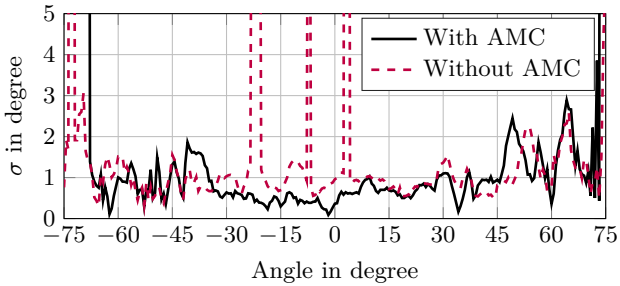

Fig. 6.25: Standard deviation of the DoA error computed from the two sets of measurements carried out using the prototypes without and with AMC. Results from [107], © 2018 IEEE.

7 Conclusion

The aim of this dissertation is the design and development of robust mm-wave antenna systems suitable for automotive radar applications. The main achievements of the study presented in this work are briefly listed below:

- design and development of a microstrip antenna array on a simple single-layer substrate with wideband and stable radiation performance;
- development of an optimization strategy for finding the position of transmitting and receiving antennas in a MIMO radar while taking the angular resolution requirements into consideration;
- development of microstrip antenna arrays with low-RCS properties to mitigate the multiple reflections between the bumper of the car and the radar sensor, when the latter is hidden integrated in the vehicle.

In the following, this three important outcomes are further described and summarized.

As a matter of course, the antenna system is a key component of the radar. To limit the fabrication costs, commercial radar sensors usually employ standard printed circuit board (PCB) technology for the development of the antennas. However, with this technology severe limitations and fabrication inaccuracies arise at mm-wave frequencies. To cope with them, this thesis proposes the use of a tolerance-optimized antenna design. In particular, this translates into the employment of wideband microstrip arrays, which can offer at the same time low design and fabrication complexity thanks to the single-layer substrate and relatively stable performances in the whole frequency range assigned to automotive radars. To this purpose, an 8-element microstrip array has been developed and tested. The basic radiating element is a patch antenna loaded with coplanar parasitic patches along its non-radiating edges. The measurement results demonstrates a good impedance matching and stable radiation performance against frequency in terms of gain and shape of the radiation pattern.

Modern automotive radar sensors are able to estimate the angular position of the target in addition to its distance and velocity. This can be typically done nowadays with the use of a MIMO radar, which offers an increased angular resolution performance while keeping the sensor dimensions reasonably compact. When orthogonal waveforms are employed, it is straightforward to define an equivalent virtual array that fully describes the property of the MIMO system. Moreover, the virtual array shows a virtual aperture larger than the physical aperture of the receiving elements of the radar, thus allowing to improve the angular resolution of the sensor. To synthesize a virtual array with given specifications in order to fulfill some angular resolution and sidelobe level requirements, it is necessary to employ an optimization algorithm. In fact, it is not possible to directly map the virtual array configuration into the real locations of the transmitters and the receivers. The optimization algorithm presented in this thesis for the development of MIMO radar antenna configurations is based on the use of a genetic algorithm. The novelty of the approach resides however in the definition of a proper fitness function. The classical skeleton of a genetic algorithm has been retailed, while the fitness function exploits the properties of the ambiguity function (AF). In particular, the fitness function aims to maximize the ambiguity-free range, where the AF can only reach values below a given threshold. The main advantage of defining such a fitness function is that it is intimately related to the direction-of-arrival (DoA) estimation problem, and it is able to correctly take into account all the angular direction of interest at the same time.

The optimization algorithm implemented in this work makes also the development of non-planar MIMO radars possible. A conformal shape offers in principle an increased field of view (FoV) compared to the typical planar mm-wave sensors. However, the additional degree of freedom given by this new shape makes the optimization more demanding. The simulation and measurement results demonstrate the correctness of the proposed approach. The beam pattern obtained by the experimental results collected with a MIMO radar sensor is in very good agreement with those extracted by the simulated ambiguity function. This result has been obtained for two different prototypes of conformal structure, whose design has been done with the proposed genetic algorithm.

The short wavelength at mm-wave frequencies allows the realization of quite compact radar sensors that can be even hidden integrated in the vehicle. More specifically, the most common solution preferred by the car manufacturers is

the placement of the sensor behind the car fascia. Unfortunately, a number of related problems come up. The bumper does not need to satisfy particular electromagnetic requirements. Due to its presence in front of the sensor, multiple reflections can occur, which in turn can lead to angular ambiguities and consequently to angular estimation errors. Since a change in the bumper design to suit this specific problem is not feasible in any practical case, this work proposes for the first time the idea of equipping the radar sensor with an antenna system with a low radar cross-section (RCS). The RCS of an antenna is actually the quantity that describes the amount of power reflected back by the antenna system towards the bumper. The significant advantage of this approach compared to other solutions known from the literature is the possibility to mitigate the problem of the multiple reflections, and thus improving the radar-vehicle integration, without any a priori knowledge of the car fascia.

This thesis deals thoroughly with the design of microstrip low-RCS antennas. The development of such an antenna system does not bring any increase in the fabrication complexity of the sensor. This is without any doubt a decisive advantage of the proposed approach, since for automotive radar applications cost, fabrication and design complexity, and sensor dimensions play a major role. The fundamental idea of the antenna design is to place an artificial magnetic conductor (AMC) on the really same substrate of the microstrip array. A phase compensation in the backscattering between the AMC and the array takes place leading to a strong reduction in the RCS. This kind of design strategy has been up to now used in the scientific community only for the development of low-RCS metasurfaces. This work contributes however towards the generalization of this elegant method for designing also low-RCS antennas.

Finally, a low-RCS MIMO antenna system has been tested in a mm-wave radar sensor. The radar measurements proves that the proposed approach can reduce the amount of the multiple reflections, and it can hence improve the DoA estimation conducted with the sensor in a realistic measurement scenario.

Appendix A: Design details of the 8-element array

This appendix presents further details regarding the design of the 8-element array of Chapter 4 and its feeding network. Moreover, the waveguide-to-microstrip transition used in different prototypes of this work is described.

A.1 Array dimensions

The dimensions of the antenna elements in the fabricated prototype of Fig. 4.15 on page 61 are listed in Tab. A.1. Keeping the same notation as in Fig. 4.2, the parameters g_i describe the gap width bewtween the central patch and the parasitic elements, $W_{\mathrm{par},i}$ and $L_{\mathrm{par},i}$ represent the width and length of the parasitic patch, respectively, while W_i is the central patch width. The length of the central patch is the same for all the elements, and it has been set to 1.03 mm. The distance between adjacent patches is 2.23 mm. Due to the symmetry of the design, the index i, which is related to the antenna element, varies in the range $[1, \ldots, 4]$, see Fig. A.1.

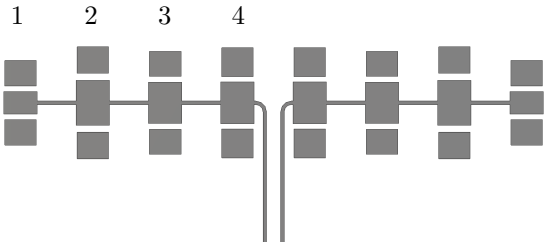

Fig. A.1: Sketch of the 8-element array after the balun. The two branches are symmetrical.

	i-th element			
	1	2	3	4
W_{par} in mm	0.79	0.82	0.77	0.89
L_{par} in mm	0.97	0.97	0.98	0.97
g in mm	0.17	0.22	0.17	0.16
W in mm	0.69	1.38	1.28	1.28

Tab. A.1: Dimensions of the antenna elements of the fabricated array. The antenna element with index i=1 represents the load at the end of the series-fed chain, while the one with index i=4 is closer to the balun output, see Fig. A.1.

A.2 Feeding network

The two arms of the array of Fig. A.1, and also in the case of the 2-elements array designs shown in Chapter 4, need 180°-phase difference at the array input ports to avoid any beam splitting in boresight direction. To this purpose, a balun is required. The model of the feeding network can be seen in Fig. A.2. It can be described as a 3-port balun derived from a 4-port branchline coupler.

The port 1 of the balun, i.e., the input port, has been fed by the waveguide-to-microstrip transition in the fabricated prototype of Fig. 4.15, while the two balun output ports 2 and 3 feed the array.

The design of the balun is based on the model presented in [111]. The main advantage of this configuration is the quite wideband behavior, that gives satisfactory results in the whole frequency range of interest. This can be noticed for example in Fig. A.3a, which shows the input reflection coefficient at the

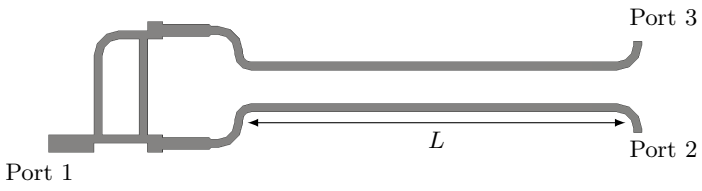

Fig. A.2: Feeding network to provide 180°-phase difference for center feeding the array. The length L is equal to 4.83 mm.

three ports calculated by means of full-wave simulations. In the same way, Fig. A.3b presents the amplitude of the transmission coefficients between the input and the output ports and the coupling between the output ports. Finally, Fig. A.3c depicts the phase of the transmission coefficients. It can be observed that a quite constant phase difference can be successfully achieved.

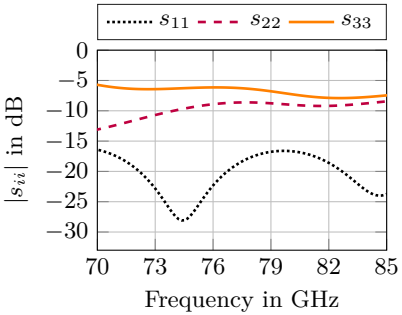

(a) Reflection coefficients.

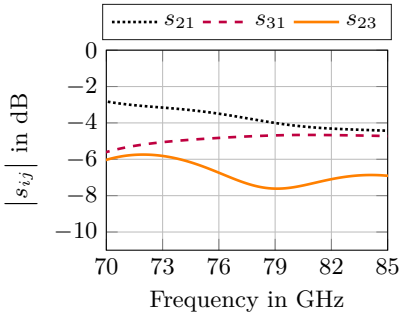

(b) Transmission coefficients s_{21} and s_{31} and coupling between the output ports s_{23}.

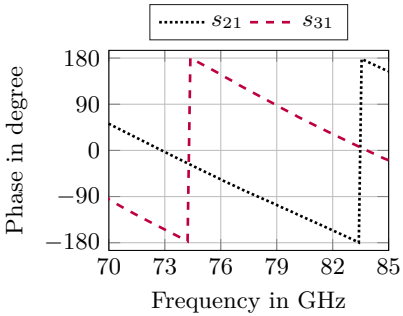

(c) Phase of the transmission coefficients s_{21} and s_{31}.

Fig. A.3: Full-wave simulation results of the array feeding network.

A.3 Waveguide-to-microstrip transition

For measurement purpose a waveguide-to-microstrip transition is required to feed the array. In this thesis, the model originally proposed in [112] has been adapted to work in the frequency range assigned to automotive radars. The design offers a simple single layer configuration with a good impedance matching and sufficient low losses in the whole frequency band of interest.

The transition consists of a microstrip probe, with a patch shape, inserted inside the rectangular waveguide, which is perpendicular to the substrate. The waveguide has been connected to the backside of the PCB to avoid having a bulky metal element on the same side of the antenna elements. On the top side of the substrate, the microstrip probe faces a metal cap that terminates the waveguide. The inner height of the metal cap is 0.55 mm.

The top view of the transition can be seen in Fig. A.4. The width and the length of the microstrip probe are 1.30 mm and 1.00 mm, respectively, while the width of microstrip line is 0.23 mm. A number of grounded vias surround the microstrip probe; their diameter is 0.30 mm.

The waveguide that feeds the transition from the back has been realized by milling it in an aluminum block, which also gives mechanical stability to

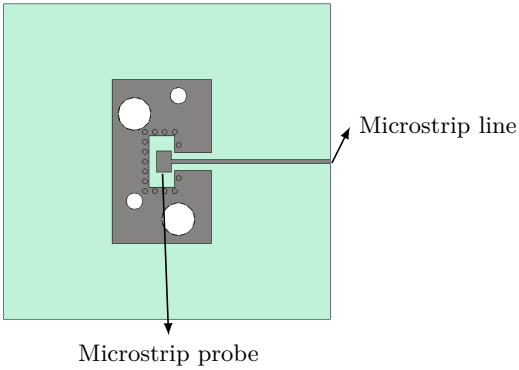

Fig. A.4: Top view of the waveguide-to-microstrip transition without the metal cap. The holes through the PCB allow to screw the metal cap — which terminates the waveguide — to the aluminum support on the backside.

the really thin substrate. The waveguide has the standard inner dimensions typically employed in the E-band, that is to say 3.10 mm × 1.55 mm.

Appendix B: Additional measurement results

This appendix completes the experimental characterization of the low-RCS patch array presented in Fig. 6.5 on page 97. In particular, the measured radiation pattern of the prototype has been compared to the one of a standard patch array without the use of the AMC, as also described in Section 6.2.1. For the sake of completeness, this section presents additional plots collected at 76 GHz and from 78 GHz to 81 GHz.

These measurement results confirm again that the presence of the AMC does not degrade the radiation pattern of the array.

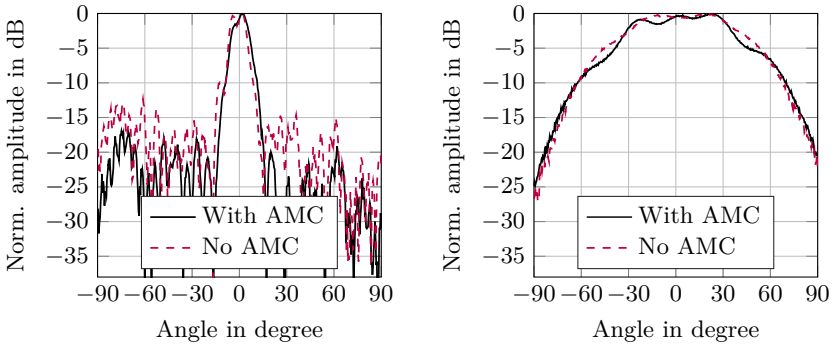

(a) E-plane. **(b)** H-plane.

Fig. B.1: Measured radiation pattern at 76 GHz.

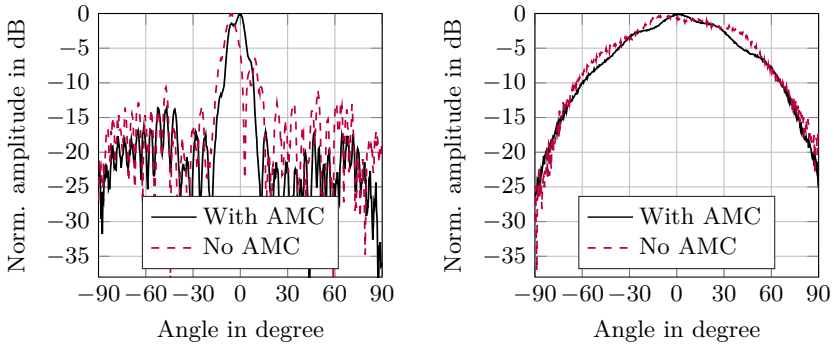

(a) E-plane. **(b)** H-plane.

Fig. B.2: Measured radiation pattern at 78 GHz.

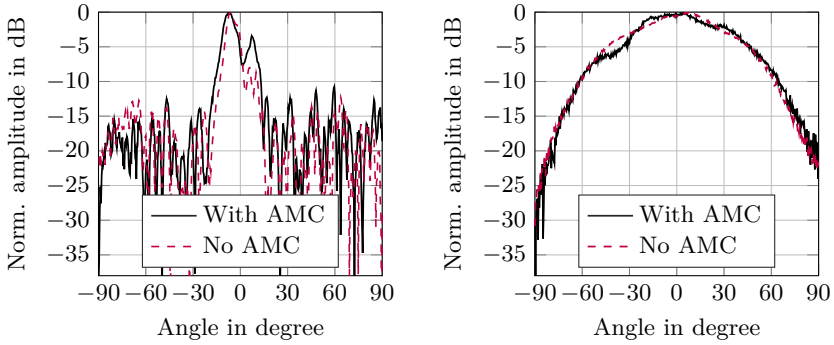

(a) E-plane. **(b)** H-plane.

Fig. B.3: Measured radiation pattern at 79 GHz.

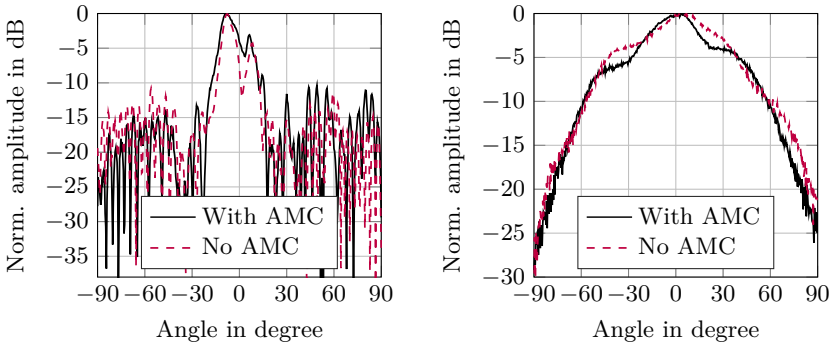

(a) E-plane. **(b)** H-plane.

Fig. B.4: Measured radiation pattern at 80 GHz.

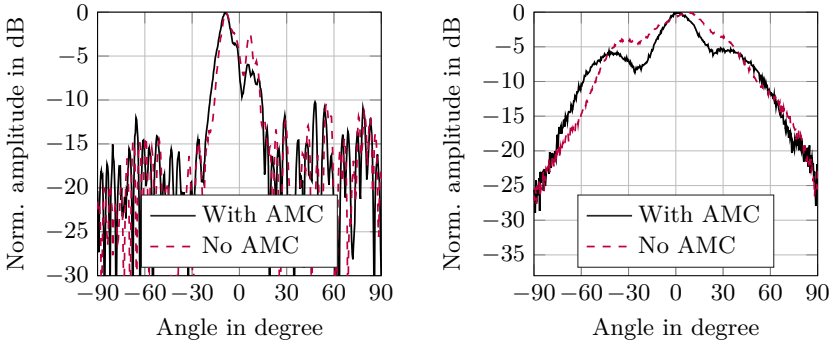

(a) E-plane. **(b)** H-plane.

Fig. B.5: Measured radiation pattern at 81 GHz.

Appendix C: Some notes on the ambiguity function

In Chapter 2 the concept of the ambiguity function (AF) has been introduced. In particular, the definition has been given with (2.2.4) on page 13.

By cutting out a row or a column from the plot of the ambiguity function the typical plot of a beam pattern can be obtained, see Fig. 2.4 on page 17. Some additional comments are however required for a correct understanding of this point.

As an example, a uniform linear array with N identical elements can be assumed. The single radiating elements have a complex radiation pattern given by $C(\psi)$, which is a complex scalar that describes the field strength in the angular direction ψ. The radiation pattern can be taken into account in the definition of the array steering vector as

$$\boldsymbol{s}'(\psi) = C(\psi)\boldsymbol{s}(\psi)\,, \tag{C.1}$$

where $\boldsymbol{s}(\psi)$ is the array steering vector of the ideal counterpart, namely an N-element ULA with isotropic radiators.

Using $\boldsymbol{s}'(\psi)$ it is possible to calculate the ambiguity function according to (2.2.4). In particular, the scalar product in the numerator becomes

$$\left|\boldsymbol{s}'^{H}(\psi_i)\cdot\boldsymbol{s}'(\psi_j)\right| = \left|C^H(\psi_i)\boldsymbol{s}^H(\psi_i)\cdot C(\psi_j)\boldsymbol{s}(\psi_j)\right| \tag{C.2}$$

$$= \left|C^H(\psi_i)\right|\,\left|C(\psi_j)\right|\,\left|\boldsymbol{s}^H(\psi_i)\cdot\boldsymbol{s}(\psi_j)\right|\,, \tag{C.3}$$

while in the denominator the norm is

$$\parallel \boldsymbol{s}'(\psi) \parallel = \parallel C(\psi)\boldsymbol{s}(\psi) \parallel = \left|C(\psi)\right| \parallel \boldsymbol{s}(\psi) \parallel\,, \tag{C.4}$$

due to the homogeneity of the L^2-norm. Thus, from (C.3) and (C.4) it can be concluded that the radiation pattern $C(\psi)$ cancels out in (2.2.4). The same ambiguity function of the case of an N-element ULA with isotropic radiators can be obtained. This effect happens when the N elements of the array have the same radiation pattern.

The normalization in (2.2.4) suppresses the effect of the single radiating element in an ULA; hence, it is not possible to obtain in this specific case the radiation pattern of the array as multiplication of the element and array factor. The typical directive properties of the single element, which acts as an angular filter that lowers the radiated power of the array for angles close to the endfire direction [113], cannot be observed for an array of identical radiating elements when the plot of the the beam pattern has been obtained from the AF.

Bibliography

[1] J. Conlon and K. Nagatsuka, "Trends in Automated Driving and Advanced Driver Assistance Systems in Europe," *Hitachi Review*, vol. 67, no. 1, pp. 39–44, 2018.

[2] J. Hasch, E. Topak, R. Schnabel, T. Zwick, R. Weigel, and C. Waldschmidt, "Millimeter-Wave Technology for Automotive Radar Sensors in the 77 GHz Frequency Band," *IEEE Transactions on Microwave Theory and Techniques*, vol. 60, no. 3, pp. 845–860, March 2012.

[3] J. Hasch, "Driving Towards 2020: Automotive Radar Technology Trends," in *IEEE MTT-S International Conference on Microwaves for Intelligent Mobility (ICMIM)*. IEEE, April 2015.

[4] Robert Bosch GmbH, *Radar-based driver assistance systems – Mid-range radar sensor*, 2017.

[5] F. Roos, D. Kellner, J. Dickmann, and C. Waldschmidt, "Reliable Orientation Estimation of Vehicles in High-Resolution Radar Images," *IEEE Transactions on Microwave Theory and Techniques*, vol. 64, no. 9, pp. 2986–2993, Sept. 2016.

[6] W. Menzel and A. Moebius, "Antenna Concepts for Millimeter-Wave Automotive Radar Sensors," *Proceedings of the IEEE*, vol. 100, no. 7, pp. 2372–2379, July 2012.

[7] J. Li and P. Stoica, "MIMO Radar with Colocated Antennas," *IEEE Signal Processing Magazine*, vol. 24, no. 5, pp. 106–114, Sept. 2007.

[8] R. Schnabel, D. Mittelstrab, T. Binzer, C. Waldschmidt, and R. Weigel, "Reflection, Refraction, and Self-Jamming," *IEEE Microwave Magazine*, vol. 13, no. 3, pp. 107–117, 2012.

[9] "Wie funktioniert das ACC von Volkswagen? KFZ Technik: Voice over Cars!" http://www.rad-ab.com/2017/05/01/wie-funktioniert-das-acc-von-volkswagen-kfz-technik-voice-over-cars/, accessed: 22.02.2018.

[10] J. Dickmann, N. Appenrodt, J. Klappstein, H.-L. Bloecher, M. Muntzinger, A. Sailer, M. Hahn, and C. Brenk, "Making Bertha See Even More: Radar Contribution," *IEEE Access*, vol. 3, pp. 1233–1247, 2015.

[11] S. Pacheco, R. Reuter, S. Trotta, D. Salle, and J. John, "SiGe Technology and Circuits for Automotive Radar Applications," in *IEEE 11th Topical Meeting on Silicon Monolithic Integrated Circuits in RF Systems*. IEEE, Jan. 2011.

[12] O. Khan, J. Meyer, K. Baur, and C. Waldschmidt, "Hybrid Thin Film Antenna for Automotive Radar at 79 GHz," *IEEE Transactions on Antennas and Propagation*, vol. 65, no. 10, pp. 5076–5085, Oct. 2017.

[13] R. Schnabel, R. Hellinger, D. Steinbuch, J. Selinger, M. Klar, and B. Lucas, "Development of a mid range automotive radar sensor for future driver assistance systems," *International Journal of Microwave and Wireless Technologies*, vol. 5, no. 1, p. 15–23, 2013.

[14] T. Binzer, M. Klar, and V. Groß, "Development of 77 GHz Radar Lens Antennas for Automotive Applications Based on Given Requirements," in *2nd International ITG Conference on Antennas*, March 2007, pp. 205–209.

[15] E. Topak, J. Hasch, and T. Zwick, "Compact Topside Millimeter-Wave Waveguide-to-Microstrip Transitions," *IEEE Microwave and Wireless Components Letters*, vol. 23, no. 12, pp. 641–643, Dec. 2013.

[16] A. E. I. Lamminen, J. Saily, and A. R. Vimpari, "60-GHz Patch Antennas and Arrays on LTCC With Embedded-Cavity Substrates," *IEEE Transactions on Antennas and Propagation*, vol. 56, no. 9, pp. 2865–2874, Sept. 2008.

[17] F. Bauer, X. Wang, W. Menzel, and A. Stelzer, "A 79-GHz Radar Sensor in LTCC Technology Using Grid Array Antennas," *IEEE Transactions on Microwave Theory and Techniques*, vol. 61, no. 6, pp. 2514–2521, June 2013.

[18] F. Sickinger, E. Weissbrodt, and M. Vossiek, "76–81 GHz LTCC antenna for an automotive miniature radar frontend," *International Journal of*

Microwave and Wireless Technologies, vol. 10, no. 5-6, pp. 729–736, June 2018.

[19] A. Bhutani, H. Gulan, B. Goettel, C. Heine, T. Thelemann, M. Pauli, and T. Zwick, "122 GHz Aperture-Coupled Stacked Patch Microstrip Antenna in LTCC Technology," in *10th European Conference on Antennas and Propagation (EuCAP)*. IEEE, April 2016.

[20] F. Bechtold, "A comprehensive overview on today's ceramic substrate technologies," in *European Microelectronics and Packaging Conference*, June 2009, pp. 1–12.

[21] M. Mosalanejad, I. Ocket, C. Soens, and G. A. E. Vandenbosch, "Wideband Compact Comb-Line Antenna Array for 79 GHz Automotive Radar Applications," *IEEE Antennas and Wireless Propagation Letters*, vol. 17, no. 9, pp. 1580–1583, Sept. 2018.

[22] M. Kronauge and H. Rohling, "New Chirp Sequence Radar Waveform," *IEEE Transactions on Aerospace and Electronic Systems*, vol. 50, no. 4, pp. 2870–2877, Oct. 2014.

[23] M. Schoor, "Hochauflösende Winkelschätzung für automobile Radarsysteme," Ph.D. dissertation, Universität Stuttgart, 2010.

[24] J. D. Kraus and R. J. Marhefka, *Antennas*, 3rd ed. McGraw-Hill, 2001.

[25] L. Rayleigh, "XXXI. Investigations in Optics, with special reference to the Spectroscope," *The London, Edinburgh, and Dublin Philosophical Magazine and Journal of Science*, vol. 8, no. 49, pp. 261–274, Oct. 1879.

[26] E. Hecht, *Optics, Global Edition*. Pearson, 2016.

[27] M. Köhler, J. Hasch, H. L. Blöcher, and L.-P. Schmidt, "Feasibility of automotive radar at frequencies beyond 100 GHz," *International Journal of Microwave and Wireless Technologies*, vol. 5, no. 1, pp. 49–54, Dec. 2012.

[28] A.D.C. GmbH, "ARS 30X /-2 /-2C/-2T/-21 Radar-Sensor 77 GHz," Data sheet.

[29] J. Singh, B. Ginsburg, S. Rao, and K. Ramasubramanian, "AWR1642 mmWave sensor: 76–81-GHz radar-on-chip for short-range radar applications," Texas Instruments, May 2017.

[30] M. Eric, A. Zejak, and M. Obradovic, "Ambiguity characterization of arbitrary antenna array: type I ambiguity," in *IEEE 5th International Symposium on Spread Spectrum Techniques and Applications - Proceedings. Spread Technology to Africa (Cat. No.98TH8333)*, vol. 2, Sept. 1998, pp. 399–403.

[31] R. S. Campos and L. Lovisolo, *RF Positioning: Fundamentals, Applications and Tools (GNSS Technology and Applications)*. Artech House, 2015.

[32] H. V. Nguyen and L. Bai, "Cosine Similarity Metric Learning for Face Verification," in *Computer Vision – ACCV 2010*. Springer Berlin Heidelberg, 2011, pp. 709–720.

[33] R. Schmidt, "Multiple Emitter Location and Signal Parameter Estimation," *IEEE Transactions on Antennas and Propagation*, vol. 34, no. 3, pp. 276–280, March 1986.

[34] A. A. H. Azremi, M. Costa, V. Koivunen, and P. Vainikainen, "Ambiguity analysis of isolation - based multi-antenna structures on mobile terminal," in *5th European Conference on Antennas and Propagation (EUCAP)*, April 2011, pp. 552–556.

[35] P. Häcker and B. Yang, "Single snapshot DOA estimation," *Advances in Radio Science*, vol. 8, pp. 251–256, oct 2010.

[36] T. E. Tuncer and B. Friedlander, Eds., *Classical and Modern Direction-of-Arrival Estimation*. Elsevier Science, 2009.

[37] M. C. Sullivan, *Practical Array Processing*. McGraw-Hill Education, 2008.

[38] M. A. Richards, J. A. Scheer, and W. A. Holm, Eds., *Principles of Modern Radar: Basic principles*. Institution of Engineering and Technology, Jan. 2010.

[39] C. Vasanelli, R. Batra, A. D. Serio, F. Boegelsack, and C. Waldschmidt, "Assessment of a Millimeter-Wave Antenna System for MIMO Radar Applications," *IEEE Antennas and Wireless Propagation Letters*, vol. 16, pp. 1261–1264, 2017.

[40] M. Harter, J. Hildebrandt, A. Ziroff, and T. Zwick, "Self-Calibration of a 3-D-Digital Beamforming Radar System for Automotive Applications With Installation Behind Automotive Covers," *IEEE Transactions on Microwave Theory and Techniques*, vol. 64, no. 9, pp. 2994–3000, Sept. 2016.

[41] F. Pfeiffer and E. Biebl, "Inductive Compensation of High-Permittivity Coatings on Automobile Long-Range Radar Radomes," *IEEE Transactions on Microwave Theory and Techniques*, vol. 57, no. 11, pp. 2627–2632, Nov. 2009.

[42] A. Melzer, A. Onic, F. Starzer, and M. Huemer, "Short-Range Leakage Cancelation in FMCW Radar Transceivers Using an Artificial On-Chip Target," *IEEE Journal of Selected Topics in Signal Processing*, vol. 9, no. 8, pp. 1650–1660, Dec. 2015.

[43] C. Vasanelli, F. Bögelsack, and C. Waldschmidt, "Reducing the Radar Cross-Section of Microstrip Arrays Using AMC Structures for the Vehicle Integration of Automotive Radars," *IEEE Transactions on Antennas and Propagation*, vol. 66, no. 3, pp. 1456–1464, March 2018.

[44] F. Fitzek, R. H. Raßhofer, and E. M. Biebl, "Broadband matching of high-permittivity coatings with frequency selective surfaces," in *German Microwave Conference*, March 2011, pp. 1–4.

[45] E. F. Knott, J. F. Schaeffer, and M. T. Tulley, *Radar Cross Section*, 2nd ed. Scitech Publishing, 2004.

[46] S. Riegger and W. Wiesbeck, "Wide-Band Polarimetry and Complex Radar Cross Section Signatures," *Proceedings of the IEEE*, vol. 77, no. 5, pp. 649–658, May 1989.

[47] J. Bechter, F. Roos, and C. Waldschmidt, "Compensation of Motion-Induced Phase Errors in TDM MIMO Radars," *IEEE Microwave and Wireless Components Letters*, vol. 27, no. 12, pp. 1164–1166, Dec. 2017.

[48] R. Feger, C. Wagner, S. Schuster, S. Scheiblhofer, H. Jager, and A. Stelzer, "A 77-GHz FMCW MIMO Radar Based on an SiGe Single-Chip Transceiver," *IEEE Transactions on Microwave Theory and Techniques*, vol. 57, no. 5, pp. 1020–1035, May 2009.

[49] H. Krim and M. Viberg, "Two Decades of Array Signal Processing Research: The Parametric Approach," *IEEE Signal Processing Magazine*, vol. 13, no. 4, pp. 67–94, July 1996.

[50] A. Haimovich, R. Blum, and L. Cimini, "MIMO Radar with Widely Separated Antennas," *IEEE Signal Processing Magazine*, vol. 25, no. 1, pp. 116–129, 2008.

[51] C. M. Schmid, R. Feger, C. Pfeffer, and A. Stelzer, "Motion Compensation and Efficient Array Design for TDMA FMCW MIMO Radar Systems," in *6th European Conference on Antennas and Propagation (EUCAP)*. IEEE, March 2012.

[52] J. J. M. de Wit, W. L. van Rossum, and A. J. de Jong, "Orthogonal Waveforms for FMCW MIMO Radar," in *IEEE RadarCon (RADAR)*. IEEE, May 2011.

[53] V. Giannini, D. Guermandi, Q. Shi, A. Medra, W. V. Thillo, A. Bourdoux, and P. Wambacq, "A 79 GHz Phase-Modulated 4 GHz-BW CW Radar Transmitter in 28 nm CMOS," *IEEE Journal of Solid-State Circuits*, vol. 49, no. 12, pp. 2925–2937, Dec. 2014.

[54] D. Schindler, B. Schweizer, C. Knill, J. Hasch, and C. Waldschmidt, "MIMO-OFDM Radar Using a Linear Frequency Modulated Carrier to Reduce Sampling Requirements," *IEEE Transactions on Microwave Theory and Techniques*, vol. 66, no. 7, pp. 3511–3520, July 2018.

[55] M. Marcus and H. Minc, *A Survey of Matrix Theory and Matrix Inequalities*, ser. Allyn and Bacon series in Advanced Mathematics. Allyn and Bacon, 1964.

[56] A. Hjørungnes, *Complex-Valued Matrix Derivatives: With Applications in Signal Processing and Communications*. Cambridge University Press, 2011.

[57] J. Li and P. Stoica, *MIMO Radar Signal Processing*. Wiley-IEEE Press, 2008.

[58] I. Bekkerman and J. Tabrikian, "Target Detection and Localization Using MIMO Radars and Sonars," *IEEE Transactions on Signal Processing*, vol. 54, no. 10, pp. 3873–3883, Oct. 2006.

[59] C. M. Schmid, R. Feger, C. Wagner, and A. Stelzer, "Design of a Linear Non-uniform Antenna Array for a 77-GHz MIMO FMCW Radar," in *IEEE MTT-S International Microwave Workshop on Wireless Sensing, Local Positioning, and RFID*. IEEE, Sept. 2009.

[60] J. H. Holland, "Outline for a Logical Theory of Adaptive Systems," *Journal of the ACM*, vol. 9, no. 3, pp. 297–314, jul 1962.

[61] D. E. Goldberg, *Genetic Algorithms in Search, Optimization, and Machine Learning*. Addison-Wesley Professional, 1989.

[62] R. Haupt, "An Introduction to Genetic Algorithms for Electromagnetics," *IEEE Antennas and Propagation Magazine*, vol. 37, no. 2, pp. 7–15, April 1995.

[63] D. Boeringer and D. Werner, "Particle Swarm Optimization Versus Genetic Algorithms for Phased Array Synthesis," *IEEE Transactions on Antennas and Propagation*, vol. 52, no. 3, pp. 771–779, March 2004.

[64] D. Weile and E. Michielssen, "Genetic Algorithm Optimization Applied to Electromagnetics: a Review," *IEEE Transactions on Antennas and Propagation*, vol. 45, no. 3, pp. 343–353, March 1997.

[65] C. Vasanelli, R. Batra, and C. Waldschmidt, "Optimization of a MIMO Radar Antenna System for Automotive Applications," in *11th European Conference on Antennas and Propagation (EUCAP)*. IEEE, March 2017, pp. 1113–1117.

[66] M. Steiner, O. Hammouda, and C. Waldschmidt, "Ego-Motion Estimation using Distributed Single-Channel Radar Sensors," in *IEEE MTT-S International Conference on Microwaves for Intelligent Mobility (ICMIM)*. IEEE, Apr. 2018.

[67] "KoRRund—Konforme multistatische Radarkonfigurationen zur Rundumsicht für das automatisierte Fahren," https://www.elektronikforschung.de/projekte/korrund, accessed: 15.10.2018.

[68] C. Vasanelli, B. Meinecke, J. Mayer, O. Elsayad, P. Hügler, F. Roos, T. Zwick, and C. Waldschmidt, "Characterization of mm-Wave Conformal Antenna Arrays for a 3×8 MIMO Radar," in *International Conference on Electromagnetics in Advanced Applications (ICEAA)*, 2019.

[69] P. Knott, T. Bertuch, H. Wilden, O. Peters, A. R. Brenner, and I. Walterscheid, "SAR Experiments Using a Conformal Antenna Array Radar Demonstrator," *International Journal of Antennas and Propagation*, vol. 2012, pp. 1–7, 2012.

[70] Rogers Corporation, *RO3000® Series Circuit Materials*, Revised 1400 092518.

[71] P. Hügler, F. Roos, M. Schartel, M. Geiger, and C. Waldschmidt, "Radar Taking Off: New Capabilities for UAVs," *IEEE Microwave Magazine*, vol. 19, no. 7, pp. 43–53, Nov. 2018.

[72] S. Maci and G. Biffi Gentili, "Dual-Frequency Patch Antennas," *IEEE Antennas and Propagation Magazine*, vol. 39, no. 6, pp. 13–20, 1997.

[73] A. Shackelford, K.-F. Lee, and K. Luk, "Design of Small-Size Wide-Bandwidth Microstrip-Patch Antennas," *IEEE Antennas and Propagation Magazine*, vol. 45, no. 1, pp. 75–83, Feb. 2003.

[74] M. Frei, "Antennen für automobile Radarsensoren bei 79 GHz," Ph.D. dissertation, Universität Ulm, 2014.

[75] O. Khan, J. Pontes, X. Li, and C. Waldschmidt, "A Wideband Variable Width Microstrip Grid Array Antenna," in *11th European Radar Conference*. IEEE, Oct. 2014.

[76] O. Khan, J. Meyer, K. Baur, and C. Waldschmidt, "Substrate Integrated Waveguide Slot-Fed Grid Array Antenna," in *European Radar Conference (EuRAD)*. IEEE, Sept. 2015.

[77] G. Kumar and K. Gupta, "Nonradiating Edges and Four Edges Gap-Coupled Multiple Resonator Broad-Band Microstrip Antennas," *IEEE*

Transactions on Antennas and Propagation, vol. 33, no. 2, pp. 173–178, Feb. 1985.

[78] K.-L. Wong and J.-Y. Sze, "Dual-frequency slotted rectangular microstrip antenna," *Electronics Letters*, vol. 34, no. 14, p. 1368, 1998.

[79] S. Maci, G. Biffi Gentili, P. Piazzesi, and C. Salvador, "Dual-band slot-loaded patch antenna," *IEE Proceedings - Microwaves, Antennas and Propagation*, vol. 142, no. 3, p. 225, 1995.

[80] J.-H. Lu, "Single-feed dual-frequency rectangular microstrip antenna with pair of step-slots," *Electronics Letters*, vol. 35, no. 5, p. 354, 1999.

[81] C. A. Balanis, *Antenna Theory: Analysis and Design*, 2nd ed. Wiley, 1996.

[82] J. Carson, "Reciprocal Theorems in Radio Communication," *Proceedings of the IRE*, vol. 17, no. 6, pp. 952–956, June 1929.

[83] M. Neiman, "The Principle of Reciprocity in Antenna Theory," *Proceedings of the IRE*, vol. 31, no. 12, pp. 666–671, Dec. 1943.

[84] J. Andersen and A. Frandsen, "Absorption Efficiency of Receiving Antennas," *IEEE Transactions on Antennas and Propagation*, vol. 53, no. 9, pp. 2843–289, Sept. 2005.

[85] J. Appel-Hansen, "Accurate Determination of Gain and Radiation Patterns by Radar Cross-Section Measurements," *IEEE Transactions on Antennas and Propagation*, vol. 27, no. 5, pp. 640–646, Sept. 1979.

[86] S. Shrestha, M. Balachandran, M. Agarwal, L.-H. Zou, and K. Varahramyan, "A Method to Measure Radar Cross Section Parameters of Antennas," *IEEE Transactions on Antennas and Propagation*, vol. 56, no. 11, pp. 3494–3500, Nov. 2008.

[87] M. A. C. Niamien, S. Collardey, and K. Mahdjoubi, "Absorption and Scattering Properties of a Receiving Patch Antenna," in *9th European Conference on Antennas and Propagation (EuCAP)*, May 2015, pp. 1–4.

[88] S. Hu, H. Chen, C. L. Law, Z. Shen, L. Zhu, W. Zhang, and W. Dou, "Backscattering cross section of ultrawideband antennas," *IEEE Antennas and Wireless Propagation Letters*, vol. 6, pp. 70–73, 2007.

[89] C. Knop and G. Lichtenwalter, "Radar Echo Reduction Using Circulators," *IEEE Transactions on Antennas and Propagation*, vol. 14, no. 6, pp. 789–790, Nov. 1966.

[90] N. Nakamoto, T. Takahashi, T. Nomura, M. Otsuka, and H. Miyashita, "A Method to Measure the Antenna Mode and Structural Mode for Antenna RCS Reduction Using Circulator and Phase Shifter," in *International Symposium on Antennas and Propagation Conference Proceedings*. IEEE, Dec. 2014.

[91] M. Paquay, J.-C. Iriarte, I. Ederra, R. Gonzalo, and P. de Maagt, "Thin AMC Structure for Radar Cross-Section Reduction," *IEEE Transactions on Antennas and Propagations*, vol. 55, no. 12, pp. 3630–3638, Dec. 2007.

[92] C. Vasanelli, F. Boegelsack, and C. Waldschmidt, "Design and Experimental Characterization of a Surface With Low Radar Cross-Section at Millimeter-Wave Frequencies," in *46th European Microwave Conference (EuMC)*, Oct. 2016.

[93] F. Capolino, *Theory and Phenomena of Metamaterials (Metamaterials Handbook)*. CRC Press, 2009.

[94] D. Sievenpiper, L. Zhang, R. Broas, N. Alexopolous, and E. Yablonovitch, "High-Impedance Electromagnetic Surfaces with a Forbidden Frequency Band," *IEEE Transactions on Microwave Theory and Techniques*, vol. 47, no. 11, pp. 2059–2074, 1999.

[95] W. Chen, C. A. Balanis, and C. R. Birtcher, "Checkerboard EBG Surfaces for Wideband Radar Cross Section Reduction," *IEEE Transactions on Antennas and Propagation*, vol. 63, no. 6, pp. 2636–2645, June 2015.

[96] A. Y. Modi, C. A. Balanis, C. R. Birtcher, and H. N. Shaman, "New Class of RCS-Reduction Metasurfaces Based on Scattering Cancellation Using Array Theory," *IEEE Transactions on Antennas and Propagation*, pp. 1–1, 2018.

[97] R. Bhalla, J. Moore, and H. Ling, "A Global Scattering Center Representation of Complex Targets Using the Shooting and Bouncing Ray Technique," *IEEE Transactions on Antennas and Propagation*, vol. 45, no. 12, pp. 1850–1856, 1997.

[98] H. Singh and R. M. Jha, *Active Radar Cross Section Reduction.* Cambridge University Press, 2015.

[99] F. Costa, A. Monorchio, and G. Manara, "Analysis and Design of Ultra Thin Electromagnetic Absorbers Comprising Resistively Loaded High Impedance Surfaces," *IEEE Transactions on Antennas and Propagation*, vol. 58, no. 5, pp. 1551–1558, May 2010.

[100] S. Genovesi, F. Costa, and A. Monorchio, "Low-Profile Array With Reduced Radar Cross Section by Using Hybrid Frequency Selective Surfaces," *IEEE Transactions on Antennas and Propagation*, vol. 60, no. 5, pp. 2327–2335, May 2012.

[101] Y. Zhang, J. von Hagen, M. Younis, C. Fischer, and W. Wiesbeck, "Planar Artificial Magnetic Conductors and Patch Antennas," *IEEE Transactions on Antennas and Propagation*, vol. 51, no. 10, pp. 2704–2712, Oct. 2003.

[102] A. Foroozesh and L. Shafai, "Investigation Into the Application of Artificial Magnetic Conductors to Bandwidth Broadening, Gain Enhancement and Beam Shaping of Low Profile and Conventional Monopole Antennas," *IEEE Transactions on Antennas and Propagation*, vol. 59, no. 1, pp. 4–20, Jan. 2011.

[103] J. C. I. Galarregui, A. T. Pereda, J. L. M. de Falcon, I. Ederra, R. Gonzalo, and P. de Maagt, "Broadband Radar Cross-Section Reduction Using AMC Technology," *IEEE Transactions on Antennas and Propagation*, vol. 61, no. 12, pp. 6136–6143, Dec. 2013.

[104] C. Vasanelli, F. Bögelsack, and C. Waldschmidt, "A Complex Low-RCS Antenna System for the Placement of mm-Wave Automotive Radars Behind Car Bumpers," in *12th European Conference on Antennas and Propagation (EuCAP)*, London, United Kingdom (Great Britain), 2018.

[105] "Time Domain Analysis Using a Network Analyzer," Agilent Application Note 1287-12.

[106] D. F. Sievenpiper, "High-Impedance Electromagnetic Surfaces," Ph.D. dissertation, University of California, Los Angeles, 1999.

[107] C. Vasanelli, K. Baur, M. Nezadal, H. Gulan, M. Steiner, and C. Waldschmidt, "Characterization of a mm-Wave Automotive Radar with a Low-RCS MIMO Antenna System," in *IEEE Conference on Antenna Measurements and Applications (CAMA)*, 2018.

[108] P. Häcker and B. Yang, "Mixed-Order and Higher-Order Ambiguity Functions," in *IEEE Intelligent Vehicles Symposium (IV)*. IEEE, June 2011.

[109] F. Athley, "Threshold Region Performance of Maximum Likelihood Direction of Arrival Estimators," *IEEE Transactions on Signal Processing*, vol. 53, no. 4, pp. 1359–1373, April 2005.

[110] W. Leupold *et al.*, *Analysis für Ingenieure*. Fachbuchverlag Leipzig, 1974.

[111] J.-L. Li, S.-W. Qu, and Q. Xue, "Investigation of a Compact and Broadband Balun," *Microwave and Optical Technology Letters*, vol. 50, no. 5, pp. 1380–1384, 2008.

[112] J. Machac and W. Menzel, "On the design of waveguide-to-microstrip and waveguide-to-coplanar line transitions," in *23rd European Microwave Conference*. IEEE, Sept. 1993.

[113] H. J. Visser, *Array and Phased Array Antenna Basics*. Wiley, 2005.

List of own publications and awards

This section lists the author's publications.

Articles in peer-reviewed scientific journals

- C. Vasanelli, F. Bögelsack, and C. Waldschmidt, *Reducing the Radar Cross-Section of Microstrip Arrays Using AMC Structures for the Vehicle Integration of Automotive Radars*, in IEEE Trans. Antennas Propag., vol. 66, no. 3, pp. 1456–1464, 2018.

- C. Vasanelli, R. Batra, A. Di Serio, F. Boegelsack, and C. Waldschmidt, *Assessment of a Millimeter-Wave Antenna System for MIMO Radar Applications*, in IEEE Antennas Wireless Propag. Letters, vol. 16, pp. 1261–1264, 2017.

Articles in conference proceedings with peer-review process

- C. Vasanelli, B. Meinecke, J. Mayer, O. Elsayad, P. Hügler, F. Roos, T. Zwick, and C. Waldschmidt, *Characterization of mm-Wave Conformal Antenna Arrays for a 3×8 MIMO Radar*, International Conf. Electromagnetics in Advanced Applications (ICEAA 2019), Granada, 2019.

- F. Roos, P. Hügler, L. L. Tovar Torres, C. Knill, J. Schlichenmaier, C. Vasanelli, N. Appenrodt, J. Dickmann, and C. Waldschmidt, *Compressed Sensing based Single Snapshot DoA Estimation for Sparse MIMO Radar Arrays*, German Microwave Conf. (GeMiC), Stuttgart, 2019.

- C. Vasanelli, K. Baur, M. Nezadal, H. Gulan, M. Steiner, and C. Waldschmidt, *Characterization of a mm-Wave Automotive Radar with a Low-RCS MIMO Antenna System*, IEEE Conf. Antenna Measurement and Applications (CAMA), Västerås, 2018.

- C. Vasanelli, F. Bögelsack, and C. Waldschmidt, *A Complex Low-RCS Antenna System for the Placement of mm-Wave Automotive Radars Behind Car Bumpers*, European Conf. Antennas Propag. (EuCAP), London, 2018.
- C. Vasanelli, R. Batra, and C. Waldschmidt, *Optimization of a MIMO Radar Antenna System for Automotive Applications*, European Conf. Antennas Propag. (EuCAP), Paris, 2017, pp. 1113–1117.
- C. Vasanelli, F. Boegelsack, and C. Waldschmidt, *Design and Experimental Characterization of a Surface with Low Radar Cross-Section at Millimeter-Wave Frequencies*, European Microwave Conf. (EuMC), London, 2016, pp. 21–24.
- C. Vasanelli, H. Meti, and C. Waldschmidt, *Investigation on a 77-GHz Broadside Vivaldi Antenna*, European Conf. Antennas Propag. (EuCAP), Davos, 2016, pp. 1–5.
- C. Vasanelli, T. Ruess, and C. Waldschmidt, *A 77-GHz Cavity Antenna Array in PCB Technology*, IEEE Mediterranean Microwave Symposium (MMS), Lecce, 2015, pp. 1–4.
- M. Jalilvand, C. Vasanelli, C. Wu, J. Kowalewski, and T. Zwick. *On the Evaluation of a Proposed Bowtie Antenna for Microwave Tomography*, European Conf. Antennas Propag. (EuCAP), The Hague, The Netherlands, 2014.
- M. Jalilvand, C. Vasanelli, J. Kowalewski, and T. Zwick. *Implementation of Antenna Array Systems for Medical Imaging*, German Microwave Conf. (GeMiC), Aachen, Germany, 2014.
- G. Monti, L. Catarinucci, C. Vasanelli, and L. Tarricone, *3D Patch Antenna using a Cardboard Substrate for RFID Reader Application*, European Microwave Conf. (EuMC), Amsterdam, The Netherlands, 2012.

Awards

- Young Engineer Prize for the paper *Design and Experimental Characterization of a Surface with Low Radar Cross-Section at Millimeter-Wave Frequencies* (European Microwave Conference, October 2016)

Herausgeber:
Prof. Dr.-Ing. Christian Waldschmidt

ulm university universität
uulm

ISBN: 978-3-948303-08-2 ISBN: 978-3-9800116-5-5 (E-Book)